Growth and Stability of Silicon Carbide Polytypes

Submitted for the degree of *Doctor of Philosophy* at the University of Cambridge
by Michael John Rutter of Queens' College.

September 1996

Acknowledgements

Memories of my time spent at TCM and the guidance of my supervisor, Prof. Heine, I count among the many indelible benefits of completing a Ph.D. in the TCM group at the Cavendish. It would not be possible to list all who have contributed to the success and pleasure of this period of research, but apart from Prof. Heine, mention must be made of the help and patience of Drs Mike Payne and Guy Makov. Thanks is also deserved by Giles Verwey and Rajiv Shah with whom I have shared an office for a considerable time, and both of whom were kind enough to proof-read this thesis. The errors that remain are probably those which I failed to correct after they were pointed out.

Man does not live by science alone, so grateful thanks is recorded to SERC / EPSRC for funding the first three years of this research, and to my parents for having faith in me after that of EPSRC had failed.

This dissertation is the result of my own work, and does not include the results of any work done in collaboration, except where the work of others is explicitly acknowledged. No part of this dissertation has been submitted for any other qualification at this or any other University.

M. J. Rutter　　　　Cambridge, September 1996

Contents

I Introduction **1**

II SiC & Polytypes: the Background **4**

II.1 SiC: its structure, properties, polytypes & uses 4

II.1.1 SiC: its structure & properties 4

II.1.2 Polytypes 5

II.1.3 Uses of SiC polytypes 7

II.2 Mechanisms for the formation of polytypes 8

II.3 Previous experimental work on SiC 10

II.3.1 Methods of preparation of SiC 10

II.3.2 Growth mechanisms 11

II.3.3 Results of growth of SiC 12

II.3.4 Transformations 14

II.4 Previous computational work on SiC 15

II.4.1 Previous LDA work – the zero temperature results 15

II.4.2 Phonon calculations – the temperature dependent effects 16

II.4.3 The theoretical phase diagram 16

II.5 Theoretical models for polytypes 17

II.5.1 Spin model for layers 17

II.5.2 Spin model for boundaries 18

II.5.3 Devil's staircases 20

II.6 Summary 22

III Polytypes from Phonons: Classical Models **24**

III.1 Motivation & methodology 24

III.1.1 Motivation for studying phonons 24

III.1.2 Outline of methodology 25

III.1.3 ΔF from phonons 26

III.2 1D chain 27

III.2.1 Description 27

III.2.2 Interaction 28

III.3 2D model 29

III.3.1 Description 29

III.3.2 Boundary self energy and nearest neighbour interaction 30

III.3.3 Next nearest neighbour interaction 32

III.3.4 Further interactions 34

III.3.5 Existence of phases in this model 35

III.3.6 Interpretation of results 37

III.4 3D model 39

III.4.1 Description 39

III.4.2 Interactions 39

III.4.3 Existence of phases in this model 40

III.4.4 Interpretation of results 40

III.5 Further analysis 41

III.5.1 How is ΔF spread over ω? 41

III.5.2 The relation to the layer spin model 42

III.5.3 Is <n n+1> stable in general? 44

III.5.4 What deficiencies does this model have? 45

III.5.5 Conclusion 46

IV Polytype Energies from *ab Initio* Electronic Structure Calculations **47**

IV.1 The aim of the calculations on SiC 47

IV.1.1 Why do *ab initio* calculations? 47

IV.1.2 Repetition of bulk calculations 48
IV.1.3 Surface calculations 48
IV.2 The theory of *ab initio* calculations 49
IV.2.1 The Schrödinger equation 49
IV.2.2 DFT & LDA 49
IV.2.3 Supercells & choice of basis set 51
IV.2.4 Plane waves and k-points 52
IV.2.5 k-space sampling and symmetry 53
IV.2.6 Pseudopotentials 54
IV.2.7 FFT grids 56
IV.2.8 CASTEP 58
IV.2.9 Serial or parallel? 60
IV.3 Technical improvement to the symmetry code 61
IV.3.1 Improvements to symmetry code 61
IV.4 Error cancellation & choice of parameters 62
IV.4.1 Error cancellation 62
IV.4.2 Choice of pseudopotentials 63
IV.4.3 Choice of k-points 63
IV.5 Results 64
IV.5.1 Bulk calculations on Si & C 64
IV.5.2 Bulk calculations on SiC 66
IV.5.3 Polytype energy differences: choice of parameters 68
IV.5.4 Polytype energy differences: convergence and results 69
IV.6 Analysis 72
IV.6.1 J_n's 72
IV.6.2 Relaxation 73

V *Ab Initio* Calculations on Surface Orientation **75**
V.1 Polytypic growth from surface energies 75
V.2 CASTEP and surfaces 78

V.2.1 The sandwich cell 78
V.2.2 Termination or reconstruction? 79
V.3 Technical development of calculation with dipole moment 81
V.3.1 Dipole–dipole interaction 81
V.3.2 Corrections for the dipole–dipole interaction 82
V.3.3 Results of tests 87
V.4 Theory, practice & improvements for atomic relaxation 89
V.4.1 Ionic forces through the Hellmann–Feynman theorem 89
V.4.2 $\sum \mathbf{F}_n \neq 0$, and ΔE on rigid shifts 90
V.4.3 Relaxation methods 92
V.5 Results & analysis 95
V.5.1 Results 95
V.5.2 Convergence 97
V.5.3 Accuracy 98
V.5.4 Analysis 100

VI Conclusions and Further Work 101

VI.1 Phonon Stabilisation of Polytypes 101
VI.2 Different growth on different sides of slab 102
VI.3 Need to allow a reconstruction? 102
VI.4 Role of impurities 102
VI.5 Study of surfaces 103

Appendices 104

A Dispersion curve for 2D phonon model 104
B Improved *post hoc* dipole correction 106
C Thermal electronic effects 111
D Polytype energies from J_n's 112

Bibliography 114

Chapter I

Introduction

Silicon carbide is a good example of a polytypic substance. That is, its structure can be considered to be made up of a number of layers stacked together, and each layer has a choice between two different orientations. Thus there is an infinite number of structures, or stacking sequences, in which silicon carbide can form, and each of these is called a polytype.

Naturally these different structures have different free energies, and different temperature dependences of their free energies. The first part of this thesis considers the transition which occurs in SiC between a low temperature and high temperature phase, and the second part concentrates on explaining silicon carbide's anomalous preference for growing in a phase which is merely metastable.

Experimental evidence points towards a phase transition in silicon carbide at a temperature of around 2200K, but the details of the transformation are unclear. Specifically, samples prepared near the transition temperature often show many other polytypes present. These could be dismissed as being caused by varying concentrations of impurities, by dislocation-controlled growth, or some other mechanism. Alternatively, it is possible that they are each truly thermodynamically stable, each over some short range of temperature.

There exists a mathematical model known as a "devil's staircase" in which a phase transition occurs via an infinite number of stable intermediate phases. This model is normally presented in terms of entities confined to a discrete lattice and interacting via a repulsive potential, a sequence of phases occurring as the density of the entities is increased by controlling some external chemical potential. The first part of this thesis continues this idea, considering the position of stacking reversals, or "boundaries" to be the entities, which are interacting via the phonon free energy of the polytypes. The phonon free energy of silicon carbide polytypes has been studied before and is considered to be important in this high–temperature phase

transition. Here a simplified model is studied in more detail with consideration of long–period polytypes and the possibility of a devil's staircase occurring.

In considering the preference of silicon carbide to grow in the metastable cubic form under a range of conditions, firstly a selection of calculations on the bulk energies of various silicon carbide polytypes are presented. These calculations are LDA calculations of the electronic ground state energy of the different polytypes, and thus give the relative stability of the polytypes at 0K. Calculations such as these have been done before, but constant improvements in technique and computing power make their repetition worthwhile so that errors in older calculations can be re-assessed.

Including the dynamic concept of growth in these calculations is more difficult, and produces some new results. Growth is a complicated process which is far beyond the scope of such LDA calculations, but with various simplifications useful data are obtainable. Here growth is considered to be a layer by layer process, with each layer, when added, finding its minimum energy configuration, and then becoming buried in the growing crystal in that configuration. This is a reasonable assumption, as a free surface will find it much easier to rearrange itself towards a minimum in energy than a buried layer would.

The energy differences between bulk polytypes and between different surface structures are very small. Therefore some care is taken to eliminate various error terms, and produce the most accurate assessment of these energies which is reasonably possible.

Chapter II of this thesis presents a review of previous work on polytypism in silicon carbide, covering both experimental results and theoretical studies. This sets the scene for the work on both phonon energies and electronic energies which follows.

Chapter III then describes a model system supporting phonons and containing stacking faults in a similar manner to silicon carbide, and analyses this system to find its phase diagram. By choosing simple models, greater analysis of the existence of long–period polytypes is possible than previous, more accurate models permitted.

Chapter IV then begins the section on LDA electronic calculations, and contains both a review of the LDA method, and new, detailed calculations on the energies of bulk polytypes of silicon carbide.

Chapter V then continues the LDA work with a discussion of its application to surfaces. Corrections for the dipole–dipole interactions between a surface and its periodic image are discussed before the results of the calculations of the energetics of stacking reversals at a free surface are presented.

Chapter VI then draws the above work to its conclusion, summarising the important results.

Thus using a combination of high accuracy LDA calculations on the electronic ground states of various configurations, and an exploration of a simplified phonon model, this work seeks to promote our understanding of polytype growth and stability in silicon carbide. These two approaches, one temperature independent, one highly temperature dependent, complement each other in the consideration of a temperature induced phase transition.

Chapter II

SiC & Polytypes: the Background

II.1 SiC: its structure, properties, polytypes & uses

II.1.1 SiC: its structure & properties

Silicon carbide is a covalent, diamond–structure semiconductor, which rarely occurs naturally, and was first discovered by Berzelius in 1824 [1] during an attempt to make diamond. Each Si and C atom has four neighbours, all of the opposite species, arranged tetrahedrally, with each atom being sp^3 hybridised. The similarity to diamond carries over to the properties of SiC, which is very hard, 9.15 on the Mohs' scale [2], and therefore often used as an abrasive in the form of carborundum. SiC does not melt, but sublimes at around 3000K, decomposing to form a vapour phase containing SiC_2, Si_2C and Si [3].

There are almost no natural sources of silicon carbide, although it has been found in meteorites [4] and diamond pipes [5]. The lack of naturally occurring SiC leaves artificial routes as the only viable methods for the preparation of SiC crystals. Growth from molten SiC is impossible, due to the lack of any liquid phase at standard pressure, or indeed any attainable pressure. Growth from molten silicon supersaturated with dissolved carbon does occur, but the resulting crystals often contain excess silicon and other impurities which have dissolved into the silicon. Thus most preparations are from solid or gaseous phases.

Low quality small crystals can be obtained by the direct reaction of carbon with silica in a furnace. This is quite adequate for some applications, but the electronics industry requires large, high purity, low defect crystals, and these are obtained by one of two methods. Firstly, gas phase reaction between silane (SiH_4) and a hydrocarbon such as propane, and secondly the sublimation of a sample of SiC followed by its recondensation. Both these methods are

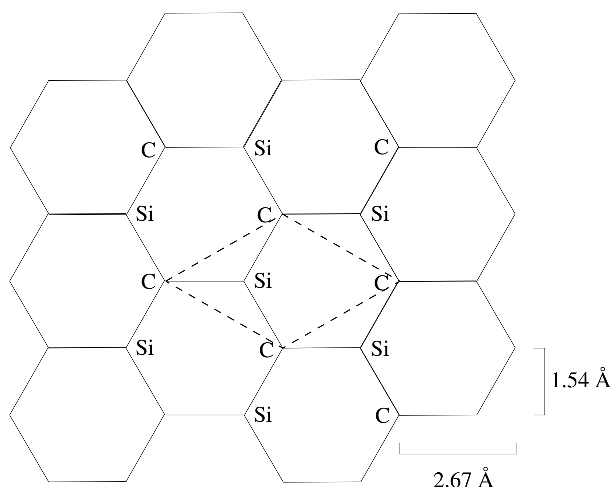

Figure II.1: The structure of a SiC layer. All the C atoms, and all the Si atoms, are coplanar, but either above or below the central plane of the layer, with the hexagons being buckled. The unit cell is outlined and its dimensions given.

discussed further in section II.3.1.

II.1.2 Polytypes

By the end of the nineteenth century this existence of polytypes in silicon carbide had been noted [6]. Today review articles often list fifty or more observed polytypes [7], and there are reports of more than one hundred [8].

What are polytypes? Polytypes are simply different stacking sequences of identical layers. The structure of SiC can be thought of as layers stacked along the [0001] direction of a hexagonal lattice. Each layer can take one of two orientations, independently of its neighbours, and still retain the tetrahedral co-ordination of each atom. Thus n layers can be stacked in 2^{n-1} different ways, forming 2^{n-1} different polytypes. As each layer has just two orientations, a layer can be described by a $+$ or $-$ sign, and then sequences such as $+ + - - + + - -$ written out. This phenomenon is not restricted to silicon carbide, but zinc sulphide, lead iodide, cadmium iodide and many other materials also display some polytypism [9, 10].

In silicon carbide the layers have the structure shown in figure II.1, where the buckling of each hexagon into and out of the plane enables the retention of the perfect $109^\circ\,28'$ tetrahedral angle. Figure II.2 then shows a stacking sequence of these layers, with the bonds shown now lying wholly in the plane of the paper. The orientation of each layer is also shown.

There is an obvious need for a compact notation to aid the discussion of such structures, and two are discussed here. The first, due to Ramsdell [11], describes the number of layers

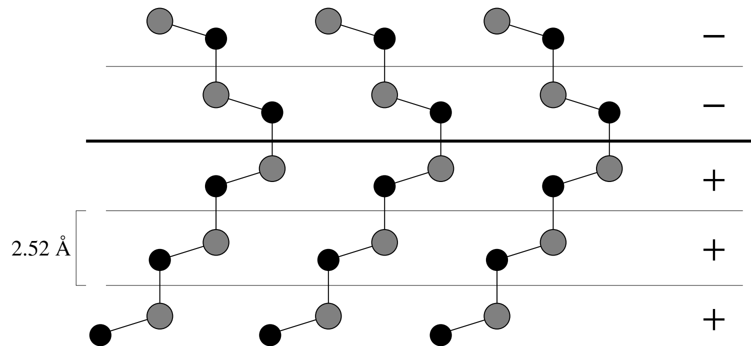

Figure II.2: Layers of SiC stacking to form the repeat unit of the polytype <23>. The stacking boundary is marked with a heavier line.

Repeat unit	Ramsdell symbol	Zhdanov symbol	Other names
... + + + ...	3C	< ∞ >	cubic, zinc blende, β
+ + + − − −	6H	<3>	α type II
+ + − −	4H	<2>	α type III
+ + − − −	15R	<23>	α type I
+ −	2H	<1>	wurtzite

Table II.1: The names of common SiC polytypes.

before a stacking sequence repeats, and then the symmetry of the crystal — cubic, hexagonal or rhombohedral. In this notation, the above structure (+ + − − + + − −) would be called ‘4H’. The repeat period of four is obvious, the hexagonal symmetry arises from consideration of the SiC lattice in particular. This notation has advantages when used to analyse X-ray diffraction patterns, where symmetry and repeat periods are readily obtained, but it has a level of ambiguity as the precise structure within the repeat period is not described. A more precise notation is that of Zhdanov [12], which describes the number of layers before the orientation is reversed. In the above example, with two layers stacked one way, then two the other, the symbol ‘<22>’ or simply ‘<2>’ would be used.

Other systems of naming have been used, based on similar structures in other minerals, the chronology of the discovery of the structures, or other descriptions in terms of layers. Table II.1 names the most common polytypes. The difference in the apparent repeat distances between the Zhdanov and Ramsdell symbols arises because the Ramsdell symbol describes the repeat distance along the c axis, whereas the Zhdanov symbol describes it in terms of layers. Adjacent layers are not vertically above each other, but displaced by one third times $\pm[1\bar{1}0]$. Thus in the case of <23>, or 15R, after one <23> unit, that is five layers, there is a shift in the $[1\bar{1}0]$ direction which is not reduced to a multiple of a unit cell vector for another two units. This is shown also in figure II.2.

Polytype	Lattice constant a (Å)	Band gap (eV)
Cubic	3.083	2.3
2H	3.076	3.3
4H	3.073	3.2
6H	3.081	3.0

Table II.2: Hexagonal lattice constants and band gaps of selected SiC polytypes.

Although many polytypes have been found experimentally, in most cases it is unclear whether they represent thermodynamically stable phases at their formation conditions, or whether they are simply growth phenomena. Long annealing times make the determination of the stable phase difficult, and impurities may also important in stabilising certain polytypes.

Because the nearest–neighbour environment of each atom is independent of the polytype, the physical properties of the polytypes would be expected to be very similar. This is indeed the case for densities and bulk moduli. However, electronic properties are very sensitive to crystal symmetry, and do vary markedly between different polytypes. Table II.2 shows some lattice constants and band gaps, with data taken from Landolt and Börnstein [2] and the NASA Lewis Research Center [13].

As has already been mentioned, polytypism is not restricted to silicon carbide but other materials also exhibit it, notably zinc sulphide, cadmium iodide and lead iodide. In some of these cases the mechanisms for polytype formation are reasonably well understood, but this is not the case for SiC. Mechanisms for polytype formation are discussed in section II.2.

II.1.3 Uses of SiC polytypes

The historic use of silicon carbide is as an abrasive, in which form it is often known as carborundum. This is almost as durable as diamond, but considerably cheaper to prepare. Although SiC is still used as an abrasive, it also finds modern application as a semiconductor, where it offers many advantages over silicon or even gallium arsenide.

One major problem in the electronics industry is that of keeping semiconductors cool during operation. Fans and heatsinks are ubiquitous, as well as being large and heavy. High temperatures destroy semiconductors in two ways. Firstly, they encourage the thermally-activated diffusion of the dopants placed in the semiconductor, so the regions which were discretely doped n– and p–type become less distinct. This process is irreversible. Secondly, the proportion of themally excited conduction electrons increases, which can change circuit function, although it will be reversed on cooling.

Because the SiC lattice is much tighter than the silicon lattice — the bond length is 1.89Å as compared to 2.35Å for Si — diffusion of dopants is inhibited, and the high band gap reduces thermal excitation. Whereas silicon devices are usually limited to junction temperatures of below 170°C at the most, silicon carbide devices have been operated successfully at 450°C [14]. This tolerance of high temperatures is coupled with a thermal conductivity which is over three times higher than that of silicon, so cooling and operation in hostile environments becomes much simpler. This has obvious advantages in satellite and aviation applications.

Another advantage of SiC's high band gap is apparent in optical devices. The optical spectrum, ranging from about 1.9 eV to 3.0 eV, falls within the band gap of SiC, and thus light emitting diodes or even lasers of a full range of colours can be produced with it.

Finally, the break-down electric field of SiC is five times higher than that of silicon or GaAs, giving SiC an advantage in high voltage applications.

In order to utilise the above advantages of SiC, it is important that high quality crystals *of the correct polytype* of SiC can be grown. Silicon production is well developed, with just one phase being grown and zone refining producing very high purity samples, so that twelve inch wafers can be prepared commercially. With SiC, the absence of a liquid phase prevents zone refining, and the presence of competing polytypes adds to the difficulty of preparing a good sample of a single polytype. Thus this thesis investigates some of the possible reasons for polytypic growth, in the hope that through understanding it might be controlled.

II.2 Mechanisms for the formation of polytypes

Polytypism is not restricted to silicon carbide, and it is not necessarily the result of a universal mechanism. Some proposed mechanisms are discussed briefly.

Dislocations

It could be that most polytypes are unstable, being merely growth phenomena. Growth occurs rapidly at steps on a crystal face, and a screw dislocation is an example of a self-perpetuating step. Not only does a screw dislocation give rise to rapid growth, but the crystal grown is also forced to have the periodicity of the Burgers vector of the dislocation. Giant screw dislocations, formed by the merging of many smaller dislocations, can thus force the creation of long period polytypes. This theory was first expounded by Burton, Cabrer and Frank [15] in the context of explaining why growth occurred at all on flat terraces. Two years later Frank [16] pointed out the implications of this mechanism for forcing a particular periodicity

onto polytypes, picking SiC as his example.

This mechanism is widely accepted for zinc sulphide where polytypic crystals often grow as thin needles with hollow cores containing the giant screw dislocations. A full review of this is given in reference [17], together with a clear microphotograph of a dislocation running down the centre of a needle crystal from work by Mardix *et al.* [18]. Pandey and Krishna [19] have also applied this theory to SiC with some success, although the case for this being the sole mechanism causing polytypic growth in SiC is less convincing.

Phonon stabilisation

Jagodzinski [20] suggested in 1954 that the phonon free energy could play an important role in the stabilisation of polytypes. It has since been identified as the driving force in the reversible phase transition from 2H to 12R in PbI_2 [21,22]. Such a theory could also explain the possible 4H to 6H transition in SiC, as will be detailed further in section II.4.2. It is unclear whether such a theory could give rise to a large number of polytypes, and this will be explored in more detail in chapter III.

"Frozen in" surface effects

Heine *et al.* [23] have proposed a model for polytypic growth driven not by bulk stabilisation effects, but rather surface stabilisation effects. It is argued that a new surface layer will take up its lowest energy configuration whilst on the surface, and then become locked into that configuration when buried by subsequent layers, unless the temperature is sufficiently high to allow layers within the bulk to re-arrange – a process which will generally require a much higher activation energy than that required to adjust a surface layer. Thus the results of surface energetics become "frozen in" to the bulk crystal. This idea forms the basis of chapter V where it is discussed in more detail.

Other mechanisms

Many other mechanisms have been mentioned. These include interactions between regions of different polytypes arising from the slight strains caused by the marginally different lattice constants of the different phases, electrostatic interactions between stacking boundaries, impurity stabilisation, and stabilisation by boundary roughening.

This last mechanism deserves a mention in order to rule it out of further consideration in the case of SiC. In some materials, particularly metal alloys such as Cu_3Al, it is possible for the

boundaries between areas of different stacking orientation to be rough, and thus to lower their free energy via entropic effects [24]. This is geometrically forbidden for SiC — any attempt to move from a perfectly flat stacking boundary to one which moved between two layers would involve several eV of strain energy due to the hole that would occur in the lattice.

II.3 Previous experimental work on SiC

The experimental work of interest to a study of polytype growth and stability is that concerning the growth of SiC and transformations between its polytypes. Although growth is not an equilibrium process, so it does not necessarily yield definitive data on polytype stability, it is easy to achieve, and thus there is much data resulting from growth experiments. There follow descriptions of the methods and results of growing SiC crystals, and some experiments concerning their transformation.

II.3.1 Methods of preparation of SiC

The original method of preparing SiC was the Acheson process of 1892 (patent no. 17,911). In this process impure SiC is formed by the direct reaction of silica (SiO_2) with carbon (as coke). This reaction is carried out at high temperatures — up to 2600°C — and produces SiC of fairly low purity, with Al, Fe and N being the main contaminants, present at concentrations varying from 0.1% to 2% in total. Such SiC, often black in colour, is perfectly adequate for grinding, but of no direct use in the electronics industry.

The impure SiC grown by the Acheson process may be refined by subliming and recrystallisation in the Lely process [25] of 1955. A hollow cylinder of SiC is prepared and heated to 2500°C for several hours, with an uneven temperature maintained along the cylinder. New crystals form on the cooler parts of the cylinder, with impurity concentrations as low as 10 ppm. The purest crystals thus formed are pale green or colourless.

Epitaxial growth can be controlled much more precisely and can produce the large, pure crystals required by the electronics industry. This can proceed via CVD (Chemical Vapour Decomposition) from gases such as silane and propane, with hydrogen or argon as a carrier, or from the sublimation of one SiC sample and its deposition onto another sample held at a lower temperature. Growth onto foreign substrates, such as silicon or aluminium nitride, will not be considered here, as it introduces the problem of lattice mismatches which are beyond the scope of this thesis.

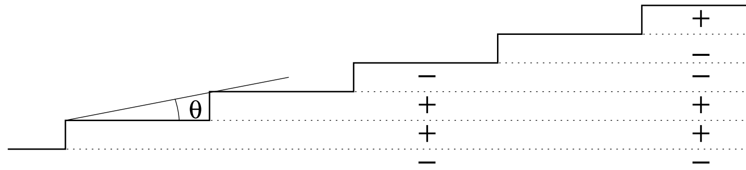

Figure II.3: A terraced near–(0001) surface with a 4H substrate. If growth proceeds by growth at the step edges, 4H is bound to result.

II.3.2 Growth mechanisms

In order to interpret the experimental growth results, it is necessary to understand the basic mechanisms by which a crystal may grow.

The naïve picture is that of atoms arriving on a perfect crystal face and sticking, further adatoms slowly building up successive monolayers. In practice growth never occurs quite like this. A single adatom on a crystal surface is more weakly bonded than an atom in a full monolayer, and even considerably below the sublimation temperature of the crystal such an atom will diffuse around the surface and evaporate.

Growth on perfectly flat terraces will occur, but only if the surface adatoms can diffuse around, collide with each other, and form "islands", before they evaporate. A small "island" of adatoms grouped together will be able to hold together and resist evaporation. For the density of adatoms diffusing around on the surface to be sufficient for islands to form, a considerable overpressure of vapour is usually necessary.

Growth occurs much more readily where there is already a step on the surface. A screw dislocation is a classic source of such a step. Atoms can attach to the edge of the step, bonding to both the step edge and the surface, and as more atoms add to the step, it simply winds around the dislocation core. This not only acts as a permanent site for easy growth, but also forces the growing crystal to have a periodicity equal to the Burgers vector of the dislocation.

Finally, and of particular importance to epitaxial growth, growth can occur at steps not caused by dislocations. If a crystal is cut a few degrees away from a perfect crystallographic face such as (0001) the surface will be stepped as shown in figure II.3. If the growth is slow, it is likely to occur at the step edges, which will grow across the crystal face. If supersaturation is high and the "off angle", θ, small, islands may nucleate on the terraces and this may become the dominant growth mechanism. Whereas step growth must result in further growth of the substrate polytype, terrace growth need not. The cross-over point between these regimes is dependent on θ, the degree of supersaturation, and the diffusion length of adatoms on the surface. The surface diffusion length, which, if high, will enable an adatom arriving in the

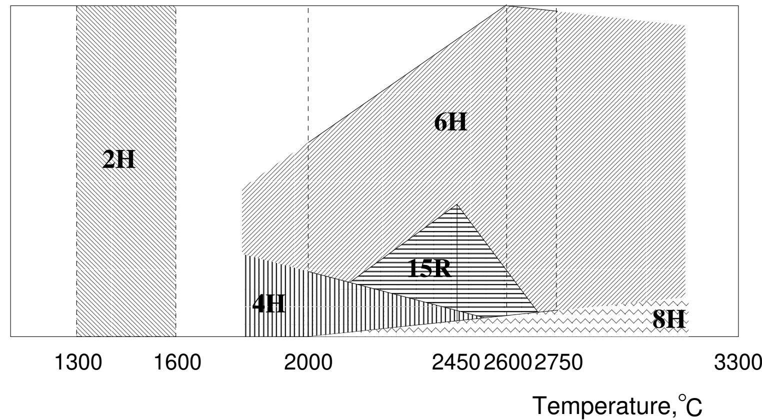

Figure II.4: Relative proportions of polytypes formed as a function of temperature, from Knippenberg [27].

middle of a terrace to find another adatom before it evaporates again, may be different for different crystal faces. In particular, it differs by more than a factor of ten between the (0001) and ($000\bar{1}$) faces of silicon carbide [26], being higher on the carbon face.

II.3.3 Results of growth of SiC

One of the first and still frequently quoted attempts at drawing a stability diagram for silicon carbide polytypes is that of Knippenberg [27] (1963). This is reproduced in figure II.4. This diagram was produced by examining the relative amounts of the different polytypes grown at different temperatures in the Acheson and Lely processes. The original diagram also recorded the cubic phase as being unstable but occurring in the temperature range 1000°C to 2750°C.

Growth by the Acheson or Lely processes still produces the results suggested by figure II.4, in that at high temperatures of above 2600°C 6H is in overwhelming predominance, and if the temperature is reduced to around 1800–2400°C then other polytypes, such as 4H, 15R and 3C are found in the crystals produced.

Epitaxial growth produces somewhat different results. As expected, off-axis orientation tends to result in further growth of the substrate polytype. By this method Itoh *et al.* [28] have grown 4H at 1500°C, whereas Matsunami [29] and Kordina *et al.* [30] have achieved 6H growth at temperatures of 1500°C and 1220°C respectively. Using on-axis growth, Yang *et al.* [31] found that on a 6H substrate 3C grew below 2000°C, and 6H above. Nishino *et al.* [32] have grown 3C on both 15R and 6H at 1500°C. Finally Kanaya *et al.* [33] have produced yields of 80% 4H or 85% 6H, both on the carbon face of a 6H substrate, by varying the growth rate and the temperature between 2280 and 2400°C, 6H dominating at the higher temperature.

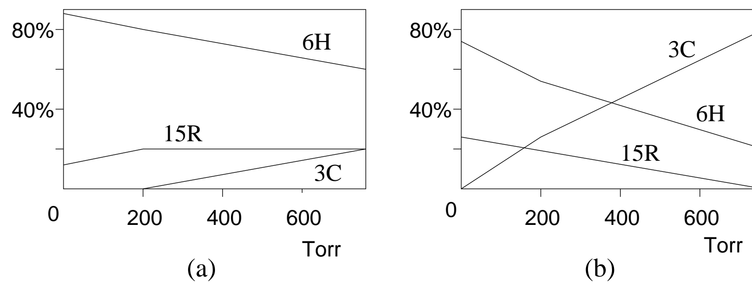

Figure II.5: Relative proportions of polytypes formed as a function of nitrogen partial pressure, from Lilov *et al.* [37]. (a) results for the (0001) silicon face, (b) the $(000\bar{1})$ carbon face.

Thus at one temperature, 1500°C, three different polytypes of SiC have been grown, the substrate and its orientation determining the polytype grown.

Of the other polytypes, 15R is quite common in Lely type experiments, and Buchan *et al.* [34] have observed growth on the carbon face of a 6H crystal change from 6H to 15R at a constant 2100°C. 2H is much less common, usually grown only when impurities such as boron are present and the growth is at low (c. 1500°C) temperatures.

Stein and Lanig [35] concentrated on the distinction between the (0001) and $(000\bar{1})$ crystal faces. Performing almost 400 experiments on epitaxial growth on 4H, 15R and 6H substrates at temperatures between 2200 and 2400°C they found that the carbon face always grew 4H and the silicon surface always grew 6H, independent of temperature, substrate, or the addition of 100 ppm of aluminium. These results are confirmed by Yoo [36], who reports that 3C grows at low temperatures and high supersaturations, but that as temperature is increased growth on the carbon face follows the sequence 4H, 4H+15R, 6H+15R, 6H, whereas that on the silicon face follows the sequence 6H+15R, 6H, with no 4H being grown. Clearly only one of 4H and 6H can be the equilibrium phase under any given conditions, and so at least one must be growing as a metastable phase.

Finally Lilov *et al.* [37] investigated the influence of nitrogen on growth on both the (0001) and $(000\bar{1})$ faces of SiC. Their results are reproduced in figure II.5. Two important points arise from these results: 3C grows much more easily on the carbon face than the silicon face, and on the "easy" face about 1% of the cubic phase is obtained for every 10 Torr of nitrogen present. In these experiments, a total pressure of 760 Torr (one atmosphere) was maintained using argon.

II.3.4 Transformations

Growth is, by definition, a kinetic rather than an equilibrium process. Therefore more convincing data concerning phase stability arise from the study of phase transformations. Many transformations are described in the review article of Jepps and Page [38], and the main points are reviewed here.

The transformation most readily observed is that of 2H to other structures. This re-enforces the suggestion of the growth results that 2H is unstable. Krishna *et al.* [39] observed 2H transforming to 3C after 16 hours annealing at 1400–1800°C, the temperature depending on the sample. They concluded that 3C must be stable within this temperature range, arguing that if 6H were more stable than 3C, the transformation would surely progress straight to 6H.

Tagai *et al.* [40] reported a sequence of phase transitions, with 2H transforming to 3C at 1600°C, then 4H at 1900°C and finally 6H at 2000°C. Krishna and Marshall [41] found a slightly different sequence, with 2H transforming to 3C at 1400 to 1600°C, 6H occurring above 2000°C, and disorder in between. Their estimate of 3C's stability range was thus revised to being below 1600°C. A review of experimental observations of transformations of 2H is given by Pandey *et al.* [42].

The cubic phase has also been observed transforming to 6H, but it requires higher temperatures. Jepps and Page [43] studying 3C / nH interfaces, observed a 3C to 6H transition at 1800°C, and a 3C to 4H transition at 1880°C. Jepps and Page also did a series of experiments heating cubic SiC in argon for varying lengths of time [38], and even at 2300°C it took one hour for 63% of the sample to transform to 6H, and a further hour took the amount transformed up to 89%. Even at this high temperature, therefore, the transformation is quite slow, and at lower temperatures much longer annealing times can be expected.

A transformation of 15R to 6H has been observed by Inmomata *et al.* [44]. They heated two crystals together, one of 15R and the other of 6H, at 2500°C for 8 hours, after which time the 15R crystal had evaporated completely, and the 6H crystal had enlarged. This result was repeatable. Thus they concluded that 15R had a higher vapour pressure than 6H, and hence was unstable with respect to 6H under these conditions. A total pressure of one atmosphere was maintained with argon, containing less than 5 ppm of nitrogen.

Just as nitrogen can be important in influencing polytype formation in growing SiC, so it can be in transformations. Jepps and Page [45] heated commercially obtained SiC samples with a mean grain size of 10 μm for 30 minutes at various temperatures in both nitrogen and argon atmospheres. The samples were originally less than 5% cubic. On heating at 2250°C in argon at 10 and 30 atmospheres pressure, the result was completely hexagonal — over 90%

6H with a little residual 15R. However 30 atmospheres of nitrogen produced the opposite result, with now 94% of the sample transforming to the cubic phase within 30 minutes. Even one atmosphere of nitrogen was sufficient to transform 25% of the sample in the half hour, and the effect was still noticeable at temperatures as low as 1800°C. It must also be pointed out that these samples contained around 10% free silicon.

II.4 Previous computational work on SiC

II.4.1 Previous LDA work – the zero temperature results

Differences in the electronic energies of systems can be found to a remarkably high degree of accuracy using a technique known as the local density approximation (LDA). The details of this method are discussed in detail in chapter IV. Let it suffice to say here that accuracies of better than 1 meV per atom are obtainable in energy differences calculated using this method, but that its major disadvantage is that it assumes the nuclei are without thermal motion. Thus it produces results valid for very low temperatures only, where phonon effects are unimportant. The technique is also computationally expensive, and thus limited to polytypes of short repeat period, such as 2H, 4H, 6H and 3C.

The first such study of the stability of silicon carbide polytypes was that of Cheng *et al.* in 1988. It concluded that of the "ideal" structures, that is allowing no relaxation from the positions within the unit cell given by the layer stacking model, and no relaxation of the unit cell axes, 4H and 6H were the most stable, by 1 meV per pair over 3C and 10 meV over 2H, as is shown in the first column of table II.3. The work was then continued [46] by consideration of relaxation of the unit cell and atomic positions. The changes on relaxation were found to be small — just 0.7 meV per pair for the most relaxable structure (4H), and thus caused no qualitative change in the results. The errors in the differences were estimated to be less than 1 meV per pair.

Similar calculations have also been done by Käckell *et al.* [47], with somewhat different results as also shown in table II.3. The ordering of the unrelaxed structures is slightly surprising, with 3C lowest, and a 3C / 2H difference of 15 meV, rather greater than that of Cheng *et al.*, but the biggest difference is the huge change in energy on relaxation. Although the relaxation energies cannot be calculated directly from their calculations, it is clear that 2H must have relaxed by over 13 meV, and 4H by 8 meV, even assuming that 3C remained unchanged. The final relaxed results seem unlikely from an experimental point of view, as 3C is very much more common than 2H experimentally, but their energy costs over 4H and 6H are similar in these calculations. Again an accuracy of better than 1 meV per pair is claimed.

Polytype	Cheng *et al.*		Käckell *et al.*	
	ideal	relaxed	ideal	relaxed
2H	8.70	8.69	15.2	1.8
3C	0.00	0.00	0.0	0.0
4H	–0.78	–1.46	4.4	–3.8
6H	–1.19	–1.59	2.6	–3.0

Table II.3: Energy differences between polytypes from electronic structure calculations. Results are expressed in meV/pair, with 3C taken as the zero in each column.

These results are discussed again at the end of chapter IV, but it is clear that they agree on 2H being less stable than the others, and 3C being less stable than 4H and 6H, at least after relaxation. The difference between 4H and 6H is too small to be distinguished at the quoted accuracy of these results.

II.4.2 Phonon calculations – the temperature dependent effects

With the electronic energies of the polytypes, particularly 4H and 6H, being so close, phonon effects could be important in stabilising phases at high temperatures. A theory of a phonon-driven phase transition has been advanced for lead iodide [22], and here also such a theory has been investigated.

Again the work is by Cheng *et al.* [48] who used a valence overlap shell model to calculate the phonon spectra of different polytypes, and hence their phonon free energies. The phase 6H was found to have a softer spectrum than 4H, and thus a lower phonon free energy at high temperature. The difference is very small, just 76 μeV/pair in favour of 6H over 4H at 2000K, or 92 μeV/pair at 2400K. The ordering of phonon free energies at high temperature, from highest to lowest, was found to be 4H, 15R, 6H, 3C.

II.4.3 The theoretical phase diagram

Keeping half an eye on the experimental results, it is possible to construct a theoretical phase diagram for SiC in the following fashion. The total free energy of a polytype is given by

$$F(T) = E_{el} + F_{\phi}(T) \qquad \text{(II.1)}$$

where E_{el} is the electronic contribution, and is assumed to be independent of temperature, and F_{ϕ} is the phonon contribution and varies with temperature.

Assuming 4H to have a slightly lower electronic energy at 0K, a phase transition to 6H can

be produced due to the contribution from the phonon free energy. Assuming this transition to occur at about 2400K, it is necessary to assume that the difference between the electronic energies of 4H and 6H is approximately 0.1 meV/pair. This is not inconsistent with the likely errors in the results of table II.3. Around the transition point it is possible that 15R becomes stable over a brief temperature range. Its phonon free energy makes it more stable than 4H, but less stable than 6H, as temperature is increased, so whether or not it appears as a stable phase around the 4H to 6H transition point depends on its precise electronic free energy. Cheng *et al.* [48] speculated that it *is* stable, over a range of about 500K centred on 2500K, although this range would seem rather large given the dominance of 6H in growth experiments. Other possible intermediate phases were beyond the scope of their work.

The cubic form, although having the lowest phonon free energy, has too high an electronic energy to be stabilised below the sublimation point of SiC. Its stabilisation temperature would be around 15 000K.

II.5 Theoretical models for polytypes

There are many ways of modelling the structures of silicon carbide in terms of simple layer or boundary interactions. Two of these descriptions follow.

II.5.1 Spin model for layers

As each layer has two orientations, it can be described by a variable, σ, taking the values ± 1, as is shown in figure II.6. Once this is done, the energy of a system of N layers could be expanded in terms of layer–layer interactions as

$$E = J_0 N - \sum_{i,n} J_n \sigma_i \sigma_{i+n} - \sum_{i,n,m,o} K_{n,m,o} \sigma_i \sigma_{i+n} \sigma_{i+m} \sigma_{i+o} + \ldots \tag{II.2}$$

In such a summation, J_0 represents the self-energy of a layer, J_n a layer–layer interaction, $K_{n,m,o}$ a four–layer interaction, and higher terms are possible. Such an expression must be unchanged on multiplying all σ's by -1, as this corresponds to a rotation of the crystal. Hence no terms with an odd number of σ's may occur. Such models have been applied to silicon carbide, considering just J_0, J_1, J_2 and J_3 to be non-zero [49, 50], and also with the addition of $K_{1,2,3}$ [51].

The form

$$E = J_0 N - \sum_{i,n} J_n \sigma_i \sigma_{i+n} \tag{II.3}$$

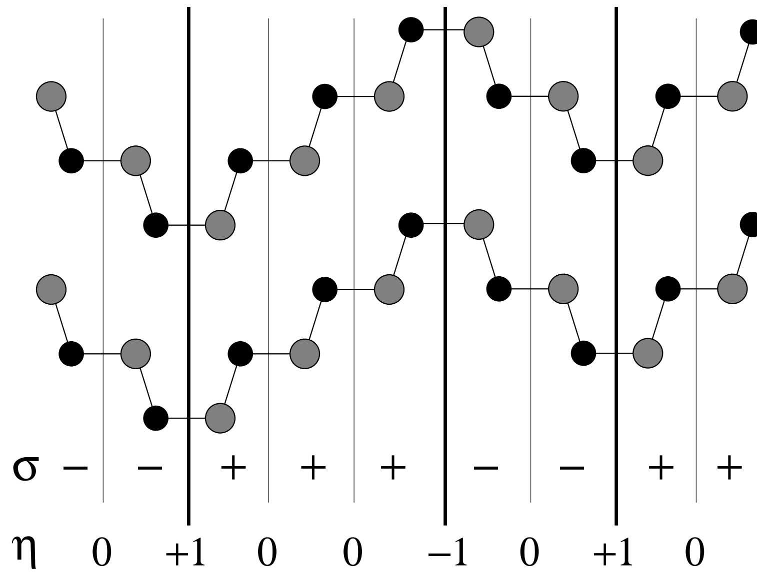

Figure II.6: The description of a polytype in terms of σ and η.

will often be used in this work, without any truncation of the range of J_n.

II.5.2 Spin model for boundaries

Just as above the focus of attention was the layers in the stacking sequence, equally one could focus on the boundaries. There are two types of boundary, that between '+' and '–' layers, and that between '–' and '+' layers. Just like the two types of layer, these boundary types are related by a rotation. This is also shown in figure II.6.

Therefore one can define a variable η at every position a boundary could occur, taking the value of 0 if there is no boundary, or ± 1 depending on the type of boundary. Considering only boundary–boundary interactions, the energy with respect to the boundary–free system can now be written

$$E = I_0 N_b - \sum_{i,n} I_n \eta_i \eta_{i+n}. \tag{II.4}$$

The terms in this equation can be related to those in equation (II.3) by the following consideration. First considering the two systems

$$\ldots + + + + + + + + + + + + + \ldots$$

and

$$\ldots + + + + + + - - - - - - \ldots$$

The energy difference between these can be expressed as

$$\Delta E = I_0 = 2 \sum_{n=1}^{\infty} n J_n. \tag{II.5}$$

In order to calculate the boundary–boundary term, let m be the separation of the two boundaries in the system

$$\ldots + + + - - - - - - - + + + \ldots$$

The energy difference between this system and the first is now

$$\Delta E = 2I_0 + I_m = 4 \sum_{n=1}^{m} n J_n + 4 \sum_{n=m+1}^{\infty} m J_n \tag{II.6}$$

so that

$$I_m = -4 \sum_{n=m+1}^{\infty} (n - m) J_n. \tag{II.7}$$

One important idea is partially hidden in equation (II.4): that is that the interaction between like boundaries is the same in magnitude and opposite in sign to that between unlike boundaries. As the two types of boundary must alternate in any system, this is equivalent to saying that the interaction between boundaries with an odd number of intervening boundaries is equal in magnitude and opposite in sign to that between boundaries with an even number of intervening boundaries. It might appear that this is simply an inevitable consequence of choosing to write the energy in the form of equation (II.4): in fact it follows directly from equation (II.3) as was proven by Cheng *et al.* [48], and thus is rather more fundamental.

To stress this point once more, the interaction between two boundaries could be written as $I^j(n)$, where the boundaries have $j - 1$ intervening boundaries. Then

$$\begin{aligned} I^j(n) &= (-1)^{j+1} I^1(n) \\ &= (-1)^{j+1} I(n) \\ &= (-1)^{j+1} I_n, \end{aligned} \tag{II.8}$$

defining $I(n) = I^1(n) = I_n$ as a convenient short-hand.

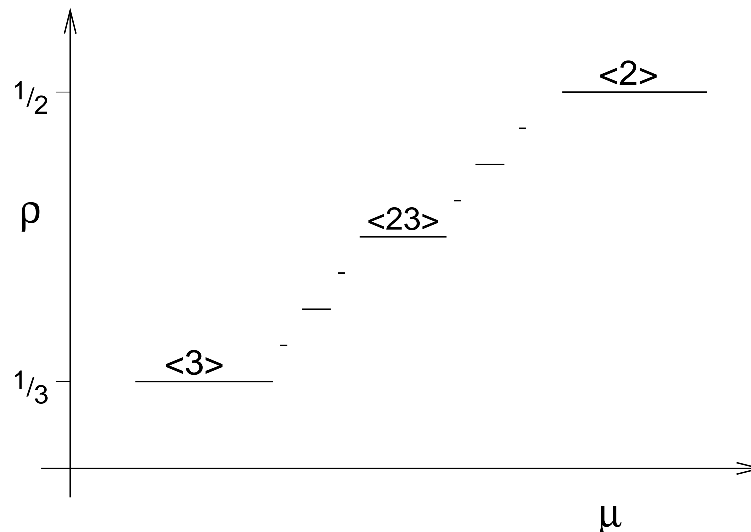

Figure II.7: A phase transition via an infinite staircase of intermediate phases as a function of some parameter μ.

II.5.3 Devil's staircases

A phase transition, such as that from <2> to <3> in SiC, need not be simple and direct. Indeed, it could proceed via an infinite number of intermediate phases to form a devil's staircase [52, 53], each intermediate phase being thermodynamically stable at some point during the transition. This is shown schematically in figure II.7, where the external parameter would represent temperature in the case of the SiC transition.

Such a staircase might seem highly unlikely, but it can arise from very simple and general mathematical models. Bak and Bruinsma [52] showed that if one considered a system of identical entities confined to a one dimensional grid, such a stair would result provided the interaction between the entities was:

- repulsive
- convex
- infinite ranged
- pairwise.

In solid state physics, grids arise naturally from lattices. For the SiC phase transition, the stacking faults can be considered to be the entities, constrained to lie on the one dimensional grid formed by the SiC layers. Other related systems include transformations in the 2D monolayer of a noble gas on a surface, such as argon on platinum [54].

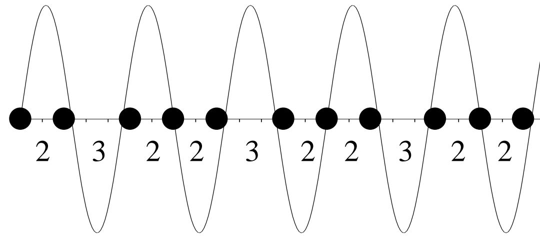

Figure II.8: The formation of a devil's staircase sequence from a sine wave. The function $\sin(\frac{3}{7}\pi x)$ gives the sequence <223>.

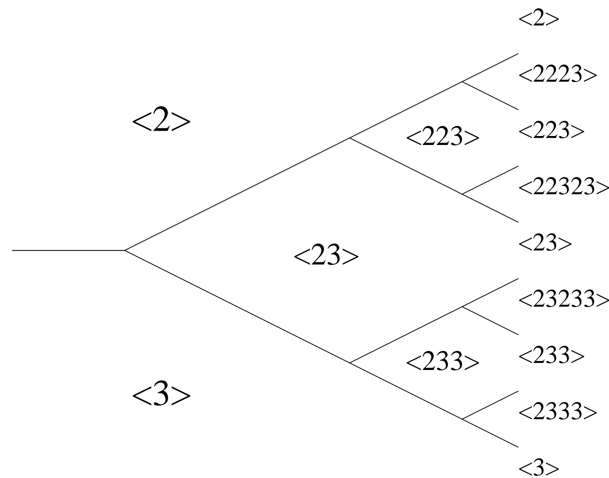

Figure II.9: The formation of a devil's staircase sequence from a bifurcation tree.

The theory of devil's staircases goes further than to predict an infinite sequence of intermediate phases — it predicts particular infinite sequences. The sequence given by the Bak–Bruinsma model above can be constructed in two different ways as follows. Firstly one may consider the zeros of the function $\sin(\pi x/\lambda)$ for $2 \leq \lambda \leq 3$, and then move these zeros to the nearest integer. As λ is varied, the shifted zeros map out all the members of the sequence. This is illustrated in figure II.8, where a λ of $2\frac{1}{3}$ gives the phase <223>.

An identical sequence is produced by the bifurcation tree shown in figure II.9, as was shown by de Fontaine [55]. Starting from the two phases <2> and <3>, these are combined to make the intermediate phase <23>. Then again at each boundary the two phases are combined to make an intermediate, and so on.

It should be stressed that these sequences do not include every possible intermediate phase between <2> and <3>. The phase <2233> is the simplest which is clearly absent.

The bifurcation tree also makes it possible to produce different sequences. For instance, if the phases <22>, <23> and <33> are used as the starting points, all resultant phases will

have an even number of symbols in their Zhdanov notation. Such a staircase, which will be called an "even staircase" has been mentioned as a natural extension of the tree model above by Cheng *et al.* [48]. It has some phases in common with the Bak–Bruinsma stair, such as <2223>, and some phases unique to it, such as <222323>. Similarly, even some of the phases in the Bak–Bruinsma staircase which have an even number of symbols, such as <22322323> are still not in the "even staircase."

The stacking boundaries in SiC cannot map directly onto the Bak–Bruinsma model due to the existence of the two different types of boundary. Although these two types are related by a reflection, like and unlike boundaries need not interact in the same manner, as discussed above in section II.5.1. Hence the Bak–Bruinsma staircase may need slight modification before it applies to SiC, such as the change to an even staircase already discussed.

II.6 Summary

From all the above data, conclusions are now drawn about the stability of the different polytypes and the phases grown.

Considering first polytype stability, the wurtzite phase (2H) is difficult to grow without special conditions, such as the presence of boron, and readily transforms to other polytypes on annealing. Electronic energy calculations all show it to be the least stable at zero temperature, the annealing results suggest it is unstable at high temperature, and therefore it will be assumed to be unstable at all temperatures.

On the other hand the 6H phase is readily grown and formed by annealing, and theoretical calculations suggest it to be one of the most stable polytypes at zero temperature, and to have a phonon free energy which will favour it over the other polytypes between <2> and <3> at high temperatures. Therefore it will be assumed to be the high temperature phase.

The above two conclusions are fairly clear and well accepted. It is with slightly more hesitation that the following propositions are also made: that 4H is the low temperature phase, that the cubic phase is never stable, and that intermediate phases between 4H and 6H, most notably 15R, may be stable around the transition between 4H and 6H. These conclusions can be drawn directly from the computational data, and are not in conflict with the experimental evidence.

The cubic phase is claimed to be unstable because of the results of the electronic structure calculations which place it above the 4H and 6H polytypes at zero Kelvin, and because donor impurities such as nitrogen might account for its experimental occurrence, as also might the growth procedure described below. The band gap in 3C is 0.7 eV less than that in the

other polytypes, whereas the energy differences between the structures are around 1 meV per atom. It might be expected, therefore, that adding a donor such as nitrogen (which substitutes directly for carbon) to the crystal would favour the cubic structure by 0.7 eV per donor. This would suggest that the cubic structure might be stabilised with 0.14% nitrogen. Such an analysis has been made before [23], and is fairly rough, but it does give an idea of the sort of impurity concentrations which could be important.

Donors and acceptors have a similar affect on 4H and 6H. The difference in band gap is smaller at 0.2 eV, but the difference in energy is also much smaller. Jepps and Page [56] report a 6H to 4H transition on the addition of boron, and the reverse transition on adding nitrogen to the sample.

The claim that 4H is the low temperature phase is the most debatable. It would help to explain why the phase is relatively common in growth experiments, particularly those at lower temperatures. That there is little evidence of a 6H to 4H phase transition on annealing at any temperature is readily explained away by the high activation energy and small driving energy of any such process. Small amounts do however occur when cubic SiC is heated to temperatures below 2200°C [38].

The stability of 15R and other polytypes is not something which can be deduced from the experimental evidence available. It is possible that some of them are stable over short ranges of temperature, equally it is possible that they are growth phenomena caused by dislocations.

Thus the most likely phase diagram of SiC is taken to be 4H below about 2000°C, 6H above about 2500°C, and maybe some intermediate phases in the intervening temperature range, with 15R being most likely intermediate phase, or being expected to have the largest range of stability of such phases.

Growth, not being an equilibrium process, need not follow the above conclusions. It is clear that steps and dislocations can readily force the growth of a specific polytype, but that in the absence of these 6H is the high temperature phase, 4H and 15R grow at intermediate temperatures, and 3C is consistently grown below about 2000°C. The proposition is made that growth on a flat terrace *always* occurs as 3C, but that at higher temperatures this anneals to one of the hexagonal polytypes as fast as it is grown. Thus low supersaturations and large off-angles result in step controlled growth and reproduction of the substrate polytype, high supersaturations and low off-angles at low temperatures leave 3C, and at higher temperatures annealing to 4H or 6H occurs as the crystal grows. As 3C nucleates independently on each terrace, and can do so either as '$\ldots +++ \ldots$' or '$\ldots --- \ldots$' on a 4H or 6H substrate, boundaries between these forms would be expected, and are indeed common [57]. This idea of 3C being the initial form of growth on a flat terrace forms the basis of chapter V, where it is discussed further.

Chapter III

Polytypes from Phonons: Classical Models

This chapter considers one mechanism which could cause different polytypes to be equilibrium structures: that of stabilisation by changes in the phonon free energy. Previous work [48, 58–60] on the phonon spectra of silicon carbide polytypes has used sophisticated models of the structure of SiC and of the Si–C interaction such as the valence overlap shell model or the bond charge model. The work has thus been restricted to simple polytypes such as 3C, 4H, 6H and 15R, and only Cheng *et al.* [48] tried to produce a phase diagram from this approach. This work takes a different approach to a slightly different goal. With the aim of determining whether phonon effects could cause a devil's staircase (as described in section II.5.3), a much simplified model is presented, yet one in which the main features of SiC are retained. This simplified model permits calculations on long period polytypes which would be impossible with a full shell model.

For the rest of this chapter the Zhdanov notation is used, it being more convenient when discussing more complicated polytypes. This notation was introduced in section II.1.2.

III.1 Motivation & methodology

III.1.1 Motivation for studying phonons

There are many good reasons to study phonons in relation to phase transitions. Jagodzinski [20, 61] was the first to dwell on the importance of phonon free energy in phase transitions, and the work of Cheng *et al.* [48] has shown it to be of importance in silicon carbide. Phonon

energy changes have also been shown to be important in a phase transition between polytypes of lead iodide [22].

Why should phonons be important in polytype stabilisation? There are two reasons. Firstly phase transitions on temperature changes must be governed by a temperature dependent term in the free energy. For a semiconductor, the electronic energy is not strongly temperature dependent. It is not possible to smear a Fermi surface as the temperature increases, but rather electrons must be promoted across a bandgap of a few eV, whereas kT is just 0.2 eV at 2300K. The level of promotion is therefore extremely small, and the temperature dependence slight. An estimate of the total change in the electronic free energy of 6H as about 1 μeV between 0K and 2500K is given in appendix C.

If the electronic contribution is negligible, perhaps entropic effects are important. In some A_3B metal alloys this is indeed the case [24]. In such systems a boundary can "roughen," reducing its free energy via the entropy term, at almost no cost to the energy of the lattice. In SiC any attempt to roughen a boundary produces major faults in the lattice costing several eV. Therefore boundary roughening simply does not occur in SiC, and does not contribute an entropic term to the free energy. The possible disorder in the stacking sequence is a one dimensional phenomenon and will be swamped in an extended system by any term which scales as the system size.

Phonons do occur, indeed, they are a universal phenomenon, and their contribution to the free energy is temperature dependent. Thus phonons are a candidate for producing phase transitions.

Secondly, and more importantly for polytype stabilisation, phonons are a long wavelength phenomenon. Whereas electronic effects are screened and decay rapidly, being weak even at next nearest neighbour level [62], the long wavelength of phonons suggests that they could produce long range interactions and stabilise long period polytypes. Thus, in the hope of finding a temperature dependent long ranged interaction, this chapter studies phonons.

III.1.2 Outline of methodology

Constraints imposed by electronic effects forbid boundary placements with separations of other than two and three. The observed scarcity and high electronic energy of wurtzite precludes a boundary spacing of one. Spacings larger than three are also rarely observed, although the electronic structure data refer only to the cubic form with its infinite boundary spacing.

The full shell model used by Cheng *et al.* permits calculations on systems with a repeat period

of twenty or so. In order to go significantly beyond this, a two stage approach is employed. Firstly a much simplified model of balls and springs is used which allows calculations with a repeat period of around one hundred to be done cheaply. By performing many calculations with this model, terms such as the boundary self–energy, the nearest neighbour boundary–boundary interaction as a function of separation, and the next nearest neighbour interaction are calculated. From such terms, an informed extrapolation is made to the full form of the boundary–boundary interaction, $I^j(n)$, where n is the separation of two boundaries and j one more than the number of intervening boundaries. Then the free energy contribution to a system from the phonons due to the number and position of the boundaries can be written as

$$F_\phi = I_0 N_b + \sum_{\substack{boundary \\ pairs}} I^j(n). \tag{III.1}$$

This expression can be evaluated for systems of around 10^5 layers in a couple of minutes on an average PC, and thus calculations on truly long period polytypes are possible.

Having thus found the temperature dependent term in the phonon free energy, this can be combined with the electronic temperature independent term in order to produce a temperature dependent free energy for each polytype, and thus a phase diagram can be constructed.

III.1.3 ΔF from phonons

The following work is all done in the high temperature approximation for the phonon free energy, F_ϕ, which, starting from the definition of F_ϕ in terms of the partition function for each phonon mode, is

$$\begin{aligned} F_\phi &= \sum_n -kT \ln Z_n \\ &= -kT \sum_n \ln \sum_{m=0}^{\infty} \exp\left[\frac{-(m+\frac{1}{2})\hbar\omega_n}{kT}\right] \\ &= -kT \sum_n \ln \left(\frac{\exp(-\frac{1}{2}\hbar\omega_n/kT)}{1-\exp(\hbar\omega_n/kT)}\right) \\ &= kT \sum_n \ln\left(2\sinh\left(\frac{\hbar\omega_n}{2kT}\right)\right) \\ &\approx N_\phi kT \ln\left(\frac{\hbar}{kT}\right) + \frac{1}{2}kT\Xi \end{aligned} \tag{III.2}$$

where

$$\Xi = \sum_n \ln\left(\omega_n^2\right) \tag{III.3}$$

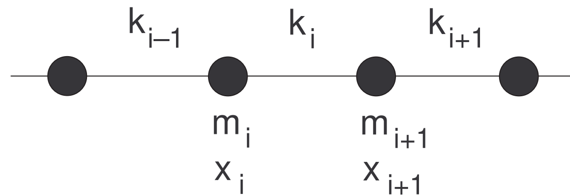

Figure III.1: A chain of masses and springs, with m_i representing the mass, x_i the displacement from the equilibrium position, and k_i the spring constant as shown.

the summations over n are over the non-zero frequency phonon modes, and N_ϕ is the number of such modes.

The only term in this equation which depends on the structure rather than the extent of the system, that is on the polytype, is Ξ. Thus when comparing the free energies of different polytypes, the other terms can be ignored.

Because the important free energy differences are related to differences in the logarithms of the eigenfrequencies, a uniform scaling of all the eigenfrequencies produces no change at all in the free energy differences as it simply shifts the free energy of all polytypes by the same amount. Thus the absolute choice of mass or spring constant is irrelevant in these calculations.

III.2 1D chain

III.2.1 Description

The fundamental requirements for a simplified model of phonon effects in SiC are that it should support phonons and should permit a perturbation to be introduced which will scatter the phonons. The boundaries in SiC interact with the phonons by causing a mixture of partial transmission and reflection, and so must whatever is used to represent the boundaries in a simplified model.

The simplest model would be a one dimensional chain of balls and springs, as shown in figure III.1. A boundary can be represented by a changed mass or spring constant, which will be sufficient to scatter any phonon travelling along the chain. This model is so simple that it can be readily analysed analytically. Using the usual co-ordinates of

$$u_i = \sqrt{m_i} x_i \tag{III.4}$$

the equation of motion of the chain is

$$\omega^2 u_i = A_{ij} u_j \tag{III.5}$$

where

$$A_{ij} = \begin{cases} (k_{i-1} + k_i)/m_i & j = i \\ -k_i/\sqrt{m_i m_j} & j = i \pm 1. \end{cases} \tag{III.6}$$

The important quantity in this analysis is the sum of the logs of the eigenvalues, that is Ξ. This is equivalently the log of the determinant, as

$$\Xi = \sum_i \ln\left(\omega_i^2\right) = \ln \prod_i \left(\omega_i^2\right) = \ln \det \underline{\underline{\mathbf{A}}}. \tag{III.7}$$

Thus for this system Ξ can be written as the determinant of a simple matrix.

III.2.2 Interaction

The interaction produced between changed masses on this chain can be calculated by considering a system where $m_i = m$ for all i, except at two positions p and q where $m_p = m_q = M$, and seeing how Ξ depends on the separation $p - q$. In fact, the analysis can be made even more general.

If a matrix $\underline{\underline{\mathbf{B}}}$ is defined to be equal to $\underline{\underline{\mathbf{A}}}$ but without the factors of m, then as each m_i appears to the power of -0.5 throughout just one row and one column

$$\det \underline{\underline{\mathbf{A}}} = \det \underline{\underline{\mathbf{B}}} \prod_i (m_i)^{-1}. \tag{III.8}$$

As m appears in the product only, this expression is independent of the position of any changed masses, so there is no dependence on $p - q$ for the example given, and no interaction between the changed masses. This is not to say that the changing a mass does not change the phonon free energy, just that the change is independent of the other masses in the chain.

In order to consider changes in the k's, it is necessary to transform $\underline{\underline{\mathbf{B}}}$ somewhat. $\underline{\underline{\mathbf{B}}}$ represents the equations of motion for a system of unit masses, the masses having been factored out of the original matrix $\underline{\underline{\mathbf{A}}}$. These equations are as follows:

$$\begin{aligned} -\omega^2 u_i &= k_{i-1} u_{i-1} - (k_{i-1} + k_i)\, u_i + k_i u_{i+1} \\ -\omega^2 u_{i+1} &= k_i u_i - (k_i + k_{i+1})\, u_{i+1} + k_{i+1} u_{i+2}. \end{aligned} \tag{III.9}$$

These equations are written twice to ease the transformation from u_i to a co-ordinate $e_i =$

$u_{i+1} - u_i$, which is achieved by subtracting the first line from the second, thus:

$$-\omega^2 e_i = k_{i-1}e_{i-1} - 2k_i e_i + k_{i+1}e_{i+1} \tag{III.10}$$

or in matrix form,

$$\omega^2 e_i = C_{ij} e_j \tag{III.11}$$

with

$$C_{ij} = \begin{cases} -k_{i-1} & j = i-1 \\ 2k_i & j = i \\ -k_{i+1} & j = i+1. \end{cases} \tag{III.12}$$

And finally,

$$\det \underline{\underline{\mathbf{C}}} = \det \underline{\underline{\mathbf{D}}} \prod_i (k_i) \tag{III.13}$$

Where $\underline{\underline{\mathbf{D}}}$ is the matrix with 2 on the leading diagonal, and -1 on the first off–diagonal. So once more $\sum \ln \omega^2$ is independent of the position or relative position of any changed k's.

Any concern that all of the above determinants are zero anyway due to the presence of an $\omega = 0$ mode can be allayed by realising that this zero-frequency mode can be removed by attaching one single atom to a fixed spring. This just adds a term k'/m_x to the element A_{xx} where x refers to the atom concerned. The rest of the factorisation is unchanged. A similar argument applies for the case of changed spring constants.

Thus for a general one dimensional chain with Hooke's Law nearest neighbour springs, no interaction can arise between the "boundaries" of changed masses or spring constants, and no phase diagram can result.

III.3 2D model

III.3.1 Description

It is clear that too many simplifications were made in the construction of the one dimensional model above, so now a two dimensional model is investigated. On a two dimensional grid it is possible to place springs in different orientations in different columns, and thus produce a structure more closely analogous to a polytypic structure. As shown in figure III.2, a square mesh is used in which each column has one diagonal link per cell, sufficient to prevent zero frequency modes, and sufficient to define an orientation for each column. The figure shows two changes in orientation, or stacking boundaries. Comparison with figure II.2 shows that the structure is analogous to SiC, with the boundaries being formed between two areas identical

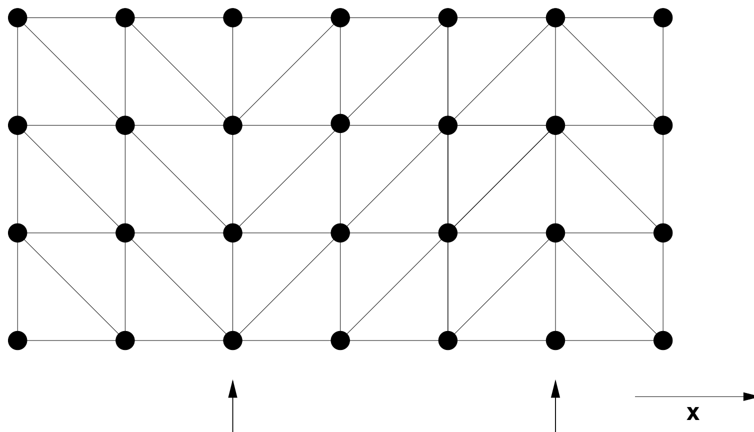

Figure III.2: Simple 2D ball–and–spring model showing stacking reversals. The lines represent springs. Note the two boundaries indicated by the arrows.

apart from a rotation.

This model has one important advantage over the one dimensional chain: it recovers the idea of there being two types of stacking boundary, related by a reflection, as discussed in section II.5.2.

III.3.2 Boundary self energy and nearest neighbour interaction

The calculations performed here are done on a 120×48 grid with periodic boundary conditions. The boundaries are placed perpendicular to the longer direction, whilst Bloch's theorem is used along the boundaries to reduce the computational effort. A simple test of the code and an analytic consideration of the infinite boundary–free grid are given in appendix A. By calculating the energies of various systems with stacking boundaries, it is hoped that a formula such as

$$\Xi = \Xi_0 + N_b A_b I_0 + A_b \sum_{i,j} I^{j-i}(r_i - r_j) \tag{III.14}$$

can be applied, where N_b is the number of boundaries, A_b their area, r_i the position of the ith boundary, and I_0 and $I^j(n)$ the self-energy and interaction energy of boundaries. The A_b is extracted from I_0 and $I(n)$ to leave a quantity which should be almost independent of system size.

Firstly Ξ_0 was calculated. This is simply the energy of the boundary–free system, and has no further bearing on the results, so it is subtracted from the other Ξ's quoted. Its value is just under 8700.

On a periodic system, the number of boundaries must be even, as shown by figure III.3, so

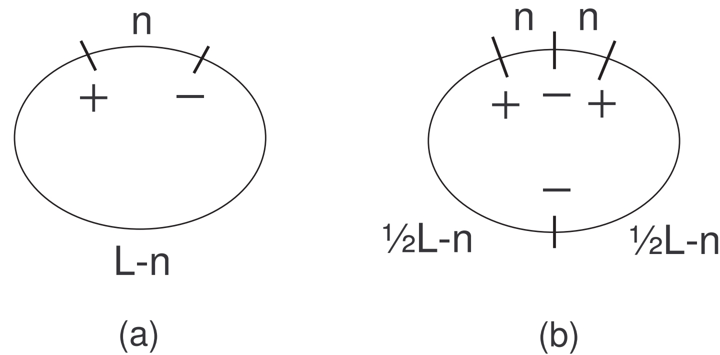

Figure III.3: Systems with (a) a pair and (b) a triplet of boundaries used in determining nearest–neighbour and next nearest–neighbour interactions. A fourth boundary is required with the triplet, as the boundaries must alternate in type. Here L is the length of the system in the x direction, the closed loop indicating the use of periodic boundary conditions.

the simplest systems that can be considered are those with two and four boundaries.

Considering a system with just a pair of boundaries of separation n on a grid of length L and periodic boundary conditions, the value of Ξ will be given by

$$\Xi(\text{pair}; n) = A_b \left(2I_0 + I^1(n) + I^1(L-n) + 2I^2(L) + I^3(L+n) + \ldots \right) \tag{III.15}$$

where $\Xi(\text{pair}; n)$ is the value of $(\Xi - \Xi_0)$ for a system with a pair of boundaries separated by n. This can be approximated as

$$\Xi(\text{pair}; n) \approx A_b \left(2I_0 + I^1(n) \right). \tag{III.16}$$

Figure III.4 shows a fit of this equation to computed data points for n between 1 and 10 assuming that

$$I(n) = a/n \tag{III.17}$$

where a and I_0 are the only fitting parameters. The fit is extremely good, as can be seen, and this is the only justification offered here for the functional form chosen. The values produced from the fit are $I_0 = 0.121\,968$ and $a = -0.046\,493$. The nearest neighbour interaction is seen to be attractive, in contrast to the interaction required for a Bak–Bruinsma staircase, but stronger electronic effects will prevent the boundary-boundary separation becoming other than two or three.

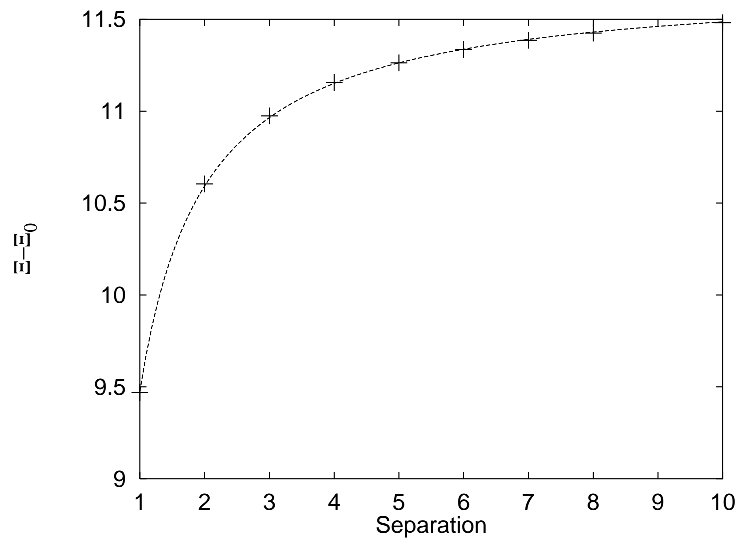

Figure III.4: $\Xi - \Xi_0$ in 2D as a function of boundary separation n for an isolated pair of boundaries on a 120x48 grid, and a fit of $A_b(2I_0 + a/n)$.

III.3.3 Next nearest neighbour interaction

Having thus found the nearest–neighbour interaction, the next–nearest–neighbour interaction is now sought. This is obtained through consideration of a triplet of boundaries, as shown in figure III.3. Again considering just the most important terms contributing to Ξ, and removing Ξ_0,

$$\Xi(\text{triplet}; n) \approx A_b \left(4I_0 + 2I^1(n) + I^2(2n)\right) \tag{III.18}$$

or

$$I^2(2n) \approx \left(\Xi(\text{triplet}; n) - 2\Xi(\text{pair}; n)\right)/A_b. \tag{III.19}$$

The work described in section II.5 suggests that

$$I^2(n) \approx -I^1(n) \tag{III.20}$$

so table III.1 is constructed to test this theory.

This table agrees broadly with the prediction, being correct in sign and to within 25% in magnitude. For the purposes of correcting the error from the omitted terms, it would now be justifiable to assume that equation (II.8) is correct and that intervening boundaries just cause an alternation in the sign of $I^j(n)$. The next nearest neighbour interaction is thus repulsive, and will tend to keep the boundaries at equal spacing, and encourage the formation of a staircase.

n	$\Xi(\text{pair}; n)$	$\Xi(\text{triplet}; n)$	$A_b I^2(2n)$	$-A_b I^1(2n)$	difference
1	9.469743	20.137265	1.197778	1.104695	7.77%
2	10.604305	21.842675	0.634064	0.554107	12.61%
3	10.974105	22.394945	0.446736	0.374629	16.14%
4	11.154893	22.660211	0.350425	0.284108	18.92%
5	11.262581	22.814170	0.289007	0.228215	21.03%

Table III.1: Calculation of next–nearest–neighbour interactions in 2D, and comparison with nearest–neighbour interaction.

n	$\Xi(\text{pair}; n)$	$\Xi(\text{triplet}; n)$	$A_b I^2(2n)$	$-A_b I^1(2n)$	difference
1	9.469743	20.137265	1.131678	1.104695	2.38%
2	10.604305	21.842675	0.567964	0.554107	2.44%
3	10.974105	22.394945	0.380636	0.374629	1.58%
4	11.154893	22.660211	0.284325	0.284108	0.08%
5	11.262581	22.814170	0.222907	0.228215	-2.38%

Table III.2: More refined calculation of next–nearest–neighbour interactions in 2D, and comparison with nearest–neighbour interaction.

Returning to the pair of boundaries, equation (III.15) can now be approximated as

$$\Xi(\text{pair}; n) \approx A_b \left(2I_0 + I^1(n) + n^2 \left. \frac{\partial^2 I(x)}{\partial x^2} \right|_L + \dots \right) \tag{III.21}$$

Thus equation (III.16) was a better approximation to equation (III.15) than could have been initially justified, because the omitted terms tend to cancel.

For the triplet structure the cancellation is not complete. Indeed, the group of three boundaries acts like a single boundary when viewed from a long distance, leaving

$$\Xi(\text{triplet}; n) = A_b \left(4I_0 + 2I^1(n) + I^2(2n) + 2I(L/2) \right). \tag{III.22}$$

A new table for $I^2(n)$ can then be produced from the formula

$$I^2(2n) \approx \left(\Xi(\text{triplet}; n) - 2\Xi(\text{pair}; n) - \Xi(\text{pair}; L/2) \right) / A_b + 2I_0. \tag{III.23}$$

With this correction in place, table III.2 is produced. The agreement now is very good between the calculated free energy of the triplet system, and that predicted from the pairwise interactions. This adds considerable justification to equation (II.8).

III.3.4 Further interactions

Calculation of further interactions, such as $I^3(n)$, becomes increasingly difficult as systems containing the term of interest also contain an increasing number of larger terms. The theory of section II.5.2 summarised in equation (II.8) on page 19 suggests that the interaction should continue to alternate in sign. Two simple tests are now performed to give a rough check on this prediction.

First $I^3(n)$ is calculated directly from a group of four boundaries, each a distance n from its neighbours. The expression for Ξ in this case is

$$\begin{aligned}\Xi(\text{quad}; n) &= 4I_0 + 3I^1(n) + 2I^2(2n) + I^3(3n) + \dots \\ &\approx 4I_0 + 2a/n + I^3(3n)\end{aligned} \quad \text{(III.24)}$$

with all the terms of the form $I(L)$ tending to cancel.

As a brief check $I^3(3)$ and $I^3(6)$ was calculated from this equation. The prediction that $I^3(n) = I^1(n)$ gave the same sign, and the same magnitude to within $12\frac{1}{2}\%$.

Rather than continuing to look at groups of five, six, seven, eight and more boundaries, and extracting $I^4(n)$, $I^5(n)$, etc., this analysis of the interactions beyond $I^2(n)$ is rounded off by considering a system which includes all higher interactions at once. Considering the grid of length L to be filled with boundaries at a separation of n, where $2n$ is a factor of L, this will produce a Ξ given by

$$\Xi(\text{grid}; n) = \frac{L}{n} I_0 + \sum_{pairs} I^j(m). \quad \text{(III.25)}$$

By recognising that every boundary contributes identically to the sum, this may be re-written as

$$\begin{aligned}\Xi(\text{grid}; n) &= \frac{L}{n}\left(I_0 + \sum_{j=1}^{\infty} I^j(jn)\right) \\ &= \frac{L}{n}\left(I_0 + \frac{a}{n}\sum_{j=1}^{\infty}\frac{(-1)^{j+1}}{j}\right). \\ &= \frac{I_0 L}{n} + 0.693\,147\frac{aL}{n^2}.\end{aligned} \quad \text{(III.26)}$$

The energy of the full grid was calculated for n taking all possible values between 2 and 20, subject to $2n$ being a factor of 120. From equation (III.26) best-fit values for I_0 and a were calculated as 0.1218 and –0.04483 respectively. These results are completely independent of the previous results of 0.1220 and –0.04649, but in good agreement with them. The data are

Boundary spacing	$\Xi - \Xi_0$	Fitted result
2	305.971	306.059
3	214.154	213.982
4	164.302	164.215
5	133.182	133.161
6	111.940	111.962
10	68.266	68.370
12	57.100	57.224
15	45.842	45.978
20	34.513	34.633

Table III.3: An independent fit of equation (III.26) to a grid full of uniformly spaced boundaries.

shown in table III.3.

In summary, the relation $I^j(n) = (-1)^{j+1} I^1(n)$ has been justified by theory and calculation, and the form $I(n) = a/n$ justified by calculation only. The "best" values of the fitting parameters are taken to be those given by the isolated pair of boundaries on a grid, that is

$$\begin{aligned} I_0 &= 0.121\,968 \\ I(n) &= a/n \\ &= -0.046\,493/n. \end{aligned} \tag{III.27}$$

III.3.5 Existence of phases in this model

After the above work in finding the form of Ξ, the total free energy of the system can now be expressed as

$$F_{tot} = F_0 + \frac{1}{2}kT\Xi + NE_{el} \tag{III.28}$$

where N is the number of atoms, and E_{el} represents an electronic, that is a non-phonon contribution to F_{tot}.

Choosing to focus on the $<2>$ to $<3>$ transition which is so important in SiC, and assuming that electronic interactions do not extend beyond four layers (see appendix D), E_{el} can be written as

$$E_{el} = 3E_{el,<3>} - 2E_{el,<2>} + 6\rho[E_{el,<2>} - E_{el,<3>}] \tag{III.29}$$

where ρ is the linear density of boundaries. Defining $\tilde{F}$ as a shifted F per atom, with the terms independent of polytypes removed from both the phonon and electronic free energy

Polytype	ρ	$\rho I_0 + S_{<>}$
<2>	$\frac{1}{2}$	0.052927
<2223>	$\frac{4}{9}$	0.047597
<23>	$\frac{2}{5}$	0.043306
<233>	$\frac{3}{8}$	0.040990
<232333>	$\frac{3}{8}$	0.040978
<2333>	$\frac{4}{11}$	0.039918
<3>	$\frac{1}{3}$	0.037075

Table III.4: Phonon contribution to the free energy of various polytypes in 2D.

results in

$$\tilde{F} = \frac{1}{2}kT\left(\rho I_0 + \frac{1}{N}\sum_{i,j} I^{j-i}(r_i - r_j)\right) - \rho\Delta E_{el} \tag{III.30}$$

where r_i is the position of the ith boundary, and

$$\Delta E_{el} = -6[E_{el,<2>} - E_{el,<3>}]. \tag{III.31}$$

It is then possible to consider $\tilde{F}$ for each polytype in the limit of infinite system size by defining a polytype dependent sum

$$S_{<>} = \lim_{N\to\infty}\frac{1}{N}\sum_{i,j} I^{j-i}(r_i - r_j) \tag{III.32}$$

so that

$$\tilde{F}_{<>} = \frac{1}{2}kT\left(\rho I_0 + S_{<>}\right) - \rho\Delta E_{el}. \tag{III.33}$$

The stable polytype at a given T will be the one with the minimum $\tilde{F}$ and hence the minimum F.

The electronic term ΔE_{el} is necessary to produce any phase transitions at all. Without it, all polytypes have the same free energy at $T = 0$, and nowhere else.

From the results for the form of $I^j(n)$, it is now possible to calculate $\rho I_0 + S_{<>}$ for various polytypes in two and three dimensions. This is shown in table III.4 for the two dimensional case.

Two of the polytypes selected in this table have the same value of ρ. For this pair, the one with the lower $S_{<>}$ or $\rho I_0 + S_{<>}$ will be stable with respect to the other at all temperatures, as the electronic contribution depends on ρ only. Thus <232333> is stable with respect to <233>. This follows the suggestion of Cheng *et al.* [48] that this sort of interaction will favour polytypes with an even number of layers in their repeat structure – that is an even number

of symbols in their Zhdanov notation.

Two phases a and b will be in equilibrium if they have the same $\tilde{F}$, that is if

$$\frac{1}{2}kT\left(\rho_{<a>}I_0 + S_{<a>}\right) - \rho_{<a>}\Delta E_{el} = \frac{1}{2}kT\left(\rho_{<b>}I_0 + S_{<b>}\right) - \rho_{<b>}\Delta E_{el} \tag{III.34}$$

or

$$T = \frac{2\Delta E_{el}\left(\rho_{<a>} - \rho_{<b>}\right)}{k\left(\rho_{<a>}I_0 + S_{<a>} - \rho_{<b>}I_0 - S_{<b>}\right)}. \tag{III.35}$$

Hence ΔE_{el} sets the scale for T. If $\Delta E_{el} = 0$ there is no phase diagram, and for positive transition temperatures ΔE_{el} must be positive, because the sign of the denominator is dominated by the I_0 terms where I_0 is positive. For convenience when plotting the phase diagram, two reduced variables are introduced,

$$\begin{aligned} T' &= \frac{kT}{2\Delta E_{el}} \\ \tilde{F}' &= \frac{\tilde{F}}{\Delta E_{el}} \end{aligned} \tag{III.36}$$

so that

$$\tilde{F}'_{<>} = T'\left(\rho I_0 + S_{<>}\right) - \rho. \tag{III.37}$$

The reduced free energies of several polytypes in 2D are shown in figures III.5 and III.6. The figures show that <23> does have a short range of stability, whereas the other intermediate phases do not. In this case the fractional width of the region of stability of <23>, that is ΔT divided by the transition temperature, is about 0.03.

III.3.6 Interpretation of results

From the disappointing performance of the one dimensional model, this 2D model has reclaimed much of the behaviour of silicon carbide. The phase <3> is found to be the high temperature phase, and <2> the low temperature phase. <23> is, perhaps surprisingly, the only intermediate phase to be found, but this would not be in contradiction to the experimental observations. Assuming ΔE_{el} were such that the transition occurred around 2400K, <23> would be stable over about 70K. This temperature range is rather smaller than the 500K predicted by Cheng [48], but would fit better with the experimental difficulty in growing <23>, which, for non-epitaxial growth, is almost never the dominant polytype. The favouring of “even” phases is also in agreement with previous predictions.

The other important conclusion is that phonons can give rise to a long range interaction between boundaries, as was previously predicted, but not demonstrated.

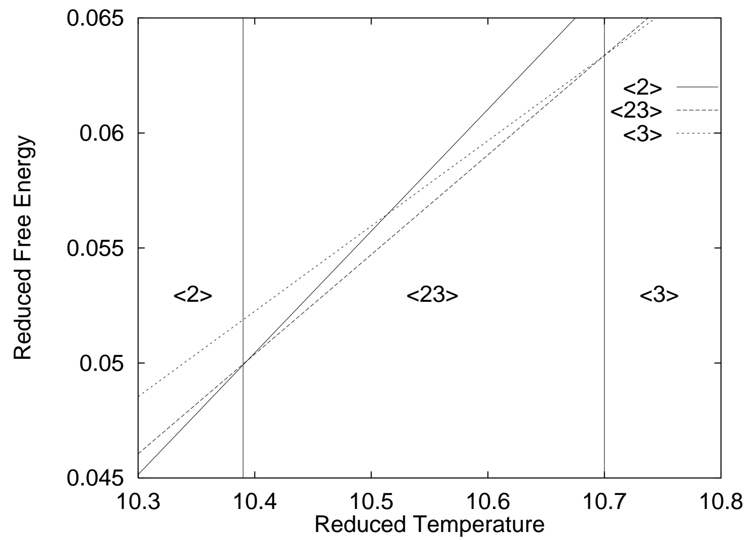

Figure III.5: Phase diagram from 2D interaction showing <2>, <23> and <3> and their regions of stability, in terms of the reduced variables defined in equation (III.36).

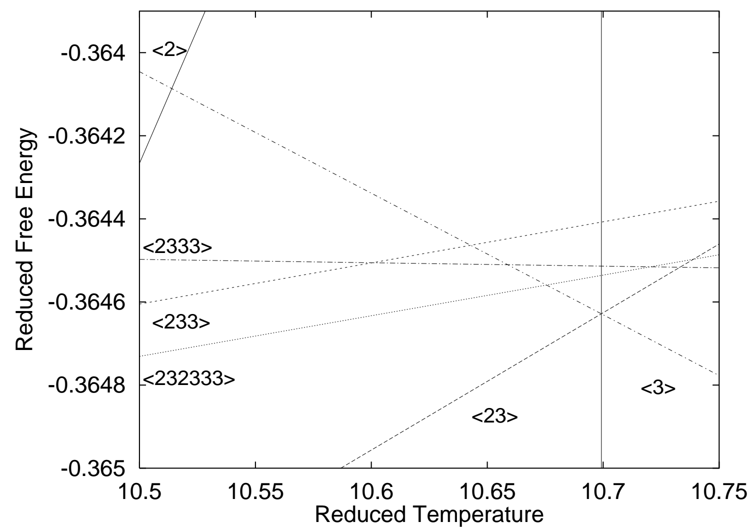

Figure III.6: Detail of transition from <23> to <3> for the 2D case. There is no intermediate phase here. A linear term of $0.04T'$ has been removed from all lines.

n	$\Xi(\text{pair}; n)$	$\Xi(\text{triplet}; n)$	$A_b I^2(2n)$	$-A_b I^1(2n)$	difference
1	72.455285	146.581542	1.555471	1.471855	5.38%
2	76.478145	153.437573	0.365784	0.338992	7.32%
3	77.314939	154.890294	0.144917	0.136557	5.77%
4	77.611008	155.409684	0.072169	0.072406	-0.33%
5	77.744361	155.642762	0.038540	0.043356	-12.50%

Table III.5: Calculation of next–nearest–neighbour interactions in 3D, and comparison with nearest–neighbour interaction.

III.4 3D model

Although the above model has reproduced much of the behaviour of silicon carbide, it is a two dimensional model. Using a model with three dimensions should move closer to real silicon carbide, so that is done here.

III.4.1 Description

The extension to three dimensions is achieved by taking layers of figure III.2, retaining x as the unique axis, and stacking them on top of one another in the z direction perpendicular to the page. In order to stabilise the structure, two diagonal springs are added across every square in the yz and xz planes.

The calculations then follow as before, except that a grid size of $120 \times 29 \times 29$ is now used, yielding a Ξ_0 of over 462 000.

III.4.2 Interactions

The variation of $\Xi - \Xi_0$ as a function of separation for a system with two boundaries is shown in figure III.7, fitted extremely well by the function

$$\Xi - \Xi_0 = A_b \left(2I_0 + \frac{a}{n^2} \right) \tag{III.38}$$

with $I_0 = 0.046\,343$ and $a = -0.006\,561$.

The interaction with a second neighbour boundary is determined again from equation (III.23), and is compared with $-I^1(n)$ in table III.5. The agreement is not as good as in the 2D system, indicating that the approximation of section II.5 about the I^2 interaction does not apply as closely in 3D as in 2D

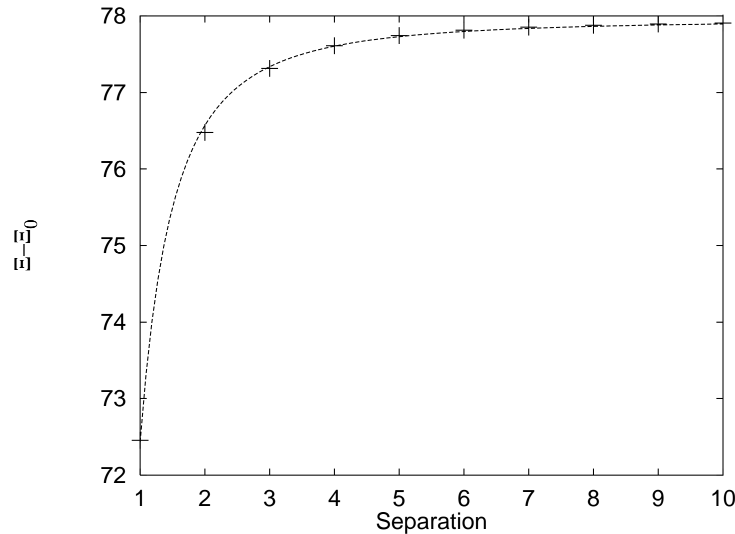

Figure III.7: $\Xi - \Xi_0$ in 3D as a function of boundary separation n for an isolated pair of boundaries on a $120 \times 29 \times 29$ grid, and a fit of $A_b(2I_0 + a/n^2)$.

III.4.3 Existence of phases in this model

For the $\pm n^{-2}$ interaction for 3D, the results are qualitatively the same as for the 2D case described in figures III.5 and III.6. The quantitative difference is that the width of stability of <23> is now only 0.006 times the transition temperature. This is to be expected, in that faster decaying interactions have been shown to produce more compact devil's staircases [63], and so in this case where the staircase is just a step, the step shortens. "Even" polytypes, such as <232333> are once more favoured over their "odd" counterparts with the same density of boundaries.

III.4.4 Interpretation of results

Again <23> is stable, and only <23> is stable between <2> and <3>. The width of stability, equivalent to just 14K if centred on 2400K, is rather smaller than the likely stability width in SiC. If the experimentally observed growth of <23> is due to its existence as an equilibrium phase, then the width of stability is probably around 50 to 100K to account for the sort of quantities obtained.

The free energy difference between <23> and a mixture of <2> and <3> is now very small — around $5 \times 10^{-6}kT$. This is still significant, for the stacking boundaries are forced to be flat due to the very high energy penalty, of the order of eV, of creating any kink on them. Thus all the atoms within one layer — a figure which could easily be over one million — act as a single unit in respect of this degree of freedom. This can be seen in electron micrographs

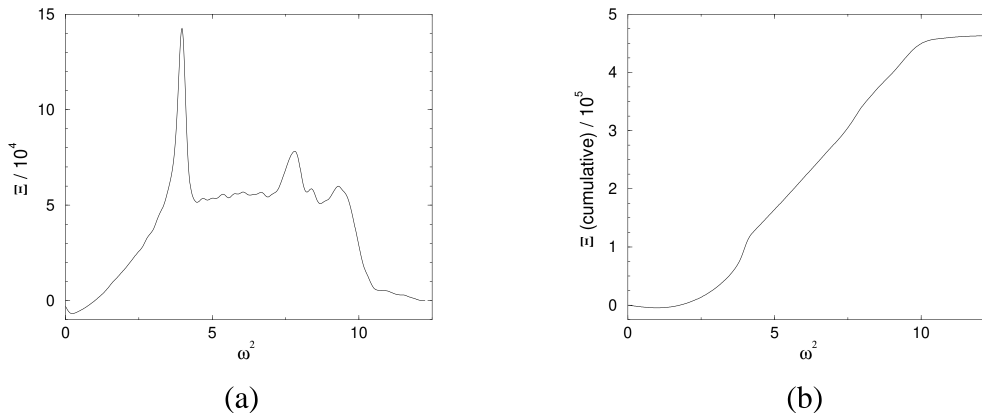

Figure III.8: The contribution to Ξ as a function of ω^2. In (a) is shown the density of Ξ in ω^2, and in (b) the integral of (a).

of SiC polytypes, such as that of a 6H / 3C interface by Nutt in Kong *et al.* [64]. It shows over a dozen stacking boundaries, each perfectly flat over the full extent of the micrograph (around 300 Å). The energy change on re-orienting such a unit can therefore be greater than kT.

III.5 Further analysis

III.5.1 How is ΔF spread over ω?

It had been suggested by Cheng *et al.* [48] that the contribution to the change in the free energy would not be uniformly spread throughout the spectrum, but rather concentrated at the low frequency long wavelength end. Work done by Short [65] suggested that this might not be the case and that the change might be spread throughout the spectrum. The following analysis seeks to resolve this issue.

The 3D calculations each produce just over 300,000 eigenvalues, each making a discrete contribution to Ξ. By smearing each contribution with a narrow gaussian, continuous graphs can be produced of the density of Ξ in ω^2 and the cumulative density. These are shown as figure III.8. On the scale of these figures the different boundary configurations produce no noticeable change. The final value of the cumulative graph is therefore approximately Ξ_0.

Figure III.9 shows how the cumulative contribution to Ξ changes as two boundaries are moved apart. Part (a) of the figure shows the difference between two systems with a pair of boundaries, one with the separation equal to two units, the other four units. The total change is, from table III.5, $76.48 - 77.61 = -1.13$. This change is not concentrated in any one part of

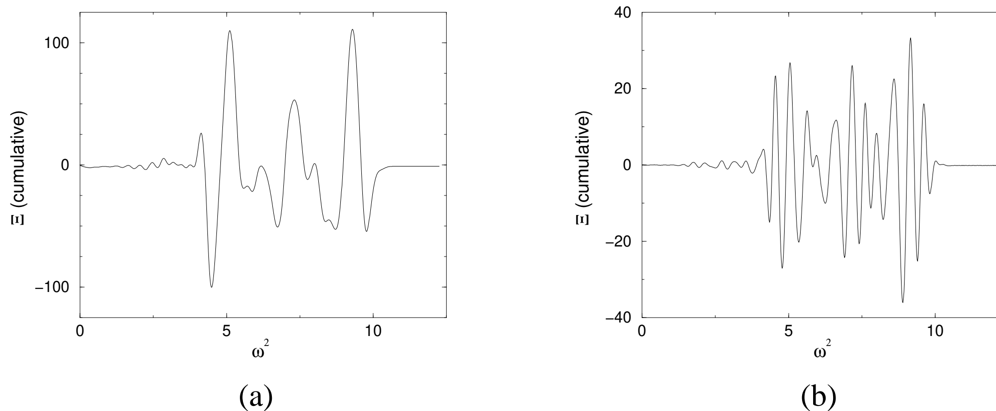

Figure III.9: Differences in the integrated density of Ξ as a function of ω^2. In (a) is shown the difference caused by increasing the separation of a pair of boundaries from 2 to 4, and in (b) from 8 to 10.

the spectrum — indeed, the changes in regions of the spectrum are one hundred times greater than this. Part (b) shows the difference between boundaries at eight and ten units. Again there is no obvious concentration at low frequencies, and although the boundaries are now three times further apart it does not seem to be the case that the contribution to the change in Ξ is coming from phonons of lower ω. These graphs emphasise how slight the change in Ξ is compared to its absolute value or even to changes within the spectrum.

III.5.2 The relation to the layer spin model

In section II.5 spin models based on both layers and boundaries were described, and in equation (II.7) a relationship was given expressing the boundary interaction I in terms of the layer interaction J. Having now found the form of I, a crude inversion of this equation is performed in order to find the form of J. Firstly, the sum is converted into an integral.

$$\begin{aligned} I_m &= -4 \sum_{n=m+1}^{\infty} (n-m) J_n \\ I(m) &\approx -4 \int_{m+1}^{\infty} (x-m) J(x) dx \end{aligned} \qquad \text{(III.39)}$$

This expression is then differentiated with respect to m twice.

$$\begin{aligned} \frac{\partial I(m)}{\partial m} &= 4J(m+1) + 4 \int_{m+1}^{\infty} J(x) dx \\ &\approx 4 \int_{m}^{\infty} J(x) dx \end{aligned}$$

$$\frac{\partial^2 I(m)}{\partial m^2} = -4J(m) \tag{III.40}$$

Considering first the two dimensional result of $I(n) = a/n$, this produces

$$J_m = \frac{-a}{2n^3}. \tag{III.41}$$

Furthermore, this can be substituted back into equation (II.5) from page 19 to give

$$\begin{aligned} I_0 &= -a \sum_{n=1}^{\infty} \frac{1}{n^2} \\ &\approx -1.65a \\ &= 0.0767 \end{aligned} \tag{III.42}$$

This result is almost a factor of two away from the measured value of I_0 of 0.122, but this error should not be too surprising. Equation (III.39) is not a very accurate way of turning sums into integrals. These sums are dominated by the first couple of terms which lie close to a pole of the function being summed — the conversion of a sum to an integral when one limit lies so close to a pole should be done much more carefully than this, especially as J_1 is not included in equation (III.40), but is obtained by extrapolation.

Ignoring these points and progressing straight to the three dimensional result of $I(n) = a/n^2$, the following is achieved:

$$\begin{aligned} J_m &= \frac{-3a}{2n^4} \\ I_0 &= -3a \sum_{n=1}^{\infty} \frac{1}{n^3} \\ &\approx -3.6a \\ &= 0.0236. \end{aligned} \tag{III.43}$$

The measured value of I_0 is again almost a factor of two greater at 0.0463.

This rough analysis (a better analysis would be significantly more complex) has not only reproduced the sign and order of magnitude of I_0, but it has also suggested the form of J_m. This latter point was a matter of conjecture for Cheng *et al.* [48], who wondered whether J_m decayed more slowly than $2^{-m/3}$ in order that certain long period polytypes might be stable. The answer for this model is a clear "yes."

III.5.3 Is <n n+1> stable in general?

Having shown for two specific cases that <23> occurs as an intermediate phase between <2> and <3>, it is natural to wonder whether this result is more general. Indeed it is, and there follows a proof that the phase <n n+1> will occur between the phases <n> and <n+1> for interactions of the form

$$I^j(n) = (-1)^{j+1} n^{-\alpha} \tag{III.44}$$

for integer values of α between one and four, and probably all positive α.

The proof for the case of $\alpha = 1$ is now given in full.

The free energy of a polytype <n> was given by equation (III.33) as

$$\tilde{F}_{<n>} = \frac{1}{2} kT \left(\rho_{<n>} I_0 + S_{<n>}\right) - \rho_{<n>} \Delta E_{el} \tag{III.45}$$

and there must exist some T_c at which $\tilde{F}_{<n>} = \tilde{F}_{<n+1>}$, that is at which <n> and <n+1> are mutually in equilibrium.

At this T_c, a system can exist which is partially <n> and partially <n+1>. Such a system, consisting of a fraction χ of <n> and $1 - \chi$ of <n+1> would have a free energy given by

$$\tilde{F}_{\text{mix}} = \frac{1}{2} kT_c \left(\rho I_0 + \chi S_{<n>} + (1-\chi) S_{<n+1>}\right) - \rho \Delta E_{el} \tag{III.46}$$

where ρ is simply the density of the boundaries in the mixture. If $\chi = n/(2n+1)$ then ρ is the same as that for the polytype <n n+1>. If <n n+1> is to be stable, its free energy must be less than that of the mixture of <n> and <n+1>. In other words

$$S_{<n\,n+1>} < \frac{n}{2n+1} S_{<n>} + \frac{n+1}{2n+1} S_{<n+1>} \tag{III.47}$$

Considering the case of the $\pm 1/n$ interaction, that is the 2D case, and ignoring the multiplicative constant a in the definition of $S_{<>}$ (equation (III.32)), then

$$\begin{aligned}
S_{<n>} &= -\frac{1}{n} + \frac{1}{2n} - \frac{1}{3n} + \frac{1}{4n} - \ldots \\
S_{<n+1>} &= -\frac{1}{n+1} + \frac{1}{2n+2} - \frac{1}{3n+3} + \frac{1}{4n+4} - \ldots \\
2S_{<n\,n+1>} &= -\frac{1}{n} + \frac{1}{2n+1} - \frac{1}{3n+1} + \frac{1}{4n+2} - \\
&\quad -\frac{1}{n+1} + \frac{1}{2n+1} - \frac{1}{3n+2} + \frac{1}{4n+2} - \ldots
\end{aligned} \tag{III.48}$$

These expressions may be manipulated to give

$$\frac{2n}{2n+1}S_{<n>} + \frac{2n+2}{2n+1}S_{<n+1>} = -\frac{2}{n+\frac{1}{2}} + \frac{2}{2n+1} - \frac{2}{3n+\frac{3}{2}} + \frac{2}{4n+2} - \dots \qquad \text{(III.49)}$$

and

$$2S_{<n\,n+1>} = -\frac{1}{n} - \frac{1}{n+1} + \frac{2}{2n+1} - \frac{1}{3n+1} - \frac{1}{3n+2} + \frac{2}{4n+2} - \dots \qquad \text{(III.50)}$$

Performing the comparison termwise, the condition for <n n+1> being stable reduces to

$$-\frac{1}{n} - \frac{1}{n+1} < -\frac{2}{n+\frac{1}{2}} \qquad \text{(III.51)}$$

and similar terms, all of which are clearly true. Thus <n n+1> is a stable with respect to <n> and <n+1> at some temperature for the $\pm 1/n$ interaction.

This analysis has been repeated for α equal to 2, 3 and 4 with the aid of computer–assisted algebra. The conclusion is that <n n+1> always has a stability range. The important value of α is 2, that corresponding to 3D.

These results were checked for the cases of <1> to <2> and <3> to <4> transitions, where the intermediate phases <12> and <34> were found, and, incidently, again no other intermediate phases could be found.

III.5.4 What deficiencies does this model have?

Although this model has been remarkable successful, it is necessary to comment on its possible deficiencies. The geometry is still wrong, even if the dimensionality is correct. Silicon carbide consists of two atomic species, each bonded to four equidistant nearest neighbours in a tetrahedral arrangement, with layers stacking not above each other but displaced by one third of $\mathbf{a}+\mathbf{b}$. This model has one atomic species, each atom bonded to six nearest neighbours and ten next nearest neighbours in a cubic arrangement, with layers stacking directly above each other. Further more, the model has purely quadratic potentials and uses the high temperature classic limit for the phonon free energy.

Why then is the model any good at all? Two factors are in its favour. Firstly, the high temperature limit of the phonon free energy is reasonably justified above the Debye temperature. Silicon carbide has a high Debye temperature of 1270K [2] but this is still lower than the temperatures of interest which are around 2400K.

Secondly, the form of $I(n)$ found can be expected to be general, not just because of the

extreme regularity of the result of n^{1-d} for $d = 1, 2, 3$, but also because of an alternative approach to the deduction of phonon spectra. If the spectrum were to be analysed in terms of lattice waves, only the scattering properties of the boundaries would be the important in determining the spectral differences on moving the boundaries. These scattering properties will be qualitatively universal, and thus these results for the interaction should be so too.

III.5.5 Conclusion

A simple phonon model has been presented which gives rise to a temperature dependent interaction between stacking boundaries which is long–ranged, decaying as $1/n^2$ in three dimensions, and which alternates in sign as intervening boundaries are traversed. For this interaction the existence of a range of stability of <n n+1> with respect to <n> and <n+1> is proven. A search for other intermediate phases between <2> and <3> was unsuccessful, so this interaction does not result in a devil's staircase.

Direct application of this result to lead iodide, where Salje *et al.* [21] observed a reversible phase transition and attributed it to changes in the phonon free energy is prevented by the different geometry of PbI_2. The phase transition observed was between 2H and 12R, with 4H being the possible high temperature phase. In Zhdanov notation the sequence is <1>, <13>, <2>. Lead iodide consists of stacked layers of iodide ions, with alternate layers having a layer of lead ions between them. The separation of the iodide layers alternates, and the ionic character of the crystal could produce important interactions over such short spacings as one, two and three iodide layers. Thus a study of the electronic energies of the PbI_2 polytypes would be required before this phonon model could be applied, but this work would suggest that such a study would give <12> a prohibitively high energy.

Chapter IV

Polytype Energies from *ab Initio* Electronic Structure Calculations

The previous chapter examined the possibility of phonon stabilisation of polytypes causing different polytypes to occur at different temperatures. This chapter considers the relative stability of different polytypes due to their electronic energies at 0K, and serves as an introduction to high accuracy self consistent electronic calculations.

IV.1 The aim of the calculations on SiC

IV.1.1 Why do *ab initio* calculations?

Ab initio calculations have improved enormously over recent years with the advent of greater computer power and advances in technique. It is now possible to calculate the energies and valence charge distributions of systems in their electronic ground state to a very high accuracy. There are limitations of this approach, but there are also many successes.

One major advantage of such "computer experiments" over real experiments is the very precise control over the system studied, and the ability to take measurements which cause no disturbance at all. Whereas in experimental work on SiC, for instance, impurity concentrations of around 100 ppm are considered low, in a computer simulation such impurities are completely absent. Indeed, including a species at a concentration of less than about 5% would be difficult. Similarly, the study of a particular polytype of SiC experimentally is hampered by the difficulty of growing specimens of most of the polytypes. In a computer simulation, properties of many polytypes can be investigated quite simply. This ability to study the

energetics and electronic properties of systems which are difficult to prepare, or even simply highly unstable, has many applications, especially in chemistry.

Another advantage of *ab initio* calculations arises from the sort of properties which they can calculate. Small energy differences between structures, energy differences as small as 1 meV per atom, are readily calculated, whereas their experimental determination, especially if no direct transformation between the structures exists, can be extremely difficult or even impossible.

Overlap between experiment and *ab initio* modelling does exist, and is important for testing and justifying the *ab initio* techniques. Lattice constants and bulk moduli are both readily calculated and experimentally determined, and reasonable agreement results. More complicated phenomena have been successfully modelled with *ab initio* techniques including, restricting reference to SiC only, selected phonon eigenfrequencies [59] the co-efficient of thermal expansion [66] and the Raman spectrum [67].

IV.1.2 Repetition of bulk calculations

Ab initio electronic calculations on SiC have been performed before, notably by the two groups of Heine [46, 68] and Bechstedt [47]. These calculations were on bulk polytypes, and the first part of this work repeats them, taking advantage of the improvements in technique and computing power available since the work of Prof. Heine's group in the late 1980's. For the first time the energy of 8H is included amongst other polytypes, allowing an estimation of the electronic contribution to J_4. The repetition also serves to test the present code and pseudopotentials.

IV.1.3 Surface calculations

The calculations on SiC surface energies form the most important part of this work. In these, growth is considered to be a layer–by–layer process, in which atoms at a surface can rearrange readily to find their minimum energy configuration, but atoms within the crystal are unable to move and thus the structure they attained on the surface is "frozen in." These calculations are discussed fully in the next chapter.

IV.2 The theory of *ab initio* calculations

The basic equation which needs to be solved in order to find the ground state energy of a system is the full electron–ion Schrödinger equation, in which the Hamiltonian is a function of all the electrons and nuclei in the system. The rest of this section describes how this can be simplified to solving an equation for non-interacting electrons, and how this simpler task can be approached for one particular choice of basis set. Finally, a description of the workings of CASTEP, the code used in this work, is given.

IV.2.1 The Schrödinger equation

The first simplification that can be made to the full electron–ion Schrödinger equation is the decoupling of the nuclei and electrons. The electrons are at least 2000 times less massive than the nuclei, and thus will respond to the movement of the nuclei "instantaneously" on the timescales of nuclear movement. The large mass of the nuclei also makes it possible to treat them as point particles with precisely known positions, as if they were classical particles. This decoupling is known as the Born–Oppenheimer approximation [69].

The equation which then results is

$$\hat{H}\Psi = \sum_i \left(-\frac{1}{2}\nabla_i^2 - \sum_n \frac{Z_n}{|\mathbf{r}_i - \mathbf{R}_n|} + \frac{1}{2}\sum_{j\neq i} \frac{1}{|\mathbf{r}_i - \mathbf{r}_j|} \right) \Psi = E\Psi \tag{IV.1}$$

where $\Psi = \Psi(\{\mathbf{r}_i\})$ is the many–electron wavefunction and the sum over n is a summation over the nuclei with charges Z_n and position vectors $\mathbf{R}_n$. The three terms in the Hamiltonian are the electronic kinetic energy, the electron–ion interaction and the electron–electron interaction respectively. The factor of $\frac{1}{2}$ in the last term prevents overcounting the electron–electron interaction. The units here are atomic units rather than SI. The nuclei simply provide an external potential for the electrons, with the energy due to the electrostatic interactions between the nuclei calculated classically separately.

IV.2.2 DFT & LDA

A major advance in the solution of the Schrödinger equation for interacting electrons was made by Hohenberg and Kohn [70] and Kohn and Sham [71], who proved that the equation could be mapped to an equation for non-interacting particles. The resulting Kohn–Sham

equation for the electronic energy is

$$E(\{\psi_i\}) = -\frac{1}{2}\sum_i \psi_i^* \nabla_i^2 \psi_i + \int \left[\frac{1}{2}\int \frac{\rho(\mathbf{r}')}{|\mathbf{r}-\mathbf{r}'|} d\mathbf{r}' + V_{ion}(\mathbf{r})\right] \rho(\mathbf{r}) d\mathbf{r} + E_{XC}[\rho(\mathbf{r})] \quad \text{(IV.2)}$$

where

$$\rho(\mathbf{r}) = \sum_i |\psi_i(\mathbf{r})|^2. \quad \text{(IV.3)}$$

Just like the Schrödinger equation, it can be solved by minimising the expectation value of the Hamiltonian, subject to the ψ_i's remaining orthogonal and normalised. Alternatively it can be solved as the eigenvalue problem

$$\left(-\frac{1}{2}\nabla^2 + \int \frac{\rho(\mathbf{r}')}{|\mathbf{r}-\mathbf{r}'|} d\mathbf{r}' + V_{ion}(\mathbf{r}) + V_{XC}[\rho(\mathbf{r})]\right) \psi_i(\mathbf{r}) = \epsilon_i \psi_i(\mathbf{r}) \quad \text{(IV.4)}$$

where

$$V_{XC}[\rho(\mathbf{r})] = \frac{\delta E_{XC}[\rho(\mathbf{r})]}{\delta \rho(\mathbf{r})}. \quad \text{(IV.5)}$$

This equation results from minimising equation (IV.2) subject to the constraint that the integrated charge density remains constant. The three non-kinetic terms, which correspond to the potential part of the Schrödinger equation, are called the Kohn–Sham potential, and are given by taking the functional derivative of the corresponding terms of equation (IV.2) with respect to $\rho(\mathbf{r})$.

$$V_{KS} = \int \frac{\rho(\mathbf{r}')}{|\mathbf{r}-\mathbf{r}'|} d\mathbf{r}' + V_{ion}(\mathbf{r}) + V_{XC}[\rho(\mathbf{r})] \quad \text{(IV.6)}$$

The effects of the exchange and correlation of the electrons are both included in the V_{XC} term, which is called the exchange–correlation potential. The many–body wavefunction must be antisymmetric under the exchange of two electrons of the same spin, and this results in the spatial separation of electrons of the same spin, and a corresponding reduction in their Coulombic repulsion. This reduction in energy is called the exchange energy. Similarly, even electrons of opposite spin correlate to avoid each other and so lower their Coulomb energy. This term is called the correlation energy. Kohn and Sham showed that the total exchange–correlation potential in the ground state is a functional of the electron density, $\rho(\mathbf{r})$, and does not depend explicitly on the individual wavefunctions. This scheme of writing the electronic energy as a functional of the electronic density is called density functional theory, or DFT.

The great utility of this result comes from the fact that the exchange–correlation potential is well represented by a function of the electron density, rather than a functional. This approximation is called the local density approximation (LDA), and was introduced by Hohenberg and Kohn. No theoretical form for the function is known, but various parameterisations exist which interpolate between the results calculated by Monte–Carlo methods for uniform density electron gases, such as the results of Ceperley and Alder [72] parameterised by Perdew and

Zunger [73] as used here.

More sophisticated approximations to the exchange–correlation potential, based on the gradient of $\rho(\mathbf{r})$ as well as its value, exist, and are known as generalised gradient approximations (GGA) [74, 75]. Although their use can produce improvements over LDA for isolated molecules, for bulk solids they do not offer a consistent improvement over LDA.

IV.2.3 Supercells & choice of basis set

In finding the functions ψ_i that minimise the energy of the Kohn–Sham equation above, the ψ_i's are expanded in a finite set of basis functions, and the best solution within that basis set found. The true ground state wavefunction must lie lower in energy than the solution constrained to lie within some artificial basis, but a sensible choice of basis set can yield a solution close to the true solution.

There are two distinct approaches to the choice of basis set. One is to expand the wavefunction in terms of atomic orbitals centred on each atom. A good description of a covalent system can be achieved with remarkably few Gaussian functions centred on each atom, and this is the basis of the Gaussian 94 code.[1]

This approach also has significant draw-backs. The basis functions are relatively complicated to manipulate, and change if the atoms are permitted to move. The basis set is also difficult to extend. The valence electrons of silicon, for instance, could be crudely described by a combination of functions corresponding to 3s and 3p orbitals. The next level of approximation would have to include all the orbitals in the region of the next energy level in silicon — 4s, 3d and 4p. Thus the number of basis functions per atom has jumped from four to thirteen. Finally, localised orbitals do not describe metallic states well, and the code used was designed for use with both metals and insulators.

The alternative approach is to use a basis set of plane waves. Whereas the atomic orbitals above are best for describing isolated molecules, plane waves are best for describing the non-localised states in periodic metal crystals. Plane waves are, however, simple to manipulate, independent of the atomic positions, and readily extended. One merely needs to consider all the plane waves with a kinetic energy below some arbitrary cut-off, which can be increased by any small or large amount.

Because plane waves are infinite in extent and periodic, they can describe only systems which also have these properties. Thus the electronic structure of a single, isolated molecule could not be described with a finite number of plane waves, although it could be described with

[1] Gaussian 94, Gaussian Inc., Pittsburgh, PA

localised Gaussian basis states. On the other hand an infinite crystal formed from the periodic repetition of a unit cell is an ideal subject for plane wave basis states.

The utility of plane waves is such that periodicity is often imposed on a system so that they can be used. For instance, if one wished to study a molecule, calculations could be made on a periodic grid of molecules, which would be physically equivalent provided that the separation between adjacent molecules was sufficient. The use of plane waves for aperiodic systems is discussed again in section V.2.1.

It is the plane wave approach that is used in this work, and which is now explained in a little more detail.

IV.2.4 Plane waves and k-points

Plane waves are useful as basis states only if the system studied has a periodic potential, as is the case for any crystalline solid. Bloch showed that the wavefunction in a periodic potential is itself the product of a cell-periodic part and a wave-like part [76].

$$\psi_{i,\mathbf{k}} = \exp(i\mathbf{k}.\mathbf{r})u_{i,\mathbf{k}}(\mathbf{r}) \tag{IV.7}$$

where u has the periodicity of the potential and $\mathbf{k}$ lies within the first Brillioun zone. By taking the discrete Fourier transform of u, the following equation is obtained:

$$\psi_{i,\mathbf{k}} = \sum_{\mathbf{G}} c_{i,\mathbf{k}+\mathbf{G}} \exp(i(\mathbf{k}+\mathbf{G}).\mathbf{r}) \tag{IV.8}$$

where $\mathbf{G}.\mathbf{l}$ is an integer multiple of 2π for all lattice vectors $\mathbf{l}$.

The infinite range of $\mathbf{G}$ and sampling density of $\mathbf{k}$ are both easily curtailed. The kinetic energy term of the Hamiltonian is proportional to the square of the wavevector. Hence states of high $|\mathbf{G}+\mathbf{k}|$ have high kinetic energy. Above some limit which will depend on the atoms present, this value will be so high that the weight in these basis functions will be negligible. Therefore only those states whose $|\mathbf{g}| = |\mathbf{G}+\mathbf{k}|$ lies below a certain value need be considered. This cut-off used is usually expressed in terms of the kinetic energy of the wavefunction at the cut-off, as

$$E_{cut} = \frac{p^2}{2m_e} = \frac{\hbar^2 g_{max}^2}{2m_e}. \tag{IV.9}$$

In order to calculate such quantities as $\rho(\mathbf{r})$ it would seem necessary to sum contributions to ρ from all $\psi_{i,\mathbf{k}}$'s, integrating over all $\mathbf{k}$'s in the Brillioun zone. The requirement to sample $\mathbf{k}$ at infinite density can be avoided by noting that similar values of $\mathbf{k}$ have similar wavefunctions

and thus contribute in a similar fashion to ρ. Thus one $\mathbf{k}$ value, or point, can represent a region in k-space, and the electronic charge density and hence Kohn–Sham potential can be accurately constructed by averaging over just a few k-points in the first Brillioun zone.

IV.2.5 k-space sampling and symmetry

It was shown above that the electronic wavefunctions can be expanded in a plane-wave basis set with no approximation given an infinite cut-off in k-space, and an infinitely dense sampling of the first Brillouin zone. It was further argued that the infinite cut-off could be reduced without too much loss of accuracy. Now the sampling of k-space will be considered.

Firstly it can be noted that because the Hamiltonian has the periodicity of the lattice, it does not mix between $\psi_{i,\mathbf{k}}$'s of different $\mathbf{k}$. That is to say that each $\mathbf{k}$ value can be considered independently of the others, with just the charge density being dependent on all $\mathbf{k}$'s as

$$\rho(\mathbf{r}) = \sum_{\mathbf{k}} w_{\mathbf{k}} \sum_i |\psi_{i,\mathbf{k}}(\mathbf{r})|^2 \tag{IV.10}$$

where $w_{\mathbf{k}}$ is the weight attached to the corresponding k-point.

Discrete sampling of continuous functions is common in computing, and is the basis of numerical integration, which, for "well–behaved" functions can be performed with arbitrary accuracy. In the same way, as long as for each band $\psi_{\mathbf{k}}$ is "well–behaved", discrete sampling of k-space should be sufficient. In metals, bands are partially filled, and the occupancy of a band may be a discontinuous function of $\mathbf{k}$, but in insulators the bands are smooth and continuous in their properties, and can be represented accurately by very few points.

Consideration of the Hamiltonian also reduces the number of separate k-points at which ψ needs to be calculated. Schrödinger's equation always exhibits time-reversal symmetry for any potential, so that $\psi_{-\mathbf{k}}$ is simply $\psi^*_{\mathbf{k}}$. As these functions make identical contributions to $\rho(\mathbf{r})$ and have identical eigenvalues, there is never a need to calculate $\psi_{\mathbf{k}}$ at both $\mathbf{k}$ and $-\mathbf{k}$. If both are required, one is calculated and its weight within the rest of the calculation doubled.

In a crystal, the potential provided by the ions may exhibit additional symmetry. If this is so, the symmetry elements in reciprocal space can be used to calculate ψ for any value of $\mathbf{k}$ related by a symmetry operation to a value at which ψ is known. In a cubic system, for instance, if ψ is known for the single k-point $(0.25, 0.25, 0.25)$, then, by rotation and inversion, it is known for the eight k-points given by all combinations of signs in $(\pm 0.25, \pm 0.25, \pm 0.25)$. Use of symmetry can thus reduce computational requirements by a significant factor. Indeed, it is not necessary to calculate each symmetry–related ψ explicitly, but rather the reciprocal space charge density can be symmetrised without reference to the ψ's from which it is constructed.

Various schemes exist for choosing an optimal set of k-points for different systems [77–79], producing sets for which the k-points do not necessarily have equal weights.

It is useful to have a measure of how "good" a particular set of k-points is, and just as one might say that a certain one dimensional integrator is exact for all polynomials up to fourth order, a similar terminology is sought here. Following the method of Monkhorst and Pack [79], a set of basis functions is constructed for expanding functions with the lattice periodicity. These functions are

$$A_n(\mathbf{k}) = \sum_{|\mathbf{R}|=C_n} e^{i\mathbf{k}.\mathbf{R}} \qquad \text{(IV.11)}$$

where the $\mathbf{R}$'s are lattice vectors, and $\{C_n\}$ is an ordered set of the moduli of all the lattice vectors. Hence the sum is over all lattice vectors of the same modulus — a "star" of vectors — and the modulus increases with increasing n. That these functions $A_n(\mathbf{k})$ are orthogonal and can be normalised is shown in reference [79].

One can further assume that any function $f(\mathbf{k})$ can be expressed in this basis as

$$f(\mathbf{k}) = \sum_{n=0}^{\infty} f_n A_n(\mathbf{k}). \qquad \text{(IV.12)}$$

The first of these basis functions is the constant function, and as n increases so does the rapidity with which the basis functions vary as a function of $\mathbf{k}$. Thus any function which is smooth should be accurately represented by just the first few terms of equation IV.12, with the higher coefficients decaying rapidly towards zero.

Thus a set of k-points can be tested by using it to integrate the basis functions $A_n(\mathbf{k})$ and recording the first value of n, or the corresponding value of C_n, for which the integral fails. This point is often called the "first failure star." This test is not a replacement for using the k-points in a real LDA calculation, but rather a means of comparing different k-point sets rapidly.

IV.2.6 Pseudopotentials

There is one further important simplification which dramatically decreases the amount of computational effect required in solving for a system's ground state, and that is the use of pseudopotentials rather than bare Coulombic potentials for the ions. Chemistry and physics both indicate that the inner electrons are almost unaffected by an atom's environment, whilst the outer electrons perform any bonding and determine the energy of the final configuration. Thus calculation of the wavefunctions and energies of, for instance, the ten electrons in the

inner two shells in silicon is wasted effort, as the result will be almost unchanged by any changes in the chemical environment of the atom.

But there is more to the use of pseudopotentials than merely throwing away the many of the electrons in a system. The wavefunctions of outer electrons contain radial nodes in the core region of the nucleus. Again these nodes are occurring in a region of space where the effect of neighbouring atoms is negligible, but more importantly these nodes, caused by the requirement of the outer electrons to be orthogonal to the inner electrons, introduce high frequency components into the wavefunction. However, the parts of the wavefunction which are involved in bonding are further from the core, and free of radial nodes. In order to get a good description of the interaction between two atoms, it is only necessary that the potential chosen for the core produces pseudo-wavefunctions $\psi_{ps,i}$ that are identical to the real wavefunctions ψ_i beyond some core radius r_c. In other words

$$\psi_{ps,i}(\mathbf{r}) = \psi_i(\mathbf{r}) \qquad |\mathbf{r}| > r_c \tag{IV.13}$$

and then the same energy eigenvalues will result, as long as the core regions do not overlap in the configuration chosen. As the pseudopotential, $V_{ps}(\mathbf{r})$, can be chosen to be equal to the real potential, $V(\mathbf{r})$, outside r_c, the above equation can be satisfied merely by ensuring that the value and first derivative of the two wavefunctions match at r_c. Such a comparison is shown in figure IV.1, where a 3s wavefunction and two corresponding pseudowavefunctions of different core radii are shown. Neither pseudowavefunction has any radial nodes, and the one which departs from the true wavefunction at the larger core radius is noticeably smoother, and thus could be described using fewer plane waves than the other. Both pseudopotentials have the same normalisation as the real wavefunction, resulting in the same total charge in the core region. This property, known as "norm–conservation", increases the *transferability* of the pseudopotential — that is, the ability to use the potential in differing situations [80]. Without some degree of transferability a pseudopotential would be useless, as one always wishes to use a pseudopotential in a situation where the exact self-consistent wavefunction and energy eigenvalues are unknown.

Pseudopotentials are in practice expressed in terms of angular momentum projectors. Once more considering silicon, an electron in an $l = 0$ orbit, such as 3s, must be orthogonal to the core electrons in the 1s and 2s orbitals, whereas an electron in an $l = 1$ state is already orthogonal to these core electrons and must orthogonalise itself to the 2p electrons. Hence these different electrons see different effective potentials from the core, and by expressing the potential in terms of angular momentum operators this can be reflected in the form of the potential.

This work uses norm conserving reciprocal space pseudopotentials in the Kleinman–Bylander

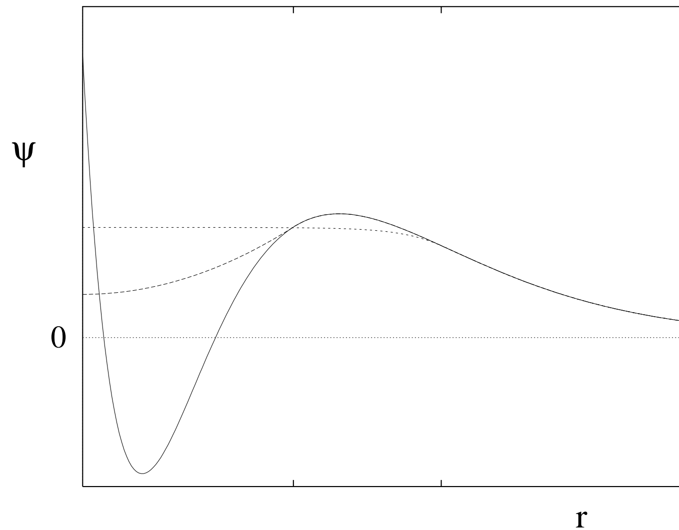

Figure IV.1: A 3s wavefunction (solid line), and two pseudowavefunctions (dotted).

form [81]. A review of the background and early use of pseudopotentials is given by Heine [82], with a later review being given by Denteneer and van Haeringen [83].

IV.2.7 FFT grids

The use of a plane wave basis set leads to much of the calculation being done in reciprocal space, where the basis set is trivial, and the kinetic energy operator is diagonal. However, some parts of the calculation still need to be done in real space, such as the construction of the real space charge density and hence the real space exchange–correlation potential. Thus much time is spent converting quantities between real and reciprocal space using fast fourier transforms (FFT's).

FFT's rely on discrete grids, and this seems at first to be a large approximation unless the grid is very fine. However, it must be remembered that $\psi(\mathbf{g})$ has no components above some cut-off value g_{max} determined by the energy cut-off employed in the basis set. Hence $\rho(\mathbf{g})$ will have no components above $2g_{max}$, and as long as the FFT grid includes all components up to $2g_{max}$ then the charge density at least can be transformed to and from reciprocal space with no loss of information. This is the criterion usually used in choosing an FFT grid size, and figure IV.2 shows its application to a hexagonal system. The figure is in reciprocal space, and the mesh represents the reciprocal lattice. Only points which lie on this lattice need to be considered. The circle represents the size of the highest frequency components which could occur in the charge density, and the bold parallelogram shows the size of the FFT mesh which would be needed to ensure that every point on the infinite reciprocal space grid lying

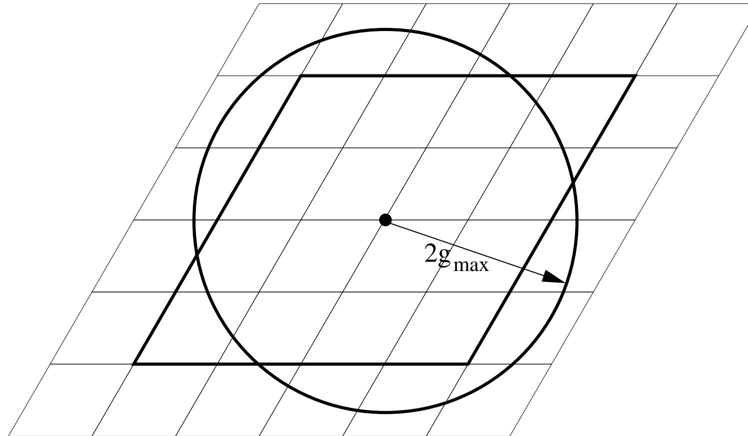

Figure IV.2: The reciprocal space lattice showing the possible extent of components of the charge density. The smallest grid which includes all points necessary to describe the charge density is outlined with a bolder line.

within $2g_{max}$ of the origin is included. In this case a 5×5 grid would be required. Of the 25 points on the FFT grid thus generated, 6 lie outside the circle, and are thus in some sense redundant. This sort of inefficiency is bound to occur, and is worse when the axes are far from being orthogonal.

Even quantities such as $\int \rho(\mathbf{r})d\mathbf{r}$ can be evaluated exactly in real space on such a grid. Slight errors do occur on evaluating more complex quantities, such as the exchange–correlation energy, in real space.

It is often sufficient to use a slightly smaller grid size than that given by the above argument, as the high $|\mathbf{g}|$ components of the charge density are very small compared to the lower $|\mathbf{g}|$ components. A figure of 80% of the above grid size is often quoted as being acceptable, and has the advantage of halving the time taken to do each FFT. This reduction in grid size is not used in this work, partly because of errors which it introduces into the forces on the atoms, as discussed in section V.4.2, and partly because of a slight complication which symmetry introduces.

In hexagonal systems such as those studied here the infinite reciprocal space FFT grid has a three-fold rotation axis. However, the finite grid used does not have this symmetry operation. Indeed, the rotation takes some points within the grid outside of the grid. This is shown in figure IV.2. When $\rho(\mathbf{g})$ is symmetrised, if the components at these points were zero anyway, this does not matter at all, but if these components were non-zero, then they need to be zeroed in order to ensure that the final $\rho(\mathbf{g})$ does have the rotational symmetry, and in zeroing them the symmetrised calculation becomes different from an unsymmetrised calculation using the full k-point mesh. Once this point is recognised, there is no particular reason not to used a

reduced mesh with symmetrisation, although it does prevent comparison with unsymmetrised results.

Sensible choices of FFT grid size are also limited to sizes with no prime factors other than 2, 3 and 5, for the FFT algorithm scales as $n \log n$ for sizes with many small factors, and n^2 for prime grid sizes. Indeed, many FFT implementations, including that which was in CASTEP, cannot use grid sizes with factors other than those listed above.

The FFT grid size is therefore one more factor which would ideally be infinite, but in practice can be quite small whilst retaining all necessary accuracy.

IV.2.8 CASTEP

CASTEP, the CAmbridge Serial Total Energy Package, is a FORTRAN code developed for performing calculations such as the above on metals and insulators, and used in this work. It has had a long history of development under Mike Payne, Victor Milman and many others, and follows closely the review of *ab initio* techniques given by Payne *et al.* [84]. There follows a brief description of the code as it was when this project was started.

CASTEP implements the methods discussed above, using pseudopotentials to solve for the ground state of a system via a plane wave basis set in the local density approximation, optionally relaxing the ions too. The minimisation of the Kohn Sham energy functional, equation IV.2, is carried out directly [85] using a conjugate gradients minimiser [86] one band at a time. This requires the construction of a potential, V, such that $V|\psi>$ is the functional derivative of the energy with respect to ψ. This is simply the Kohn–Sham potential of equation (IV.6) with the kinetic term restored, for, as $\rho(\mathbf{r}) = \psi^*(\mathbf{r})\psi(\mathbf{r})$

$$\frac{\delta E}{\delta \psi} = \frac{\delta E}{\delta \rho}\psi^*. \tag{IV.14}$$

The energy is then expressed as $<\psi|V|\psi>$ plus any necessary correction terms arising from the overcounting otherwise caused by the definition of V.

The minimisation is done band–by–band, followed by k-point by k-point, following the flow-chart expressed in figure IV.3. This is not the only possible scheme for such a code, and indeed Holender and Gillan[2] have developed a version which minimises over all bands simultaneously, leading to faster run times but greater store requirements.

One important characteristic of any such code is the manner in which its memory and CPU time requirements scale with system size. The following analysis considers this for CASTEP.

[2]J. Hollender and M. Gillan, University of Keele

```
Initialise the lowest energy components of $\psi_{i,\mathbf{k}}$'s randomly
Orthogonalise $\psi_{i,\mathbf{k}}$'s
Construct $\rho$ and $V_{KS}(\rho(\mathbf{r}))$

DO iteratively
   DO over k-points $\mathbf{k}$
      DO over bands $i$
         Minimise $< \psi_{i,\mathbf{k}}|\hat{H}|\psi_{i,\mathbf{k}} >$ for this $i$ and $\mathbf{k}$ using a conjugate gradients
            minimiser and keeping $\psi_{i,\mathbf{k}}$ normalised and orthogonal.
         Update $\rho$ and associated potentials
      NEXT band
   NEXT k-point
   Symmetrise $\rho$ and recalculate $V_{KS}(\rho(\mathbf{r}))$ if required
NEXT iteration
```

Figure IV.3: The electronic minimiser of CASTEP expressed in pseudocode.

As the plane wave cut-off energy is varied, the highest $|\mathbf{g}|$ included in the basis set increases as the square root of the cut-off energy equation (IV.9). The number of plane waves in the basis set will be the number of plane waves inside a reciprocal space sphere of radius $\sqrt{2m_eE_{cut}}$, the permitted plane waves being points on the reciprocal space lattice, plus the off-set of the k-point being considered. The number of such points within the sphere is the sphere volume divided by the volume of the reciprocal space unit cell, so the number of plane waves scales as cell volume $\times E_{cut}^{3/2}$.

For large systems, the memory requirement is dominated by the memory required to store a wavefunction, that is the number of bands times the number of plane waves, and the CPU time is dominated by the time taken to orthogonalise the update direction of a band to all other bands. This process scales as the square of the number of bands times the number of plane waves.

Most systems do not suffer this scaling, with the time taken to project out the angular momentum components of each band for the pseudopotential dominating. This is done for each pseudopotential, that is each atom, against the full wavefunction. For systems containing much vacuum, and therefore few atoms, the time taken to perform the FFT's may instead dominate. The number of FFT's required scales as the number of bands, and the time taken to do one as the number of plane waves (strictly $n \ln n$, not just n). This is summarised in table IV.1.

In all cases the run time is linear in the number of k-points used. This may introduce a factor of the reciprocal of the volume into these estimations of the timing, but in practice the reduction in the number of k-points needed for a large cell is often less than this, if only

Regime	CPU time scaling	When applicable
FFT limited	bands × volume $\times E_{cut}^{\frac{3}{2}}$	much vacuum
Projection limited	atoms × bands × volume $\times E_{cut}^{\frac{3}{2}}$	
Orthogonalisation limited	bands$^2\times$ volume$\times E_{cut}^{\frac{3}{2}}$	over ∼ 400 atoms

Table IV.1: CPU time scaling of CASTEP

because one cannot use fractional numbers of k-points. Most of the runs in this thesis are projection limited, verging on the FFT limited for the surface calculations.

IV.2.9 Serial or parallel?

Having described the code, there remains the choice of machine architecture — serial, vector or parallel. The FORTRAN CASTEP is written in vectorises readily under Cray's compiler, achieving 140 MFLOPS on a YMP/8 processor (peak performance 330 MFLOPS). There is also a parallel version called CETEP (Cambridge and Edinburgh Total Energy Package).

CETEP has the disadvantage that it does not perform symmetrisation. It stores the charge density distributed across all nodes, so that the symmetrisation routine would not only generate a lot of inter-node traffic, but would also have to keep careful track of which node each piece of the charge density was stored on. These problems are not insurmountable, but do make implementing symmetrisation to the parallel code more difficult and less beneficial than its implementation on the serial code. The surface calculations presented in chapter V with a $7 \times 7 \times 1$ k-point mesh required calculations at 8 k-points with symmetrisation, and would have required 25 k-points without (inversion symmetry may still be used). The difference is slightly larger for the bulk calculations in this chapter, the $7 \times 7 \times 4$ k-point mesh used for the cubic system requiring 26 k-points with CASTEP and 98 with CETEP.

For the bulk calculations the computational requirement is sufficiently small the a serial workstation is the natural choice, re-enforced by the four-fold greater efficiency of CASTEP over CETEP for these calculations. The surface calculations were originally planned for the vector Cray YMP/8 on which time was available and the benefits of symmetrisation could be realised. The parallel machine available, an Intel iPSC/860, would not have been significantly faster, having 64 nodes of 40 MFLOPS peak performance each, and also being shared amongst a large number of users.

Despite some time being spent on improving the vectorisation of the code and reducing its run-time on the YMP/8 by about 30%, in the end the calculations were performed on a DEC Alpha workstation, which had higher availability and accessibility than the Cray, and whose CPU performance was only a factor of five slower, with a rather smaller factor separating

their real-time performances.

IV.3 Technical improvement to the symmetry code

IV.3.1 Improvements to symmetry code

The code as described in figure IV.3 implements symmetry in a slightly odd fashion. The charge density is symmetrised at the end of minimising over all bands and k-points, rather than kept symmetric in a self-consistent manner. This was done because the symmetrisation is fairly expensive, and a more ideal scheme would increase the number of calls to the symmetriser by a factor of a hundred or so, for little gain in the swiftness of convergence. The current scheme does have one major disadvantage: the charge density is not correctly expressed as the symmetrised sum of the contributions from the individual bands and k-points throughout the calculation. After updating each band, the charge density is updated as though the band had contributed in an unsymmetrised fashion to the density. In other words, if no symmetrisation is applied,

$$\rho(\mathbf{r}) = \sum_{\mathbf{k}} w_{\mathbf{k}} \sum_{i} |\psi_{i,\mathbf{k}}(\mathbf{r})|^2 \tag{IV.15}$$

where $w_{\mathbf{k}}$ is the weight of the k-point $\mathbf{k}$ and $\psi_{i,\mathbf{k}}$ the wavefunction of the ith band at k-point $\mathbf{k}$. If one band is updated then

$$\rho(\mathbf{r}) \mapsto \rho(\mathbf{r}) + w_{\mathbf{k}} \left(|\psi_{i,\mathbf{k},new}(\mathbf{r})|^2 - |\psi_{i,\mathbf{k},old}(\mathbf{r})|^2 \right). \tag{IV.16}$$

Defining an operator $\hat{S}$ to represent the required symmetrisation, that is converting $\rho(\mathbf{r})$ to reciprocal space, symmetrising it, and reconverting to real space, the symmetrised versions of the above equations are

$$\rho(\mathbf{r}) = \hat{S} \sum_{\mathbf{k}} w_{\mathbf{k}} \sum_{i} |\psi_{i,\mathbf{k}}(\mathbf{r})|^2 \tag{IV.17}$$

and

$$\rho(\mathbf{r}) \mapsto \rho(\mathbf{r}) + w_{\mathbf{k}} \hat{S} \left(|\psi_{i,\mathbf{k},new}(\mathbf{r})|^2 - |\psi_{i,\mathbf{k},old}(\mathbf{r})|^2 \right) \tag{IV.18}$$

whereas the update equation used by CASTEP is still equation IV.16. This short-cut can produce pathological effects, including that of the density of the electrons becoming negative.

Although symmetrising after each band is updated would be prohibitively expensive, it was found that for some systems a significant improvement in convergence was obtained by reconstructing ρ correctly after each k-point, rather than after all k-points. This still leaves ρ in error once the first band is updated, but the error is not permitted to accumulate for so

Iteration	Energy (eV)	
	before	after
10	−789.7931669	−789.8010123
11	−789.7991350	−789.8010140
12	−789.8005455	−789.8010144
13	−789.8009209	−789.8010144
14	−789.8009907	−789.8010145
15	−789.8010085	−789.8010145
16	−789.8010133	−789.8010145
17	−789.8010137	−789.8010145
18	−789.8010126	−789.8010145
19	−789.8010092	−789.8010145
20	−789.8010002	−789.8010145
21	−789.8009756	
22	−789.8009088	
23	−789.8007268	
24	−789.8002328	
25	−789.7988888	
26	−789.7952393	
27	−789.7853132	
28	−789.7583702	
29	−789.7913315	
30	−789.7997715	

Table IV.2: Demonstration of convergence failure before the alteration to the symmetrisation was made.

long. An example of a system (3C SiC in a six-atom hexagonal cell) where the difference was significant is shown in table IV.2. The difference here is quite clear: with the correction convergence to 0.1 μeV is achieved in 14 iterations, without it convergence to 1 μeV is achieved in 17 iterations, after which the energy rises for the next ten iterations, rising by a total of over 40 meV, before once more falling. This shows starkly that with the old symmetry routine the energy is not guaranteed to fall iteration by iteration. In fact, the new routine can still offer no such guarantee — it merely remains well-behaved in more situations, and, indeed, in all situations encountered.

IV.4 Error cancellation & choice of parameters

IV.4.1 Error cancellation

Many approximations have been discussed above — the introduction of a finite basis set cut-off, the introduction of a discrete set of k-points, the use of a discrete FFT grid. These all

introduce errors, and great effort would be required in order to reduce the absolute error to the level of the energy differences usually sought. Most of the errors introduced will tend to cancel if the same parameters are used in the systems being compared. This is clearest in the case of the plane wave cut-off, where the high energy components are helping the wavefunction to concentrate in the region of the atomic core where the potential is strong, even after the use of pseudopotentials. This localisation will reduce the total energy noticeably, but is almost unaffected by the environment of the atom, so the error is determined by the number and types of the atoms, not their configuration, and hence cancels when structural energy differences are calculated. A similar argument can be offered for the high frequency components which the coarse FFT grid treats incorrectly, and even the k-point sampling enjoys similar error cancellation.

IV.4.2 Choice of pseudopotentials

Thanks and credit are due to M.-H. Lee for producing the pseudopotentials used in this work. The potentials had all been used before in other calculations, and had been shown to be reliable. The carbon potential had been developed to combine a high degree of transferability with a reasonably low cut-off, using Q_c filtering [87] and had been successfully tested in diamond[3], ethane, ethylene and acetylene[4]. The silicon potential had been slightly less well tested[5], and used a reduced number of angular momentum projectors in order to reduce CPU usage [87, 88]. The hydrogen potential used was a simple Coulombic potential.

IV.4.3 Choice of k-points

As mentioned above, there are many schemes for choosing k-points, and thus the method used here is not necessarily the only reasonable solution. As there is no *a priori* way of telling whether a k-point mesh was sufficiently dense, but rather one has to repeat the calculation with a denser one and see if convergence was achieved, it is useful to chose a set which is readily extendible.

The sets of the Monkhorst Pack method [79, 89] were chosen due to their ease of extension. These sets form uniform meshes in k-space, and are described by the number of points along each axis, so that in two dimensions there are sets of 1×1, 2×2, 3×3 k-points, and so on. Thus the total number of unsymmetrised k-points in these sets increases as n^2, and the step from one set to the next as n. The alternative sets, such as those of Chadi and Cohen [78],

[3] M.-H. Lee and V. Milman

[4] C. Goringe and A. Sutton, Oxford

[5] R. Perez successfully calculated a_0, B and $\partial B/\partial P$ for bulk Si.

or Cunningham [77], have far fewer intermediate sets. The first three Chadi Cohen sets for a two dimensional hexagonal lattice have 3, 6 and 18 points after symmetrisation, whereas Monkhorst Pack sets exist with 2, 3, 4, 5, 7, 8, 10, 12, 14, 16 and 19 points. Even comparison in terms of failure stars is unfavourable to Chadi and Cohen, with their 18 point set having the same failure star (see section IV.2.5) as the Monkhorst Pack 12 point set [89].

IV.5 Results

IV.5.1 Bulk calculations on Si & C

The application of the above theory, and the code and pseudopotentials to be used, are now tested by some simple bulk calculations on silicon, carbon (diamond), and silicon carbide. Silicon is the easiest system to work with, because its pseudopotential is much "softer" than that of carbon, that is, it needs fewer plane waves to describe the resulting pseudowavefunction. In the simple bulk calculations on Si, C and SiC no attempt will be made to justify the cut-offs or k-point meshes chosen — values which other researchers have found adequate are used. These choices are carefully investigated and justified when the energy differences between the SiC polytypes are calculated.

The lattice constant & bulk modulus of silicon

The first calculation presented is a simple test of the silicon pseudopotential. Using an eight atom cubic cell, the energy of bulk silicon is calculated at six different lattice constants, and from these the equilibrium lattice constant and bulk modulus found. These calculations use a 160 eV cut-off, a $4 \times 4 \times 4$ Monkhorst Pack k-point mesh, reducing to just four k-points after symmetrisation, and are based on an experimental lattice constant of 5.429Å [2]. The raw results are shown together with a fitted cubic in figure IV.4. A cubic is chosen as the minimum is expected to be asymmetric — a solid will resist compression more strongly than extension for all but the smallest strains.

The equilibrium lattice constant, that is the minimum of the energy curve, is readily found to be at 100.75% of the experimental result on simply fitting a quadratic to the data, or 100.69% on fitting a cubic polynomial. The bulk modulus may also be found as

$$\begin{aligned} \delta P &= B\frac{\delta V}{V} \\ B &= V\frac{\partial P}{\partial V} = V\frac{\partial^2 E}{\partial V^2} \end{aligned} \quad \text{(IV.19)}$$

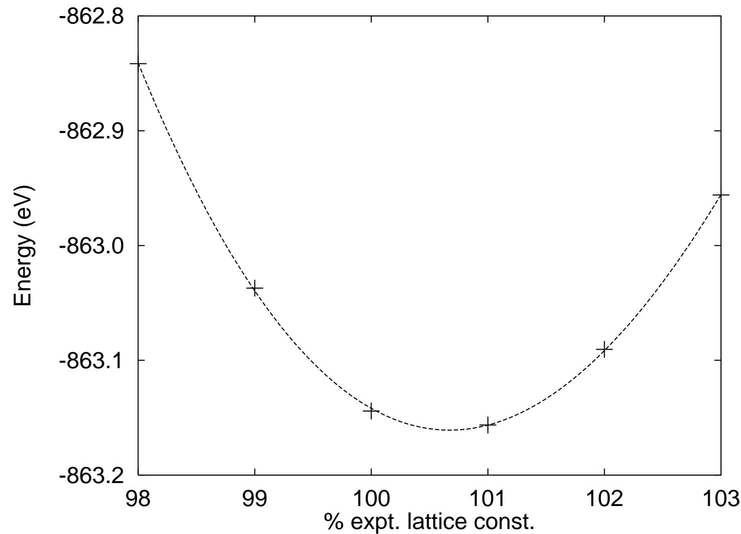

Figure IV.4: Energies of bulk silicon as a function of lattice constant, together with a fitted cubic.

where B is the bulk modulus, V the volume of the solid and P the pressure exerted by the solid. Considering this quantity for one unit cell of side xa_0 where a_0 is the equilibrium lattice constant, and x is a fraction approximately equal to unity,

$$\begin{aligned} V &= (xa_0)^3 \\ dV &= 3a_0^3x^2dx \\ \frac{\partial^2 E}{\partial V^2} &= \frac{1}{9a_0^6x^4}\frac{\partial^2 E}{\partial x^2} \end{aligned} \tag{IV.20}$$

so that

$$B = \frac{x^2}{9V}\frac{\partial^2 E}{\partial x^2}. \tag{IV.21}$$

The quadratic gives the bulk modulus as 0.5762 eV Å^{-3} or 92.3 GPa and the cubic a bulk modulus of 91.9 GPa. These results compare favourably with the experimental result of 97.8 GPa [2].

In summary, some fairly simple calculations have reproduced silicon's lattice constant to within $\frac{3}{4}$% of the experimental value, and its bulk modulus to within 6%.

Testing symmetrisation

As a test of the symmetry code, the eight atom silicon cell was run with the full eight points of the $2 \times 2 \times 2$ k-point mesh, and with the single point produced after symmetrisation. The

% Experimental lattice constant	Energy (eV)
97.5	-1243.2921
98	-1243.3606
98.5	-1243.4045
99	-1243.4124
99.5	-1243.3861
100	-1243.3353

Table IV.3: Energies of bulk carbon as a function of lattice constant.

resultant energy was the same to all figures returned by CASTEP (0.1 μeV).

The lattice constant & bulk modulus of diamond

In a similar fashion the carbon pseudopotential was tested, except that now a higher cut-off of 600 eV was used. A table of results is given in table IV.3. Fitting a quadratic to these data yields an equilibrium lattice constant of 98.89% of the experimental value of 3.56685 Å [2], and a bulk modulus of 481 GPa compared with the experimental values of 442 GPa to 542 GPa [2, 90]. Once more, the agreement is good.

IV.5.2 Bulk calculations on SiC

The above bulk calculations on silicon and carbon are useful tests of the two pseudopotentials, but not particularly stringent ones. It is certain that any silicon pseudopotential is tested on silicon before being distributed, and probably as part of the initial testing procedure. A test on silicon carbide would represent a genuinely new system for the potentials, which, if they are decently transferable, they should pass.

The cut-off for any system must be the highest of the cut-offs required by the pseudopotentials present, so without further discussion the energies for cubic SiC are presented as a function of lattice parameter in table IV.4. These calculations again used an eight atom cubic cell, a $4 \times 4 \times 4$ Monkhorst Pack k-point mesh, and a 600 eV cut-off.

Fitting a quadratic to these data yields an equilibrium lattice constant of 101.4% of the experimental value of 4.3596Å, and a bulk modulus of 225 GPa.

These results for silicon, carbon and silicon carbide are summarised in table IV.5. There is a considerable range of experimental data for the bulk moduli, and the ranges given are those which encompass the data of Landolt and Bornstein [2], Kaye and Laby [90] and for SiC's bulk modulus Yean and Riter [91] and Schreiber and Soga [92]. Data on silicon carbide itself are

Fraction of experimental lattice constant	Energy (eV)
100%	-1053.0647
100.5%	-1053.1257
101%	-1053.1555
101.5%	-1053.1616
102%	-1053.1398
102.5%	-1053.0992

Table IV.4: Energies of bulk silicon carbide as a function of lattice constant.

System	Lattice constant (Å)		Bulk modulus (10^{11}Pa)	
	expt.	calc.	expt.	calc.
Silicon	5.429	5.466	0.98–1.00	0.92
Carbon	3.566	3.527	4.42–5.42	4.81
SiC	4.360	4.421	0.97–2.30	2.25

Table IV.5: Summary of lattice constant and bulk modulus calculations

particularly variable, partly because the material of engineering interest is a compact of small crystals sintered with excess silicon, and will inevitably be considerably softer than a pure single crystal. The value of the bulk modulus of the pure crystal would be almost irrelevant to the engineering profession where the impure compacts are used, and also to the electronics profession where the bulk modulus is simply not an important property. A discussion of the various experimental data and the effects of sample porosity on the bulk modulus is given by Lambrecht *et al.* [93] who conclude that 225 GPa is the best experimental estimation of the bulk modulus. Such a value, lying roughly mid-way between that of silicon and carbon, is very reasonable. Previous values from *ab initio* calculations are 250 GPa and 222 GPa given by Churcher *et al.* [68] in 1988 and Käckell *et al.* [47] in 1994 respectively.

A more careful determination of the bulk modulus from electronic structure calculations would be possible: more points could be taken, more care taken over the function fitted so as to take account of the asymmetry of the minimum, and a correction for the change in energy cut-off between the different cell sizes used. The importance of using the same cut-off when comparing energies from different calculations has already been stressed, but if the unit cells are different this is impossible. The actual cut-off used is always slightly below that requested of the code, for if a 160 eV cut-off is requested, it may be that there are no plane waves states between 159 eV and 161 eV, and hence 159 eV is the true cut-off used. On changing the unit cell, both the number of states and the energy of the highest state within the cut-off will change. Francis and Payne [94] describe a correction for this, which was not applied here as it would have made no difference at the level of accuracy of these calculations.

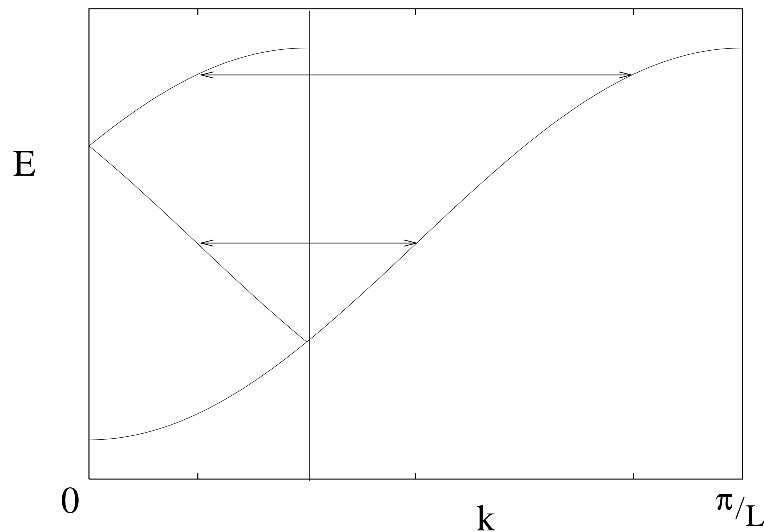

Figure IV.5: A band showing a three-fold folding out of k-space between a unit cell and a supercell three times its size.

IV.5.3 Polytype energy differences: choice of parameters

The importance of using identical FFT grids and k-point meshes in order that errors cancel as much as possible has already been stressed. It might seem that in order to compare the polytypes 2H, 3C, 4H and 6H a cell of 12 layers would have to be used for all of them, as such a cell would be the smallest that could contain an integer number of unit cells of all these polytypes. Although such a cell is conceptually useful, no calculations need be done in it, as calculations in the smaller cells can be made identical to calculations in the large cell.

Suppose one wished to do a calculation with a $25 \times 25 \times 240$ FFT grid and using one layer of k-points in the c^* direction at $c^* = \frac{1}{2}$ in the 12 layer supercell. Reducing this down to the three layer cubic cell an FFT grid of $25 \times 25 \times 60$ has points at identical positions in real space, and four layers of k-points at $c^* = \frac{1}{8}$, $\frac{3}{8}$, $\frac{5}{8}$ and $\frac{7}{8}$ are also equivalent. This idea of "folding out" k-points from a large real-space cell (and thus small in reciprocal space) is illustrated in figure IV.5 for a three-fold folding out.

The full width of figure IV.5 shows an idealised cosine band stretching across a unit cell, with possible sampling points marked on the horizontal axis at $\frac{1}{6}$, $\frac{1}{2}$ and $\frac{5}{6}$. On moving to a supercell of three times the length in real space, the reciprocal space length must be reduced by a factor of three. Also, because the real space cell will now contain three times as many electrons, there should be three times as many bands in the new band structure. This is achieved by simply folding the original band back and forth into the new reciprocal space cell as shown in the left-hand third of the figure. Because the choice of cell does not correspond to the periodicity of the potential, there is no band gap where there would have been no change

Cut-off eV	Wurtzite eV/pair	Cubic eV/pair	Difference meV/pair
400	-262.412	-262.417	5.363
450	-262.835	-262.842	6.533
500	-263.074	-263.080	5.932
550	-263.195	-263.201	6.150
600	-263.259	-263.265	6.008
650	-263.290	-263.296	6.003
700	-263.302	-263.308	5.997
750	-263.307	-263.313	6.010

Table IV.6: Convergence of total energy and energy differences between SiC polytypes as a function of basis set cut-off.

of band in the original unit cell. In the co-ordinates of the supercell, a single point at $\frac{1}{2}$ on the horizontal axis samples the band structure at *exactly* the same places as the set of three points did in the original cell.

Thus the cells chosen do not reflect the smallest unit cells for the individual crystal structures, nor the units cells which have the symmetry of the individual structures, but rather are fractions of one "super–cell' in which all the structures may be described. This method is common to the previous determinations of the energy differences between polytypes.

IV.5.4 Polytype energy differences: convergence and results

Firstly results of the variation of total energy with respect to energy cut-off are shown in table IV.6 and figure IV.6, expressed in terms of energies per pair of atoms, that is, per SiC unit. For these calculations a fine FFT grid of $32 \times 32 \times 288$ in the full 12 layer cell was used. This enabled the same FFT mesh to be used for all the calculations, although once the energy cut-off was fixed at 600 eV it was reduced to $25 \times 25 \times 240$. It can be seen that the energy differences are converged to within 0.1 meV/pair when the absolute energy is still at least 50 meV/pair away from convergence. This table justifies the use of a 600 eV cut-off for the bulk polytype calculations, and a 560 eV cut-off for the surface calculations. In both cases the expected total accuracy is around 0.5 meV/pair, so that the errors due to the finite cut-off are much smaller than this.

Next results regarding k-point sampling are presented. In order to be able to compare all the main polytypes with the same mesh, the sampling in the c^* direction is already relatively dense, leaving a free choice of mesh in the (0001) plane. Various Monkhorst Pack meshes are shown in table IV.7, in which the number of k-points per layer after symmetrisation and the failure stars (see section IV.2.5) are also tabulated. The number of k-points per layer

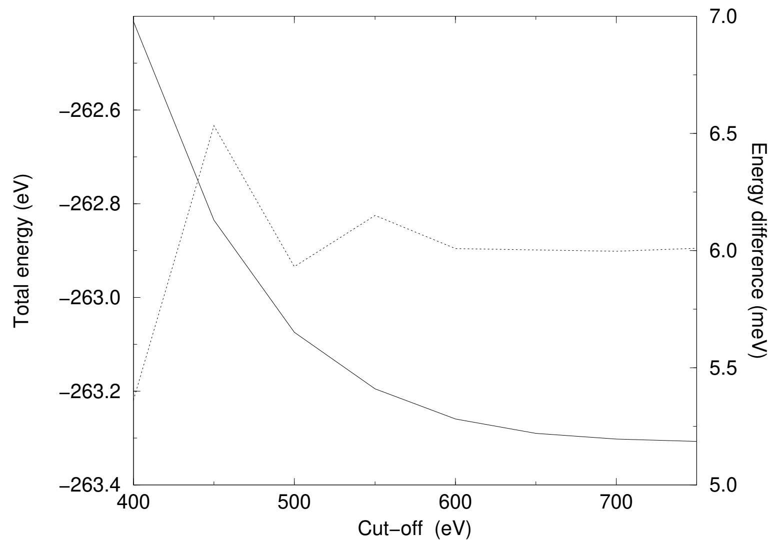

Figure IV.6: Convergence of total energy and energy differences as a function of cut-off. The solid line shows the total energy, and follows the left-hand scale, and the dotted line the 3C/2H difference, and follows the right-hand scale.

after symmetrisation is calculated for the cubic system, which has fewer of the hexagonal symmetry operations than the other structures. The degree of convergence in this table is not as impressive as that in the table of energy cut-offs, and nor is the error cancellation in the energy differences. However, the table does still show the absolute energy varying by 70 meV and the energy differences varying by less than 5 meV over the same range. On the basis of this table the 7×7 mesh was chosen for all other calculations. The very slight discrepency of 0.02 meV/pair between this table and table IV.6 is due to the change in FFT grid between them.

Mesh	Points after reduction	First failure star (Å)	Energy (2H) (eV/pair)	2H – 3C (meV/pair)
4x4	6	12.33	-263.1905	10.13
5x5	8	15.41	-263.2409	6.89
6x6	11	18.50	-263.2547	6.23
7x7	13	21.58	-263.2589	5.99
8x8	17	24.66	-263.2603	5.64
10x10	24	30.20	-263.2608	5.86

Table IV.7: Convergence of total energy and energy differences between SiC polytypes as a function of k-point sampling. The second column gives the number of k-points per layer in the 3C system after symmetrisation.

% Experimental lattice parameter	Wurtzite – Cubic (meV/pair)
100	6.01
101	6.10
102	6.23

Table IV.8: Convergence of total energy and energy differences between SiC polytypes as a function lattice parameter.

Polytype	Energy (eV/pair)	Difference (meV/pair)	Result of Cheng (meV/pair)
2H	–263.25890	5.99	8.70
3C	–263.26489	0.00	0.00
4H	–263.26731	–2.42	–0.78
6H	–263.26713	–2.24	–1.19

Table IV.9: Energy differences between SiC polytypes.

There remains one other parameter to check in these calculations: that of the lattice constant used. One could pick the experimental value, or the value given by these LDA calculations, and one could pick the value for 3C or for some other polytype. The obvious question is: does it matter? Thus in table IV.8 are presented the 3C / 2H energy differences at three different lattice constants. The differences do vary, as would be expected from the different equilibrium lattice constants of the structures, but not significantly.

Having now chosen a cut-off and k-point mesh, it remains to recalculate the polytype energy differences as previously done by Cheng *et al.* [50]. These are shown in table IV.9, together with Cheng's results for the energy differences. The results of Cheng *et al.* were achieved with a cut-off of just 435 eV and a 9x9 mesh of k-points in the (0001) plane. Although they did check their results carefully for convergence with both cut-off and k-point sampling, the cut-off used is surprisingly low. A lack of computing power prevented the use of a higher cut-off, and comparison with yet lower cut-offs suggested convergence, but considering the oscillatory nature of the variation of the energy difference with cut-off shown by table IV.6 this may have been a chance result. The pseudopotentials used in 1988 are likely to be less sophisticated than current pseudopotentials, making the low cut-off seem even more unlikely.

The new results show broad agreement with those of Cheng *et al.*, although Käckell *et al.* [47] have also done similar calculations with rather different results, including a 15 meV/pair difference between the cubic and wurtzite (2H) structures. Such results are clearly not repeated here over the wide range of cut-offs and k-point meshes chosen, and the reason for the dramatic difference remains unclear.

	Unrelaxed			Relaxed	
	Cheng	Käckell	This work	Cheng	Käckell
J_1	4.85	7.85	3.47	4.81	1.25
J_2	–2.56	–1.60	–2.71	–2.90	–2.35
J_3	–0.50	–0.25	–0.47	–0.46	–0.47

Table IV.10: Electronic contribution to J_n. Units are meV/pair.

IV.6 Analysis

IV.6.1 J_n's

Taking these results together with those of Cheng *et al.* and Käckell *et al.*, there are now three calculations of the unrelaxed polytypes energy differences and two of the relaxed energy difference. From each of these values for J_1, J_2 and J_3 can be determined, assuming that

$$E = J_0 N - \sum_{\substack{n=1,3 \\ i=1,\infty}} J_n \sigma_i \sigma_{i+n} \tag{IV.22}$$

(see section II.5.1). The relevant formulae are given by Cheng *et al.* and are repeated in appendix D, and the resulting table is shown as table IV.10.

The reduction in $|J_n|$ as n increases is common to all the data, and is to be expected as electronic interactions are usually short-ranged. The various sources also agree unanimously on the signs of the J_n's. This table will be referred to again at the start of the next chapter.

The applicability of the above analysis can be tested by attempting to predict the energy of the (rare) 8H polytype. In terms of J_n's its energy with respect to 3C is

$$\begin{aligned} E_{8H} - E_{3C} &= \frac{1}{2}J_1 + J_2 + \frac{3}{2}J_3 + 2J_4 \\ &= -1.68 \text{ meV} \end{aligned} \tag{IV.23}$$

with J_4 assumed to be zero (see appendix D).

This is now tested by calculating the energies of 3C, 4H, 6H and 8H in the same supercell. This is the first time, to the author's knowledge, that any electronic structure calculation has been done which enables J_4 to be calculated. The calculation uses a supercell of 24 layers (24 being the lowest common multiple of 8 and 3), with an 8×8 Monkhorst–Pack k-point mesh perpendicular to the stacking direction, a 600 eV cut-off and a $24 \times 24 \times 480$ FFT grid in the supercell. The results are shown in table IV.11. Not only are the 4H and 6H results in remarkable agreement with those in table IV.9 despite the change in k-point sampling, but the energy of the 8H polytype is just 0.1 meV away from the prediction of this simple

Polytype	Energy (eV/pair)	Difference (meV/pair)
3C	–263.26624	0.00
4H	–263.26866	–2.42
6H	–263.26847	–2.23
8H	–263.26802	–1.78

Table IV.11: Energy differences between SiC polytypes including 8H in a 24 layer supercell.

formula. To suggest that the error is solely due the the omission of the J_4 term would be to take a rather cavalier attitude to other possible sources of error, but the result does usefully suggest that $|J_4|$ is probably less than 0.1 meV, so continuing the trend of rapid decrease in the value of J_n. It must, of course, be repeated that this result is only valid in the absence of relaxation effects.

IV.6.2 Relaxation

The obvious question arising from this work is "why not calculate the energy of the fully relaxed structures?" To do so merely to confirm the 2H – 3C – 4H/6H ordering found by Cheng *et al.* and Käckell *et al.* would seem to be a fairly pointless diversion. The real prize would be to resolve the 4H – 6H energy difference.

This difference is expected to be around 0.1–0.2 meV/pair, so an accuracy of 0.05 meV/pair would be required. There are now listed briefly some of the issues involved in such a calculation which would need to be addressed.

a) CASTEP's ionic relaxation routine, discussed more fully in section V.4.3, converges rapidly to positions close to the minimum, but suffers from worse and worse undershoot the closer to the minimum it gets. Relaxing down to the 20 μeV/atom level required would take a lot of CPU time. The alternative would be to rewrite the relaxation routine.

b) CASTEP has no means to relax the unit cell parameters a and c, which are independent for 4H and 6H. The most simplistic way of finding the minimum would be to calculate the energy at various different, fixed values of a and c, and to fit a quadratic surface to the resulting data. As there are six fitting parameters, an absolute minimum of six full calculations would be required. This is essentially the technique used by Käckell *et al.*, who fitted a cubic surface to "typically 48" data points for each of the hexagonal polytypes. A smaller number of points would surely have sufficed had they used the Francis–Payne correction (described in section IV.5.2) to eliminate the noise caused by

changes in the basis set as the cell size was varied. A more sophisticated approach would use the Hellmann–Feynman stresses on the cell, corrected for the Pulay stress [95] caused by the dependence of the basis set on the cell parameters, in a manual or automatic search for the energy minimum.

c) The accuracy of the whole LDA method at this sort of level is questionable. To resolve possible concerns about this, comparisons with alternative approximations for the exchange-correlation energy, such as GGA, would have to be made.

The more modest aims of this chapter were to introduce the CASTEP code, and to show it in use in calculating simple bulk properties of silicon, carbon and silicon carbide, as well as to demonstrate the evaluation of structural energy differences. These aims have been achieved.

Chapter V

Ab Initio Calculations on Surface Orientation

This chapter extends the electronic structure calculations of the previous chapter to consider the energy of a stacking boundary at a free surface. In order to attain this goal, a careful consideration of the details of surface calculations with periodic boundary conditions is made, and a correction for the interaction between a surface and its periodic image introduced into the CASTEP code.

V.1 Polytypic growth from surface energies

The surface calculations on SiC form the major part of this work. The idea is to model the growth of a crystal in a simple way which includes more of the physics of growth than a bulk calculation, and yet stops short of a full simulation of the dynamics of growth from the vapour which is a process which will probably remain beyond the scope of computers for many years yet.

A simple model of crystal growth is therefore proposed. That is that growth proceeds by the addition of complete layers on the surface of a crystal, the layer choosing the lowest orientational energy. Thus considering for simplicity a cubic substrate, the question is asked as to whether '$\ldots\ ++++$' is favoured over '$\ldots\ +++-$'. These sequences are now only semi-infinite, so direct application of previous theory may not be applicable, but it is easy to write down the energy difference in terms of the layer interaction model of section II.5.1 as

$$\Delta E = -2\sum_{n=1}^{\infty} J_n \tag{V.1}$$

As the sum of the first three J_n's is positive in four of the five cases given in table IV.10 from section IV.6.1 (page 72), ΔE will be negative and the cubic form will be favoured. The contribution from the phonons to J_n described in section III.5.2 favours the cubic form even more clearly as all the individual J_n's are positive. Thus this layer by layer model for growth will, in this simple analysis, result in the cubic form growing, even though this is not the lowest energy form for the bulk structure.

Such analysis, applying J_n's calculated in bulk structures directly to surfaces, was done by Heine *et al.* [23], and has subsequently been used by Chien *et al.* [57]. It has two deficiencies which this chapter seeks to resolve: it takes no account of the effect of the surface on the J_n's, and it cannot distinguish between the two types of SiC surface — that covered by silicon and that covered by carbon. By performing electronic structure calculations for the surfaces themselves, with different orientations of the surface layer, both of these points are addressed.

It is necessary to spend a moment considering the advantages and deficiencies of this model. Firstly, growth is clearly an atom–by–atom process, not a layer–by–layer process, so the idea of adding layers seems strange. However, whilst atoms are on a growing surface, they are relatively free to move, and thus the newly grown layer can also move readily to its lowest energy position. Once a layer is buried in the bulk of the crystal, re-arrangement is much harder, and whatever structure it gained whilst on the surface can be considered to be "frozen–in" to the crystal, only changing after long annealing.

Thus this model does permit a crystal to grow in a non-equilibrium phase. Moreover, by retaining the short–range periodicity of the crystal in two dimensions, it is relatively easy to simulate.

There are, however, deficiencies. Dislocations and surface steps are absent from this model, and can be important in polytype formation, as has been discussed in section II.2 *et seq.*

In using this model, it is necessary to consider the two types of SiC surface. SiC, when cut perpendicular to the stacking direction for the polytypes, has two types of surface, as is shown in figure V.1. One is terminated by silicon, the other by carbon. There is no reason why growth in this model should proceed in the same way on both surfaces, so each will be considered separately.

These calculations will consider the difference in energy between a surface layer oriented with and against the stacking direction of a cubic substrate. The effect of the relaxation of the surface layers perpendicular to the surface will also be considered. As always, energy differences between structures, rather than absolute energies, are being measured. Figure V.2 shows schematically these two possible orientations at a (0001) surface.

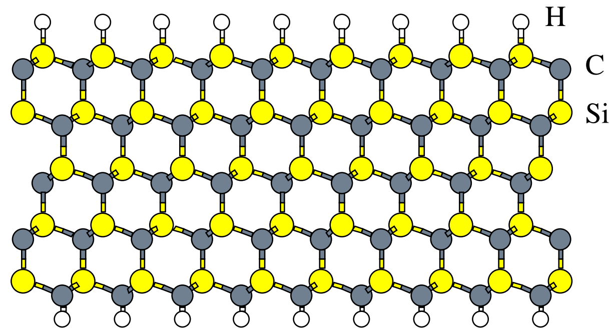

Figure V.1: A SiC slab showing two types of surface — at the top the (0001) surface with silicon at the surface, at the bottom the $(000\bar{1})$ surface with carbon. Hydrogen is shown saturating the "dangling bonds" at the surface, as is discussed in section V.2.2

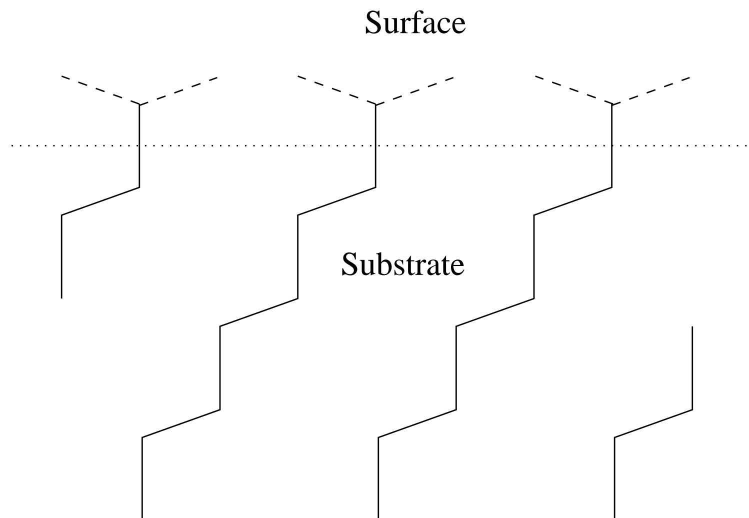

Figure V.2: A (0001) surface on a 3C substrate, with the two possible orientations of the surface layer shown. The leftward orientation describes a stacking reversal.

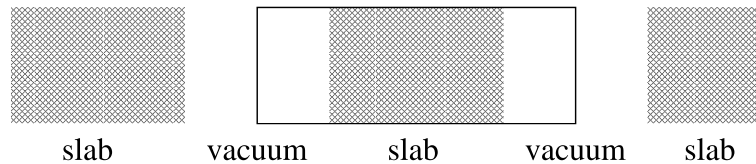

Figure V.3: The sandwich structure used to model surfaces. A unit cell is outlined.

V.2 CASTEP and surfaces

V.2.1 The sandwich cell

So far CASTEP and the plane wave method has been discussed in relation to periodic crystals only. Once a surface is formed, periodicity in that direction is broken, and much of the preceding analysis becomes invalid. In order to regain periodicity, the idea of a "sandwich cell" is used.

Rather than considering just one, isolated slab of SiC, an infinite sandwich is constructed of SiC slabs followed by vacuum gaps. If the vacuum region is sufficiently wide, the neighbouring slabs will not interact significantly, and an isolated slab will be accurately simulated. Similarly, if the slab is sufficiently thick, its two surfaces will not interact, and an isolated surface is thus simulated. Figure V.3 shows this construction.

"Sufficiently thick" is difficult to determine *a priori*, although calculations at different thicknesses can readily determine whether any interaction across the vacuum or through the slab remains. In practice, distances of just 10 Å are usually sufficient, and there follows a brief explanation of why such small distances should suffice.

Away from the attractive potential of an atomic core, electronic wavefunctions should decay exponentially, with a characteristic decay length of less than 1 Å. As the charge density is simply proportional to the square of the amplitude of the electronic wave function, this too decays exponentially into the vacuum region. Thus for a fairly small separation between the two slabs the centre of the vacuum will attain a very small charge density, small enough to ignore.

There remains the possibility that the electrostatic potential due to one surface could affect another surface across the vacuum gap. Ignoring the small effect of the electronic charge in the vacuum, the potential must obey

$$\nabla^2\phi = 0. \tag{V.2}$$

At the surface, ϕ must vary in the plane of the surface as the various surface atoms are traversed. It is reasonable to wonder whether this variation of ϕ is still noticeable across a

region of vacuum. Considering just the lowest frequency fourier component of ϕ, and writing

$$\phi = a \exp i(k_x x + k_y y + k_z z) \tag{V.3}$$

one can then substitute this into equation (V.2) to produce

$$-k_x^2 - k_y^2 - k_z^2 = 0. \tag{V.4}$$

This implies that k_z is imaginary as k_x and k_y must be real. In other words, the oscillations in ϕ occurring parallel to the surface decay exponentially away from the surface in a vacuum. Further more, the decay length is equal to the wavelength of the oscillations, which cannot be greater than the unit cell axis length of 3.1Å. If one were to include a consideration of the electrons as well, these would screen the variations in the potential producing an even faster decay.

There is just one outstanding problem. A potential of the form $\phi = az$ solves V.2, and produces a long–ranged interaction. This problem is discussed in section V.3.

The potential arising from a slab in a unit cell is shown in figure V.4. The "slab" in this figure consists, rather artificially, of a plane of potassium atoms and a plane of chlorine atoms, separated by 2.7 Å. At the top of the diagram, which shows the potential in a slice through such a cell, a slice which cuts through the nuclei, is a line of chlorine atoms, with a line of potassium atoms directly below them. Then there is a region of vacuum of just over 9 Å. In this region it can be seen that the equipotential lines rapidly straighten and move to equal spacing, representing a uniform electric field. The bottom of the figure shows the periodic image of the slab again. The details of this plot will be referred to again.

V.2.2 Termination or reconstruction?

Surfaces are highly reactive areas. From the point of view of a chemist they contain dangling bonds. These bonds will try to satisfy their bonding requirements in one of two ways. Either they will grab some passing molecule from any vapour phase above them and use it to saturate the bond, or they will perform some sort of surface rearrangement which places pairs of surface atoms closer together, and which point the dangling bonds can bend towards each other and join.

Surface rearrangement is common, but it can be complex. Silicon has famously been shown to undergo a surface reconstruction in which the unit cell of the reconstructed surface contains 7x7 unit cells of the unreconstructed surface by both experimental [96] and *ab initio* methods [97]. Even the simplest reconstruction must lead to a new cell which is 2x1 times

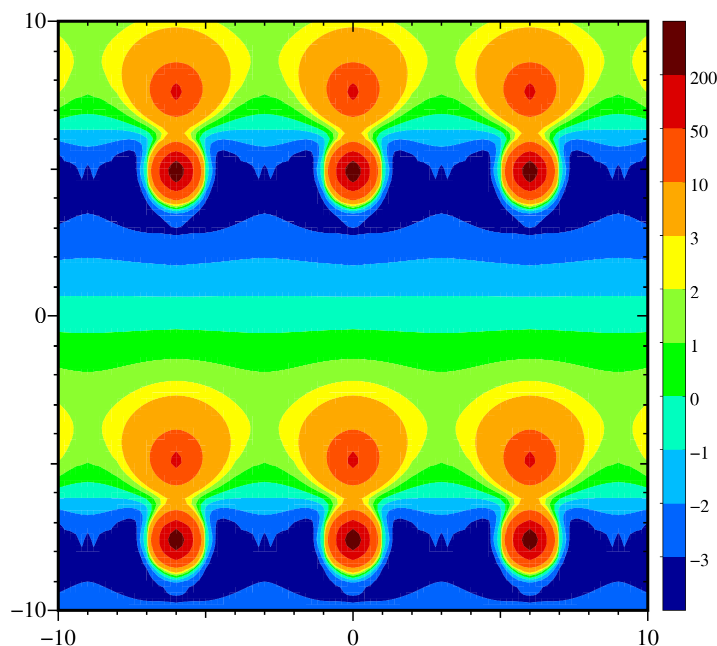

Figure V.4: The potential in volts arising from a slab placed in a periodic sandwich. The axis scale is Angstroms, and the atoms are potassium (top row), chlorine (second row). The unit cell is 12.5 Å tall and 6 Å wide, so it is seen repeated here.

the size of the old. Figure V.5 shows such a reconstruction, in which the rows of atoms have moved alternately left and right in order to give each surface atom one close neighbour to which it may bond.

Reconstructions have been observed on the (0001) face of 3C and 6H silicon carbide [98]. The reconstruction changed as a layer grew, returning to the initial state once the layer was complete. The same reconstructions were observed for both the 3C and 6H polytypes, and included a $\sqrt{3} \times \sqrt{3}$ and a 3×3 reconstruction.

From a computational point of view, reconstruction is expensive. A doubling of the unit cell size quadruples the required memory, and the extra size is coupled with a loss of symmetry, so the time taken for a run would increase by much more than a factor of eight, probably at least a factor of twelve, for just the electronic relaxation. Relaxation of the ions is also much more complicated, as each atom is free to move in the plane of the surface, as well as relax into it.

For these reasons, it was decided to terminate the dangling bonds with hydrogen. Hydrogen will be present when SiC is grown from silane / hydrocarbon mixtures, and it is really the only sensible choice for a terminating atom. A monovalent atom which will form a reasonably

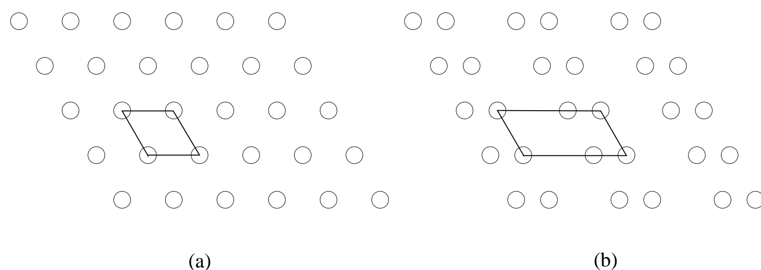

Figure V.5: A surface before (a), and after (b), a simple 2×1 reconstruction. A unit cell is outlined in each case.

non-polar covalent bond with silicon or carbon is required, for a strongly polar bond could cause spurious affects by polarising the surface. The alkali metals are not good at forming covalent bonds, and the halogens are either too electronegative or too large. The halogens have the added disadvantage of introducing seven electrons to the system to hydrogen's one electron.

It is acknowledged that adding a monolayer of hydrogen in this fashion might affect the surface energy differences sought. It has recently been shown [99] that a monolayer of H on Si(111) not only prevents the above 7×7 reconstruction, but also causes growth to proceed by faceting, rather than by monolayers. Accepting this risk is a compromise which must be made in order to simplify the problem to be studied.

V.3 Technical development of calculation with dipole moment

V.3.1 Dipole–dipole interaction

As mentioned above, it is necessary to ensure that the vacuum region between two slabs is sufficiently wide to eliminate any noticeable interaction between them, and whereas most interactions decay exponentially away from the slab, a net dipole moment in the unit cell produces an interaction which will be shown to decay as the reciprocal of the cell length.

CASTEP considers not only the atomic positions and electronic wavefunctions within the system to be periodic, but also the potential. The latter does not follow from the former if the unit cell has a dipole moment, as a dipole usually causes a step change in the potential.

Care must be taken when discussing dipole moments of cells in periodic systems. Whereas the dipole moment of a molecule is well–defined, irrespective of the origin used to calculate it, the same is not true of the dipole moment of a unit cell in a periodic system. As shown

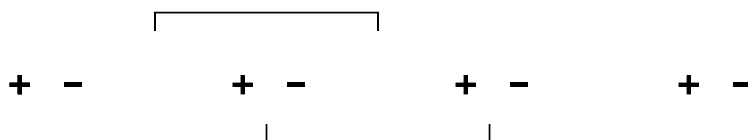

Figure V.6: The dipole moment per unit cell in a periodic system. Two different unit cells are outlined above, which clearly have very different dipole moments, showing that the dipole moment is dependent on the choice of unit cell.

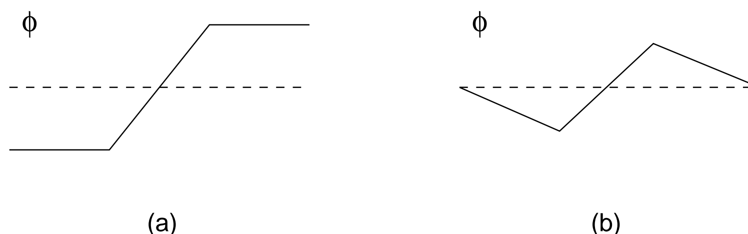

Figure V.7: Potentials across a dipole slab. In (a) is shown the variation of potential, ϕ, across a dipole. In (b) is shown the way in which CASTEP would force this potential to be periodic.

by figure V.6, not even the sign can be determined until the cell is precisely defined. Or to state this in a slightly different way, the dipole moment per unit volume in an infinite crystal is determined by the boundary conditions at infinity. It is therefore necessary to decide what boundary conditions are required, and compare these to those that CASTEP is using.

For the study of an isolated slab, the natural boundary condition would be that the electric field in the vacuum should be zero. The step in potential from one side of the slab to the other caused by the slab's dipole moment would give a non-periodic potential in this case. CASTEP re-introduces periodicity into the potential by adding a constant field across the cell, the magnitude of which is dependent on the cell's size and dipole moment. This is shown in figure V.7. Although this field does tend to zero as the vacuum size is increased, it does so slowly, decreasing as the reciprocal of the cell length.

V.3.2 Corrections for the dipole–dipole interaction

There are three possible approaches to the problem of this slowly–decaying interaction. It could be eliminated by a careful choice of cell for which the dipole moment is zero, it could be corrected by a *post hoc* correction term added on to CASTEP's final energy, or it could be eliminated in a self–consistent way inside CASTEP. These approaches are now discussed. It should be remembered that provided the unit cell retains its three-fold rotation axis perpendicular to the surface, then the dipole moment is constrained to lie along that axis. This simplifies the analysis, and allows the use of a single scalar to describe the dipole moment.

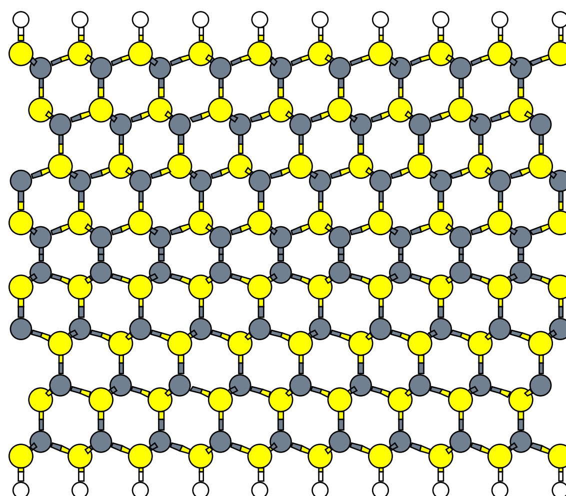

Figure V.8: A SiC slab with inversion symmetry, obtained by introducing a C–C bond in the centre of the slab. Both surfaces are thus silicon covered.

Elimination of dipole moment

Elimination of the dipole moment can be achieved by ensuring that the unit cell has inversion symmetry. This is difficult to achieve in SiC, for one surface has Si on it, the other C. It is soluble by placing a carbon–carbon or silicon–silicon bond in the centre of the slab, as shown in figure V.8. Then both top and bottom surfaces are the identical, and the orientation of both surfaces would have to be changed together in any comparison in order to keep the inversion symmetry. This has the advantage of doubling the energy difference between the structures compared.

This scheme does have one major disadvantage. In order to avoid the carbon–carbon or silicon-silicon bond affecting the surface, the slab would need to be eight layers thick, or possibly ten. A similar degree of isolation of a single surface would be achievable with about half the number of layers if the requirement for inversion symmetry could be avoided. As the time required to perform a calculation scales as the square (at least) of the number of atoms present, the eight layer structure shown in figure V.8 would take over two and a half times the CPU time of the five layer structure of figure V.1.

***Post hoc* correction**

The next simplest scheme is to calculate the energy of the dipole–dipole interaction from classical electrostatics, and correct for this in a *post hoc* fashion. The calculation of the *post hoc* correction proceeds as follows, in which it is assumed that the dipole moment lies along the z axis, and is therefore expressed as a scalar.

The dipole moment p of the total charge distribution in the cell gives rise to a step in the potential. This is most simply evaluated by considering the well–known parallel plate capacitor. A capacitor of plate separation d and surface charge density σ has a dipole moment per unit area of σd, and a field between the plates of σ/ϵ_0 giving rise to a potential difference of $\phi = \sigma/\epsilon_0$. So, for a cell of dipole moment p,

$$\phi = \frac{p}{\epsilon_0 A} \tag{V.5}$$

where A is the area of the cell perpendicular to p. In order to eliminate this step in potential by the introduction of a uniform electric field across the cell, the field must have magnitude

$$\mathcal{E}_z = \frac{p}{\epsilon_0 A z} = \frac{p}{\epsilon_0 V} \tag{V.6}$$

where z is the extent of the cell perpendicular to A, and V is the volume of the cell.

This leads to two terms in the electrostatic energy, the self energy of the field, and the interaction of the field with the dipole. The first of these is the integral of $\frac{1}{2}\epsilon_0\mathcal{E}^2$ throughout the cell, where as a first approximation the cell is assumed to be predominantly vacuum, and is an energy cost which will raise the calculated energy. The second is the interaction of the dipole moment p with the field, and lowers the calculated energy by an amount $p\mathcal{E}$. The total energy contribution is then

$$E = -\frac{p^2}{2\epsilon_0 V}. \tag{V.7}$$

Thus the total energy has been lowered by the dipole–dipole interaction, and the above term should be subtracted from the final energy in order to correct for this.

This does retain one disadvantage – the electrons still see and respond to the extraneous electric field. Thus the correction is not complete, and some variation of the corrected energy with cell size would still be expected.

This correction is discussed in more detail and in a more sophisticated form in appendix B which required knowledge of the slab's dielectric constant.

Self consistent correction

The above *post hoc* adjustment to the total energy should be included within the expression which CASTEP minimises. This can be done in the following way. Firstly it is necessary to consider the dipole moment as arising from two parts — one due to the electrons, and one due to the ions. Using subscripts of e and I to refer to the electronic and ionic contributions, equation (V.7) can be written as follows

$$\begin{aligned} E &= \frac{(p_I + p_e)^2}{2\epsilon_0 V} \\ &= \frac{p_I^2}{2\epsilon_0 V} + \frac{p_I}{\epsilon_0 V}\int \rho(z) z dz + \frac{1}{2\epsilon_0 V}\int\int \rho(z')z'dz'\rho(z)zdz \end{aligned} \tag{V.8}$$

where

$$\rho(z) = \int\int \rho(\mathbf{r}) dx\, dy \tag{V.9}$$

and remembering that the contributions to the dipole moment are all constrained to lie along z. The Kohn-Sham potential is produced by taking the functional derivative of the energy with respect to $\rho(\mathbf{r})$, and this produces

$$\begin{aligned} V(z) &= \frac{p_I}{\epsilon_0 V} z + 2\frac{1}{2\epsilon_0 V}\int \rho(z')z'dz'z \\ &= \frac{p_I + p_e}{\epsilon_0 V} z \\ &= \frac{p}{\epsilon_0 V} z \end{aligned} \tag{V.10}$$

Thus the term to be added to the Kohn-Sham potential is precisely the electric field found in equation (V.6). This addition will have the correct sign to cancel the field, and thus leave a zero field in the vacuum, but a step at some arbitrary point in order to keep the potential periodic, as the potential derived is linear. This step is introduced in the centre of the vacuum, away from any charge density, where it can do no harm.

The Kohn-Sham potential may now be correct, but what of the energy? Assuming that this potential is made to act on the ions as well, the energy will have changed by an amount equal to

$$\begin{aligned} \Delta E &= \int V(\mathbf{r})\rho(\mathbf{r})d\mathbf{r} + \sum_I V(\mathbf{R}_I)q_I \\ &= \frac{p}{\epsilon_0 V}\int \mathbf{r}\rho(\mathbf{r})d\mathbf{r} + \frac{p}{\epsilon_0 V}\sum_I \mathbf{R}_I q_I \\ &= \frac{p^2}{\epsilon_0 V}. \end{aligned} \tag{V.11}$$

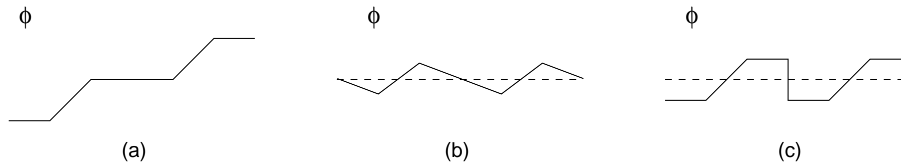

Figure V.9: Potentials across repeating dipole slabs. In (a) is shown the variation of potential, ϕ, across a series of dipoles. In (b) is shown the way in which CASTEP would force this potential to be periodic, and in (c) the result of applying the *post hoc* correction described.

This is precisely twice the desired energy correction of equation (V.7). This is eliminated by the addition of an overcounting term to the electronic energy, and by halving the potential which acts on the ions.

This scheme has eliminated the unwanted electric field described in the previous section, and thus can be expected to give rather better results. Figure V.9 shows the real, physical potential that the periodic sandwich would produce, that which the unaltered CASTEP code would produce, and that produced by this alteration. In the region of the slab, the potential after this correction can be seen to be identical to the physical potential, the only difference arising in the centre of the vacuum where there is nothing on which the resulting potential gradient can act. The elimination of the imposed electric field also means that ϵ_r will not enter into the equations, for ϵ_r merely describes a system's response to such a field.

This discontinuity in the field in the centre of the vacuum can be viewed as being simply an artificial parallel plate capacitor. It has no net charge, has no external field, and has just a step change in the potential across it. Having no external field, it does not interact with anything in its neighbourhood.

In implementing this correction, two decisions were taken. Firstly, CASTEP used to construct the Kohn-Sham potential in no fewer than seven different places in the code. These were replaced by a call to a single subroutine so that adjustments to the potential could be coded more simply.

Secondly, CASTEP stores the charge density on both real space and reciprocal space grids. Either could be used for calculating the dipole moment, and using the reciprocal space grid is faster and more accurate given that the grid is sufficiently dense to store the reciprocal space charge density exactly. However, for ease of coding the real space grid was used. Subsequent tests with a reciprocal space calculation showed no significant improvement in speed or stability of CASTEP as a whole.

This self-consistent correction can also be achieved by recalculating the Ewald summation of the electrostatic energy with a boundary condition other than $V = 0$ at infinity. This was

done by Makov and Payne for the case of a single isolated molecule in the unit cell [100], whereas the simpler technique used here was also developed independently by Neugebauer and Scheffler [101]. The author is grateful to Dr Makov for discussions on this topic, and for his repetition of his results of the above paper for the boundary conditions relevant to the geometry used here. Of course an identical expression resulted.

V.3.3 Results of tests

In order to test and demonstrate the post hoc and self-consistent corrections outlined above, a simple system was studied. Rather than considering an SiC slab with its many atoms and electrons and high energy cut–off, a system consisting of a plane of potassium atoms and a plane of chlorine atoms was considered. Such a system is unphysical only in the sense that it is highly unstable, and could not possibly be produced in a laboratory. From a theoretical point of view, the atoms produce a perfectly reasonable potential, and attempting to find the electronic ground state is likewise perfectly meaningful. As a simple test system it has a strong dipole moment, and can be run much faster than SiC.

The total length of the sandwich cell was varied from 10Å to 60Å, and the way in which the energy converged as a function of cell length investigated for three cases: no correction, post hoc correction and self-consistent correction. The dipole moment of the cell was also recorded to investigate the effect on the charge distribution of the corrections. As the post hoc correction is merely a correction to the energy, the charge distribution and dipole moment are unchanged.

A 160 eV cut-off was used in these calculations, a unit cell with orthogonal axes with the x and y lengths being 6Å, and the distance between the K and Cl nuclei was 2.7Å.

As can be seen from table V.1 and figure V.10, such corrections dramatically increase the convergence with cell size, particularly so in the case of the self-consistent correction. This KCl system was chosen for its large dipole moment per unit volume, and its low cut-off. The required correction for the SiC systems would be expected to be less significant.

The electrostatic potentials produced in this system are also shown in figure V.11 for comparison with figure V.9. It can be seen that the linear term has indeed been eliminated, and leaving the potential in the vacuum almost constant. In figure V.11 the potassium atom is at 4.9Å, and the chlorine atom at 7.6Å. No further change in the electronic configuration was calculated between the two plots shown, but table V.1 shows that the dipole moment of the charge distribution fell by one third when the self-consistent correction was applied. The potential difference across the slab would fall by the same factor. This potential difference is given by equation (V.5), where $A = 36\text{Å}^2$ and $\epsilon_0 = 1/181$ in electrostatic units. So with

z (Å)	Energies (eV)			Dipole Moments (eÅ)	
	uncorrected	ph correction	sc correction	uncorrected	sc correction
10	–414.5186	–413.3352	–413.6056	2.17	1.559
12.5	–414.2750	–413.4788	–413.7298	1.99	1.326
15	–414.1503	–413.5707	–413.7454	1.86	1.274
20	–414.0275	–413.6686	–413.7576	1.69	1.256
25	–413.9569	–413.7027	–413.7547	1.59	1.255
40	–413.8680	–413.7359	–413.7531	1.45	1.255
60	–413.8260	–413.7462	–413.7532	1.38	1.255

Table V.1: The convergence of the energy and dipole moment of a system with respect to cell size after various corrections for dipole–dipole interactions. ph and sc abbreviate *post hoc* and self-consistent respectively.

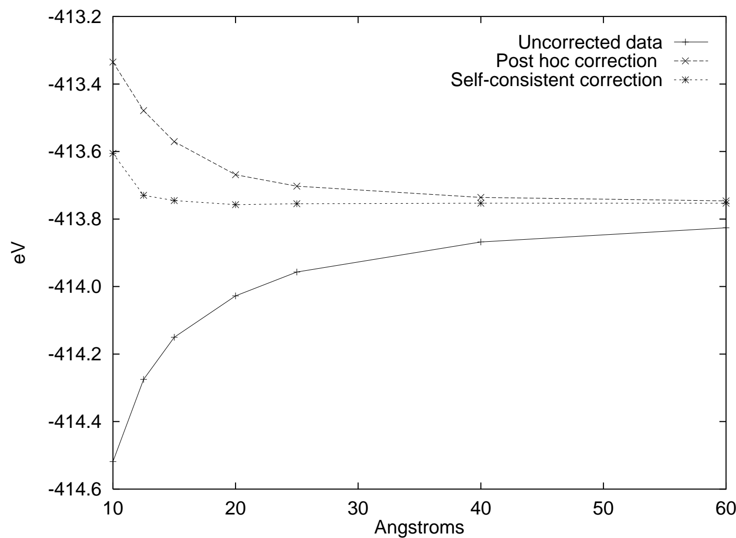

Figure V.10: The data of table V.1 showing the convergence of energy with respect to cell size presented graphically.

$p = 1.99$eÅ from table V.1 for the electrons relaxed in the uncorrected potential, a potential difference of 10.0V is expected. This is indeed found.

The reader is also referred back to figure V.4 on page 80 where the uncorrected potential for this system across the plane through the K and Cl atoms was shown.

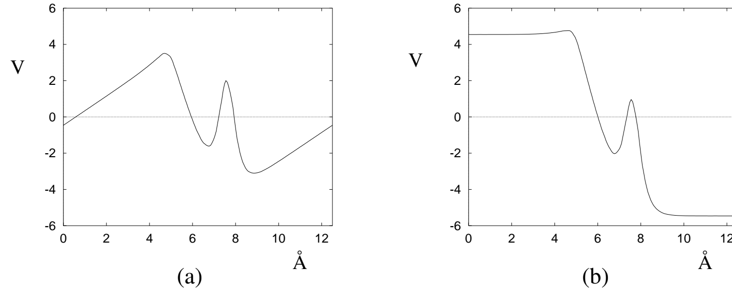

Figure V.11: The averaged potential across a unit cell. (a) before any correction, and (b) immediately after applying the dipole correction.

V.4 Theory, practice & improvements for atomic relaxation

V.4.1 Ionic forces through the Hellmann–Feynman theorem

So far the total energy of the system has been considered. Now, additionally, forces are required. The force $\mathbf{F}_n$ on atom n with position vector $\mathbf{R}_n$ is given by

$$\mathbf{F}_n = \frac{dE}{d\mathbf{R}_n}. \tag{V.12}$$

This simple definition of a force can then be manipulated as follows:

$$\begin{aligned}
\frac{dE}{d\mathbf{R}_n} &= \frac{\partial E}{\partial \mathbf{R}_n} + \sum_i \left[\frac{\partial E}{\partial \psi_i}\frac{\partial \psi_i}{\partial \mathbf{R}_n} + \frac{\partial E}{\partial \psi_i^*}\frac{\partial \psi_i^*}{\partial \mathbf{R}_n} \right] \\
&= \frac{\partial E}{\partial \mathbf{R}_n} + \sum_i \left[\left\langle \psi_i \middle| \hat{H} \middle| \frac{\partial \psi_i}{\partial \mathbf{R}_n} \right\rangle + \left\langle \frac{\partial \psi_i}{\partial \mathbf{R}_n} \middle| \hat{H} \middle| \psi_i \right\rangle \right] \\
&= \frac{\partial E}{\partial \mathbf{R}_n} + \sum_i \left[\left\langle \lambda_i \psi_i \middle| \frac{\partial \psi_i}{\partial \mathbf{R}_n} \right\rangle + \left\langle \frac{\partial \psi_i}{\partial \mathbf{R}_n} \middle| \lambda_i \psi_i \right\rangle \right] \\
&= \frac{\partial E}{\partial \mathbf{R}_n} + \sum_i \lambda_i \frac{\partial}{\partial \mathbf{R}_n} \langle \psi_i \mid \psi_i \rangle \\
&= \frac{\partial E}{\partial \mathbf{R}_n}.
\end{aligned} \tag{V.13}$$

This analysis is true for the ground state only, the important step being the recognition that $\hat{H}|\psi_i >= \lambda_i|\psi_i >$ in the ground state, λ_i being the eigenvalue associated with ψ_i. Thus for the ground state, the force on an ion is given by the change in the value of the Hamiltonian with respect to the ion's co-ordinates, with no corresponding change in the electronic wavefunctions. This means that the force on the ions is simply the classical electrostatic force arising from the charge density of the electrons and ions, as the only term with explicit dependence on $\mathbf{R}_n$ in the Hamiltonian is such a term. This result is known as the Hellmann–Feynman

theorem [102, 103].

If the basis states had not been independent of the atomic co-ordinates, that is, if the basis states had included localised orbitals which moved with the atoms, an additional, non-zero term would have arisen in the full derivative of E with respect to $\mathbf{R}_n$ due to the change in basis set. The resulting 'Pulay force' [95] must also be included when calculating the force on each atom, but due to the choice of a plane wave basis set, this concern does not arise.

One other important result arises from the study of the forces on the atoms. If all the atoms are moved through a small displacement $\delta\mathbf{R}$, then the change in energy resulting is

$$\begin{aligned} \delta E &= \sum_n \mathbf{F}_n . \delta\mathbf{R} \\ &= \delta\mathbf{R} . \sum_n \mathbf{F}_n . \end{aligned} \tag{V.14}$$

This should be zero for any displacement $\delta\mathbf{R}$, as the energy should be independent of the choice of origin. Hence $\sum \mathbf{F}_n$ is zero. Another way of considering this is that as no external force is acting on the system, the sum of all the internal forces must be zero as a consequence of Newton's third law.

V.4.2 $\sum \mathbf{F}_n \neq 0$, and ΔE on rigid shifts

Equation (V.14) clearly shows that

$$\sum_n \mathbf{F}_n = \mathbf{0}. \tag{V.15}$$

The reasons why this might not be exactly true after the approximations made by CASTEP are now discussed.

Firstly, the Hellmann–Feynman theorem is true at the electronic ground state only. If the electronic wavefunctions are not converged, then the forces are simply wrong. The error in the Hellmann–Feynman forces is first order in the error in ψ [84], whereas that in the energy is second order, so the forces converge more slowly than the total energy. Assuming the forces are converged, then the following applies.

The argument for equation (V.15) was the invariance of the energy of the system under a rigid shift of all the atoms — equivalent to a co-ordinate shift. After such a shift, the unit cell vectors are obviously unchanged, hence so are the reciprocal unit cell vectors, the k-points, and the basis set in which the wavefunctions are described. The wavefunctions themselves will change, but in reciprocal space, and hence in the plane wave basis, each component is just multiplied by a complex phase factor, an operation which can be done "exactly."

Atom	position
Si	$(0, 0, 0)$
C	$(\frac{1}{3}, \frac{1}{3}, \frac{1}{8})$
Si	$(\frac{1}{3}, \frac{1}{3}, \frac{1}{2})$
C	$(0, 0, \frac{5}{8})$

Table V.2: Atomic positions within the unit cell for 2H SiC.

It would seem that equation (V.15) does indeed hold, but for one snag. The real space FFT grid has moved relative to the atoms, and hence relative to the charge density. Quantities calculated on this grid may therefore change, and the most important of these is the exchange correlation energy. Given this, it would be reasonable to assume that a shift of an integer multiple of the real space FFT grid cell would leave the energy invariant, but that any other shift might change it.

It is worth investigating the accuracy of the above deductions, and the magnitude of this change in energy and the resulting forces. The system chosen for a few test calculation was 2H silicon carbide in a two layer hexagonal cell. This is computationally the simplest structure considered, but it retains the hexagonal geometry used throughout this work. The positions of the atoms with respect to the unit cell axes are as given in table V.2. The cut-off used was 560 eV, the lower of the cut-offs used for the SiC calculations in this work, for the effect should be more marked at lower cut-offs.

A choice of FFT grid of $24 \times 24 \times 40$ will place each atom precisely on a grid point. This FFT grid is also the smallest to include all reciprocal space vectors of length $2|\mathbf{g}_{max}|$, the criterion described in section IV.2.7 which gives a grid size of 39.6 in the c direction. The atoms can then be shifted by $\frac{c}{40}$ and $\frac{c}{80}$ in the c direction. The former should produce no change in the energy, whereas the latter should produce the maximum change.

On shifting the whole system by one FFT grid cell there was no change in the total energy of the system (to 0.1μeV in 526eV), and no change in the final forces (to 1μeVÅ^{-1}). However the sum of the forces was not zero, but 270μeVÅ^{-1}. This agrees fully with the above analysis, and places some limits on the accuracy of the forces arising from CASTEP.

The shift of one half of an FFT grid cell, which is 0.063Å, did produce an energy change of 0.24meV, and the new sum of the forces was still 270μeVÅ^{-1}. The actual value of the forces changed by 2.6μeVÅ^{-1} for the Si atoms, and 240μeVÅ^{-1} for the C atoms.

As the silicon pseudopotential is so much softer than the carbon pseudopotential, the charge density in the vicinity of the silicon will be much smoother than that near the carbon. Thus the dominant contribution to the above affect will be from the two carbon atoms in the cell. This is confirmed by the much smaller change in the force on the silicon atoms compared to

Grid size (in z)	ΔE (meV/pair)	ΔF (C) (meV/Å)
40	0.120	2.78
36	0.256	5.29
32	0.504	10.91

Table V.3: Maximum changes in energy and forces on performing a rigid shift at various FFT grid sizes.

the carbon atoms after the shift. The carbon atoms are equivalent, so that the energy shift can be partitioned as 0.12meV/atom, which over 0.063Å is equivalent to a force of 2meVÅ^{-1}. This energy change is a worst–case result, so that in a 'real' system the noise in the error could not be more than $\pm 0.06n$meV, where n is the number of carbon atoms, and is probably closer to $\pm 0.04n^{\frac{1}{2}}$meV, as there is no reason for the carbon atoms to add in unison, and the root mean square error will be about half the peak value.

Table V.3 summarises such data for three grid sizes for calculations on wurtzite. The calculations were done at zero, one quarter and one half of a grid cell shift. That a spherically symmetric atom on, or half way between, grid points can have no resultant force due to interactions with the grid is clear from symmetry considerations, so these two points represent energy extrema. The force would be expected to be extremised half way between these points. The tabulated ΔE is the difference between these two expected energy extrema, whilst the ΔF is the difference caused by a shift of $\frac{1}{4}$ of a grid cell, that is the expected peak, rather than peak–to–peak, variation in F.

The errors can be seen to increase exponentially as the grid size is reduced, although they still remain reasonably small. The change in the force on the silicon atom on such a shift, which is not tabulated here, was always at least a factor of 60 below that on the carbon atom. These data will permit some estimate of the error due to the coarseness of the FFT grid to be made.

V.4.3 Relaxation methods

Given a set of forces, there are many ways of attempting to move the ions towards their equilibrium positions. The simplest method is to move each ion in the direction of the resultant force on it a distance proportional to the force. As long as the proportionality constant is small, this scheme should lower the energy at every step, but convergence will be very slow.

Original method

The technique used by CASTEP when this work was started was more sophisticated than the above method. Again it displaced each atom in the direction of and proportional to the resultant force on the atom, but the choice of distance was more complicated. In outline, the scheme was as follows. A trial displacement of the ions was attempted, and the linear response of the electronic wavefunctions to this movement calculated. The energy of the trial position was then calculated according to the wavefunctions updated by the linear response. Then a quadratic was fitted to the known initial energy and gradient thereof with respect to ionic displacement in the chosen direction, and the energy of the trial position. The minimum of this quadratic was found, and a step taken to this point, moving the ions and updating the wavefunctions according to the linear response. Thus an attempt is made to calculate the optimal distance to move the ions, and the electronic wavefunctions are partially updated for the resultant change in the ionic potential.

The scheme has several weaknesses. The linear projection of the wavefunctions is bound to result in a wavefunction at the trial position which is not the ground-state and thus has higher energy than the ground state. The energy at the trial position is therefore overestimated, and the step taken towards it will always be too short. As implemented, the scheme used a fixed number of electronic iterations after an ionic step in order to reconverge the electronic wavefunction. This is not necessarily appropriate. Finally, the initial direction of the ionic displacement, although optimal for a general case with no prior knowledge of the system, is poor near a free surface.

Having implemented the dipole correction discussed above, there remained a choice of either altering the existing scheme to work correctly with the new potential, or writing a new one. The second route was chosen, because of the inefficiency of the undershooting of the above scheme. In rewriting the relaxation routine, a quick and simple route was chosen in order to reduce coding time. This is justified by the simplicity of the relaxation problem — just nine atoms relaxing constrained by symmetry to have one degree of freedom each.

The new relaxation scheme

Although the choice to produce something quick and simple had been made, there was one obvious area where a considerable improvement could be made over the schemes discussed above. Whereas they assume the atoms relax independently in quadratic wells fixed in space, when relaxing a surface a better model is that of a chain with a free end. This can significantly alter the direction in which the ions are moved, and is illustrated here for a simple case.

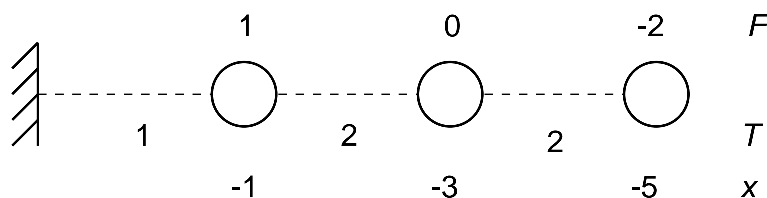

Figure V.12: A ball and spring chain showing the resultant force on each ball (F), the tension in each spring (T), and the relative motion required by each ball to relax the tension in all springs (x). Note that this motion is not necessarily in the same direction as the resultant force on the balls.

Figure V.12 shows a chain of three balls joined by springs, free at one end and fixed at the other. The resultant forces on each atom are shown, as are the tensions in the springs joining them. In order to relax the system, it is the tensions in the springs which must be reduced to zero, and these vary linearly with the spring length. From the resultant forces on the atoms, the tensions in the bonds are sought. Each bond is then relaxed an amount proportional to its tension, and the atomic displacements for such a relaxation calculated. As can be seen from the example given, the trial directions in this scheme do not necessarily have the same sign as in the fixed potential well model.

For this example, CASTEP's ionic displacement would be α, zero and -2α for the three atoms, optimised by adjusting α. However the spring to the left of the first atom was stretched and is stretched further by this displacement. The revised scheme proposed here would use a displacement of $-\alpha$, -3α and -5α, thus shortening all the bonds under tension.

There remains the problem of finding the optimum value of α. This is done by CASTEP by a trial ionic step and linear projection of the electronic wavefunctions as described above. The new routine tried something simpler. For the first relaxation step, a "guessed" value of α was used, in the region of the optimum, but perhaps a factor of two or so in error. When the next ionic step was to be taken, the new ionic displacement vector was compared with the old. If the previous step had been of optimal length, the old and the new vector should be orthogonal, as no further relaxation would be required in the direction previously taken. By calculating the dot-product of the old and new vectors, the degree of overshoot or undershoot on the previous step was determined and α adjusted accordingly. If the atoms did suffer from identical nearest–neighbour quadratic potentials only, these scheme would find the minimum in two steps, a fact which was used to test the coding of the scheme.

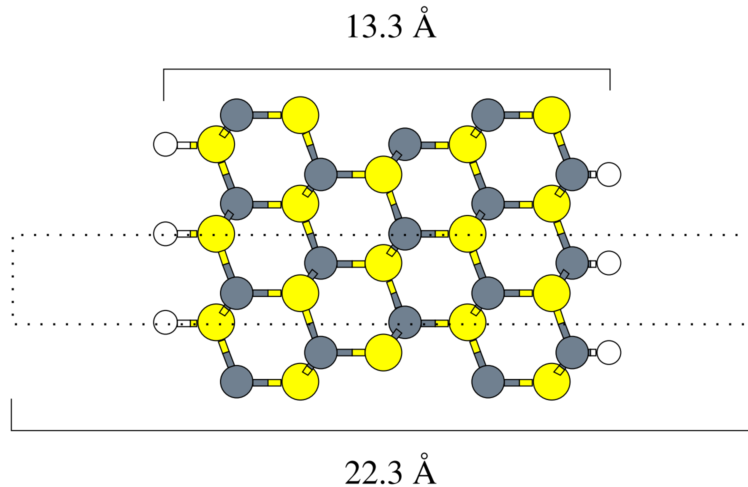

Figure V.13: The five layer SiC slab, with 9Å of vacuum. The unit cell is shown by the dotted line.

System	Energy (eV)	Energy difference (meV)
Cubic	–1346.97642	
C reversed	–1346.97274	3.68
Si reversed	–1346.98201	–5.59

Table V.4: Unrelaxed 5 layer SiC systems and their energies.

V.5 Results & analysis

V.5.1 Results

The systems discussed first will be those of five layers of SiC and 9 Å of vacuum, measured from between the hydrogen nuclei, as shown in figure V.13. Unless otherwise stated, these systems have the self-consistent dipole correction described in section V.3.2 applied to them.

Firstly, table V.4 presents the unrelaxed energies of the three systems: that is all layers in the cubic stacking direction, the carbon surface layer reversed, and the silicon surface layer reversed.

When relaxation is permitted, only relaxation of the atoms in the c direction is permitted: if symmetry is maintained, movement in the a-b plane is impossible. Relaxation of the unit cell vectors themselves was not thought to be important, considering that the layers of bulk will fix the lattice constant regardless of whether a surface layer is reversed, and the effect of varying the lattice constant on the polytype energy differences was very small. The freedom of the layers to move in the c direction means that only the a and b lattice constants are

System	Energy (eV)	Energy difference (meV)
Cubic, C relaxed	–1347.0157	
C reversed	–1347.0143	1.4
Cubic, Si relaxed	–1347.0113	
Si reversed	–1347.0230	–11.7

Table V.5: Relaxed 5 layer SiC systems and their energies.

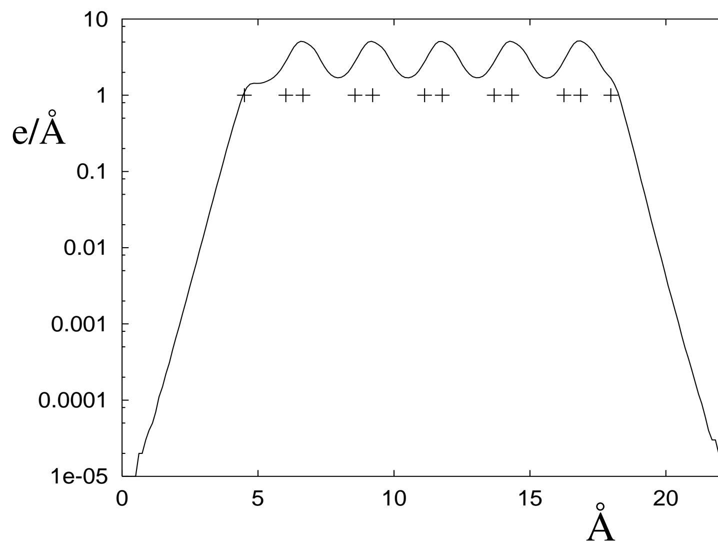

Figure V.14: The charge density along the c axis of the unit cell. The crosses mark the positions of the atoms, which are, from left to right, $H(SiC)_5H$.

being held fixed. The relaxation was limited to the surface being reversed and the immediate sub-layers, so that rather than relaxing all 12 atoms present, just 9 were permitted to move. The gain from this appears to be small, but the decision to follow this route was taken when it was expected that more bulk layers would be required. The consequence is that the cubic system needs to be calculated twice: once with the silicon surface relaxed, and once with the carbon surface relaxed. Table V.5 shows these results, and figure V.14 the charge density for a typical system. The charge density is plotted along c, with the perpendicular area of the unit cell integrated over, so that the units are eÅ^{-1}, and the integral of the figure shown is the total number of electrons in the cell, that is 42. The exponential fall-off of the charge density into the vacuum region and down to very low levels can be clearly seen.

To give more detail of these calculations, they were all done with a 560 eV cut-off, a 7×7 Monkhorst Pack k-point mesh in the a^* b^* plane, with $c^* = 0$ so as to reduce the number of k-points after symmetrisation to just 8. The apparently poor sampling in the c^* direction is not important because of the large difference in length scales between the c and a b directions in real space. The modulus of a is just under 3.1 Å whilst that of c is just over 22 Å, and thus

System	Energy (eV)	Energy difference (meV)
Cubic	–1610.19948	
C reversed	–1610.19580	3.68
Si reversed	–1610.20509	–5.62

Table V.6: Unrelaxed 6 layer SiC systems and their energies.

the position of the first failure star is still determined by the sampling perpendicular to c^*. In other words, the distance between k-points perpendicular to c^* was 0.29 Å^{-1}, and parallel to c^* was 0.28 Å^{-1}.

The FFT mesh was $24\times24\times180$ – sufficient by the criteria given earlier. To give an indication of the time required for these calculations, electronic convergence took 30 iterations, and ionic relaxation a further 100 iterations, with each iteration taking about 18 minutes of CPU time on a DEC Alpha workstation (262 SPEC92fp). Thus each fully relaxed calculation took around 40 hours. The memory requirement was around 50 Mb.

V.5.2 Convergence

Before claiming that the above results stand, it is necessary to check that convergence with respect to cell size had indeed been reached with five layers and the chosen vacuum size. Hence the unrelaxed calculations were repeated with six layers and 10 Å of vacuum, with the FFT grid extended to $24 \times 24 \times 192$. The unrelaxed results are given in table V.6. The level of agreement between this table and table V.4 for the 5 layer system is remarkable, and suggests that the energy differences are indeed converged with respect to vacuum size and bulk size. This good agreement is retained after relaxation, the reversal of the carbon face costing 1.4 meV, and that of the silicon face –11.6 meV.

Tests of convergence with respect to cut-off and k-point sampling are shown in tables V.7 and V.8. Just the energies of the unrelaxed systems with neither surface reversed and the carbon surface reversed are calculated, as the results give a clear indication that convergence has indeed been reached, and to relax the structures would take considerably more computational effort. Again it is clear, particularly from the convergence in the cut-off energy, that the difference between the structures is much better converged than the total energy.

Finally the effect of the dipole correction should be noted. Table V.9 shows the result of calculating the total energy and the dipole moments of an unrelaxed slab with no surface reversal. It can be seen that the *post hoc* correction over–corrects the energy by a considerable margin — not surprising when the large change in the dipole moment on removing the dipole–dipole interaction is considered.

Cut-off (eV)	Total energy (eV) No reversal	C reversed	Difference (meV)
560	–1346.97642	–1346.97274	3.66
600	–1347.24369	–1347.24001	3.67
650	–1347.43421	–1347.43050	3.71

Table V.7: Convergence of unrelaxed systems with respect to cut-off energy.

k-point mesh	Total energy (eV) No reversal	C reversed	Difference (meV)
$7 \times 7 \times 1$	–1346.97642	–1346.97274	3.66
$9 \times 9 \times 2$	–1346.98462	–1346.98106	3.56

Table V.8: Convergence of unrelaxed systems with respect to k-point sampling.

In appendix B an improved version of the *post hoc* dipole correction is derived, which replaces the $1/\epsilon$ in the correction term with the average value of this quantity throughout the unit cell. For SiC, ϵ_r is 9.7 [104], which when applied to the full 13.3 Å of the slab gives an averaged value of 2.15 for ϵ_r. With this value of ϵ_r the improved *post hoc* and self-consistent corrections give very similar energies. It must not be thought that this improved *post hoc* energy correction solves all the problems caused by the dipole and periodic boundary conditions. Although the energy may be correctable, the field in the vacuum is still non-zero, so that the charge density is affected, as seen by the different dipole moment produced. The forces on the atoms are also changed. As one example, in this unrelaxed configuration the surface silicon atom has a force of 0.15 eV/Å on it in the self-consistent calculation. In the non self-consistent calculation this is only 0.10 eV/Å. Thus the relaxed ionic configurations would differ.

V.5.3 Accuracy

Estimating the errors in LDA calculations is never easy, but a reasonable analysis follows. The cut-off and k-point mesh gave errors of less than 0.15 meV/pair when used for the polytype energy differences in chapter IV and compared to much higher cut-offs and denser meshes. For a five layer cell the errors could be as large as 0.75 meV for each, but are likely to be smaller. The FFT grid could cause errors of up to 0.12 meV per carbon and hydrogen atom, but remembering that one carbon and one hydrogen atom are in identical positions in each calculation, and the others are in similar positions with respect to the grid, the total error

Energy (eV)				Dipole moment (eÅ)	
uncorrected	*post hoc*	improved *p.h.*	self-consistent	uncorrected	self-consistent
–1346.9813	–1346.9705	–1346.9763	–1346.9764	0.1476	0.0674

Table V.9: Effect of dipole corrections on unrelaxed SiC slab.

System	Energy (eV)	Change on relax. (meV)	$\sum \mathbf{F}^2_{atom}/2k$ (meV)	$\sum \mathbf{F}^2_{bond}/2k$ (meV)
NC	–1346.97642	39.2	30.0	43.3
NC, relaxed	–1347.01567	-	0.006	0.04
NSi	–1346.97642	34.9	2.1	49.1
NSi, relaxed	–1347.01129	-	0.004	0.10
C	–1346.97274	41.5	27.6	49.8
C, relaxed	–1347.01427	-	0.008	0.14
Si	–1346.98201	41.0	4.5	51.2
Si, relaxed	–1347.02303	-	0.024	0.19

Table V.10: Estimating errors due to incomplete relaxation. NC – no reversal carbon face, NSi – no reversal silicon face, C – carbon surface reversed, Si – silicon surface reversed.

here is likely to be less than 0.2 meV. The FFT grid was chosen to ensure that the surface reversal moves the surface atoms from grid line to grid line, as the lines $(0, 0, z)$, $(\frac{1}{3}, \frac{1}{3}, z)$ and $(\frac{2}{3}, \frac{2}{3}, z)$ are all on lines of the real space grid.

The error due to the lack of total relaxation is more difficult to calculate. The usual approach, such as that used by Cheng *et al.* [48], is to sum over the residual forces, assuming Hooke's law, and take

$$\Delta E = \sum_n \frac{\mathbf{F}_n^2}{2k} \tag{V.16}$$

where k is a suitable spring constant for the bond — for SiC this is 18 eVÅ^{-2} calculated from the bulk modulus given earlier by the method of Yean and Riter [91]. However, one could argue that the $\mathbf{F}_n$'s used should not be the resultant forces on each atom, but rather the internal forces in each bond following section V.4.3. Applying these schemes both before and after relaxation gives table V.10.

This table shows that consideration of the forces in the bonds, rather than on the atoms, gives a much better estimation of the amount of relaxation remaining. This supports the basis of the new relaxation scheme of section V.4.3 as being a good representation of the system. It also shows that all the relaxed structures are relaxed to within 0.2 meV of their true minima.

Thus the total error from the lack of complete relaxation and the various finite grids used would be expected to be about 0.5 meV. The errors due to the use of the LDA and pseudopotentials are probably of similar magnitude. The energy difference of 1.4 meV for reversing the carbon face is at the limit of clear detectability. The 13 meV difference between this result and the corresponding result for the silicon face is much larger than any possible errors.

V.5.4 Analysis

This work has for the first time investigated SiC polytype growth using *ab initio* methods and in a manner which can distinguish between the Si and C surfaces. The difference between them is found to be surprisingly large, with reversing a Si-terminated face 13.1 meV/pair easier than reversing a C-terminated face. Clearly such a large effect ought not to be ignored in future work on this aspect of SiC growth.

The old model of the energy change on reversing a surface layer being twice the sum of the J_n's gives values between 3.6 and –3.1 meV/pair. These values are in the region of the result given here for the carbon face, but fail to describe the silicon face result of –11.7 meV/pair at all. The reason for this is not explained by some anomalous atomic relaxation on the Si face, for the relaxed data follow broadly the unrelaxed data, but must be contained within the electronic structure of the two surfaces.

The expected growth pattern from these calculations would be that the carbon surface of a cubic crystal would continue to grow cubic, this being preferred by 1.4 meV/surface pair in the growth process. The silicon face would show a strong preference for introducing a stacking reversal, with an energy of 11.7 meV/surface pair preferring this (see table V.5). This result would be supported by the work of Lilov *et al.* (figure II.5 on page 13) who found that the carbon face grew a higher percentage of the cubic polytype than the silicon face did. On the other hand, Stein and Lanig and Yoo (section II.3.3) find a strong preference for the growth of 4H on the carbon face and 6H on the silicon face. As 4H contains more stacking reversals than 6H, this preference is contrary to the suggestion of this work.

This work has also served to test three different corrections for the dipole–dipole interaction energy arising from periodic boundary conditions. The self-consistent and the improved *post hoc* correction described give almost identical corrections to the electronic energy, although the forces given differ. The more simplistic *post hoc* correction is shown to be significantly in error, overcorrecting by a factor of just over two, and thus being marginally worse than no correction at all in this case.

It might seem that no correction was strictly necessary, for although the error in the total energy if none had been applied would have been 5 meV/pair, the error in the energy differences would have been rather less, as the dipole moments varied by less than 10% between the systems, suggesting an error in the differences of around 1 meV. However, it was only through the careful analysis above that this of conclusion could have been reached, and the method used does benefit from the complete removal of the electric field which would have affected the relaxation.

Chapter VI

Conclusions and Further Work

VI.1 Phonon Stabilisation of Polytypes

The work of Cheng *et al.* [48] on the phonon spectra of specific silicon carbide polytypes suggested that, as temperature increased, the sequence of stability would be 4H, 15R, 6H. The work said nothing about the nature of the boundary–boundary interaction, and conjectured about the existence of other phases.

This work, using a simple and general phonon model reproduces the 4H, 15R, 6H sequence without being fitted in any way to Cheng's data. It also gives the form of the boundary–boundary interaction as being $\pm 1/n^2$, the sign alternating every time an intervening boundary is traversed. No other phases are found to be stable within this model, thus no devil's staircase results, just a single step.

Although the model used is quite general, it does lack some of the details of silicon carbide's geometry, especially the manner in which adjacent layers of SiC are displaced slightly to one side rather than directly above each other. This may give rise to more complex interactions, as described by Shaw and Heine [51]. The approximate treatment of long–range effects may also have masked some small energy change which could be sufficient to stabilise more intermediate polytypes.

Thus this is far from being the last word on the existence of a devil's staircase in silicon carbide, although it does provide considerable evidence against.

VI.2 Different growth on different sides of slab

The work on the energy change on reversing a surface layer of silicon carbide produces a clear distinction between the silicon and carbon faces. This is in contrast to previous work which used layer spin models which are unable to distinguish between the two types of surface.

The difference between the energy of a stacking boundary at either surface is found to be large — over 10 meV per pair. This may be surprisingly large, but it does reflect the different properties of the surfaces, such as diffusion length or oxidation rate [105], and the different growth on them observed experimentally.

VI.3 Need to allow a reconstruction?

The most obvious deficiency of the calculations of the electronic surface reorientation energies is the absence of any surface reconstruction. Conceptually this is simple to include; computationally it is expensive, with the cost of even a 2×1 reconstruction being a factor of four on memory usage and a factor of about twenty on cpu time. The loss of symmetry does make the use of parallel computers and the existing parallel version of CASTEP (known as CETEP) attractive, at which point the increase in CPU time becomes less of an issue, as long as the reconstruction is fairly simple. Other modifications of technique, such as the use of softer pseudopotentials [106] and the use of real space projection for the pseudopotentials [107] would help to reduce the CPU time requirement of these larger calculations. Calculations of simple surface reconstruction energies have recently been done [108], and did utilise very soft pseudopotentials with a 260 eV cut-off.

Clearly the results of the calculations here are not yet in total accord with experimental data, and this is the most significant deficiency. Beyond this would lie the details of the atom-by-atom growth process which will remain out of the range of *ab initio* calculations for many years to come.

VI.4 Role of impurities

It is almost impossible to use a code such as CASTEP to study impurities at low concentrations. For carbon containing compounds with surfaces, even parallel computers are limited to systems of about 100 atoms, where the smallest possible impurity concentration is 1%. However, it has been suggested that boron may promote the growth of the 2H by some mechanism which enables it to stay on the surface of the growing crystal, so that the bulk concentration

is low, but the surface concentration high. This suggestion follows the work of Headrick *et al.* [109] who showed that if a third of a monolayer of boron is placed on a silicon (111) face — that is the face corresponding to (0001) in a hexagonal basis — the subsequent growth of silicon remains cubic but the stacking direction is reversed, the boron being buried. Perhaps in silicon carbide, the boron stays on the surface, causing each layer to reverse the stacking direction.

VI.5 Study of surfaces

The corrections for the interaction of the dipole moments of a surface and its periodic image described here has utility stretching far beyond the study of silicon carbide. Most surfaces suffer from this interaction when studied with plane-wave codes, and these techniques enable accurate answers to be obtained with smaller cell sizes the previously possible. The self consistent correction can be trivially extended to enable calculations to be done in artificially–imposed electric fields, such as those in tunnelling microscopes or cold–cathode displays.

This thesis has described the determination of a temperature dependent interaction between stacking boundaries given by a simple phonon model, and its consequences for the stability of long-period silicon carbide polytypes. Furthermore it has presented careful electronic structure calculations of the energies of stacking boundaries at surfaces, and in doing so produced a clear distinction between the silicon and carbon surfaces, as well as giving a general analysis of corrections for the dipole–dipole interaction caused by the imposition of periodic boundary conditions. The study of polytypism in silicon carbide as both an equilibrium and a growth phenomenon is thus advanced.

Appendices

Appendix A

Dispersion curve for 2D phonon model

The 2D phonon model of chapter III is sufficiently simple that it can be analysed analytically a little further, and in doing so the results of the numeric code can be checked. For the case of no stacking boundaries, the motion of the infinite system can be described via Bloch's theorem by considering one unit cell as shown in figure A.1.

Phase factors between the displacements of neighbouring atoms are shown as $\exp(i\theta)$ along the x direction and $\exp(i\phi)$ along the y direction. The equation of motion for the displacement

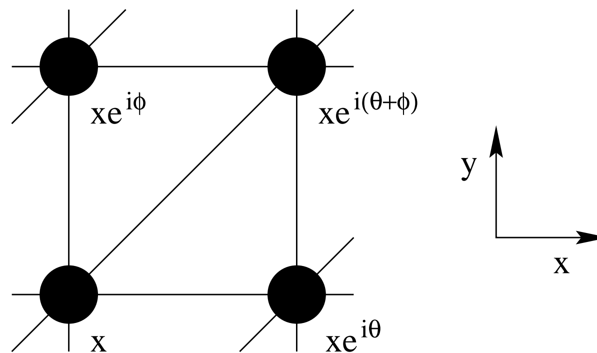

Figure A.1: One unit of the 2D phonon model with the displacements from equilibrium in the x direction marked. The lines represent springs.

from equilibrium of an atom in the x direction is

$$\begin{aligned} m\ddot{x} &= kx\left(e^{i\theta} - 2 + e^{-i\theta}\right) + \frac{1}{2}kx\left(e^{i(\theta+\phi)} - 2 + e^{-i(\theta+\phi)}\right) + \frac{1}{2}ky\left(e^{i(\theta+\phi)} - 2 + e^{-i(\theta+\phi)}\right) \\ -m\omega^2 x &= kx(2\cos\theta + \cos(\theta+\phi) - 3) + ky(\cos(\theta+\phi) - 1). \end{aligned} \tag{A.1}$$

The equation for the motion in the y direction is given by swapping x and y in the above equation.

The equation for the normal modes is just

$$-m\omega^2\mathbf{x} = \underline{\underline{\mathbf{F}}}\mathbf{x} \tag{A.2}$$

so the eigenfrequencies are given by the roots of

$$|\underline{\underline{\mathbf{F}}} + m\omega^2\underline{\underline{\mathbf{1}}}| = 0. \tag{A.3}$$

Setting $m = k = 1$,

$$\underline{\underline{\mathbf{F}}} = \begin{pmatrix} 2\cos\theta + \cos(\theta+\phi) - 3 & \cos(\theta+\phi) - 1 \\ \cos(\theta+\phi) - 1 & 2\cos\theta + \cos(\theta+\phi) - 3 \end{pmatrix}. \tag{A.4}$$

The roots of equation (A.3) are

$$\omega^2 = 3 - \cos\theta - \cos\phi - \cos(\theta+\phi) \pm 2\sin\frac{1}{2}(\theta+\phi)\left[1 - \cos\theta\cos\phi\right]^{\frac{1}{2}}. \tag{A.5}$$

This expression can then be manipulated to reveal that the maximum value of ω^2 is $4+2\sqrt{2}$, or to give the full dispersion curve.

Two checks on the code used in chapter III are then possible. The value of Ξ_0 for the 120×48 grid can be calculated, as can the maximum ω^2 in the resulting eigenvalues. Ξ_0 can also be evaluated from equation (A.5) by summing the logs of each of the roots for θ between $-59\pi/60$ and π in 120 equal steps and ϕ between $-23\pi/24$ and π in 48 equal steps, excluding the point $\theta = \phi = 0$. These two equivalent evaluations of Ξ_0 agree to 12 significant figures, and the maximum value of ω^2 is found to be $4+2\sqrt{2}$ to 14 significant figures (the maximum occurs at $\theta = 0$, $\phi = \pi$ and $\theta = \pi$, $\phi = 0$ so it is sampled). These errors represent the machine precision when performing the required matrix manipulation with double precision arithmetic, and therefore show that the code written for chapter III was performing precisely as intended.

Appendix B

Improved *post hoc* dipole correction

The theory of a *post hoc* dipole correction was briefly sketched in section V.3.2. There now follows a more detailed derivation for the case where vacuum does not predominate in the unit cell.

Figure B.1 shows a simple model of a general system. In the centre is a dielectric, representing the slab of material in the cell. On each surface of the slab there is a metal plate, with equal and opposite charges on them. This enables a dipole moment to be introduced into the system. At the edges of the cell are two further metal plates. These can have their potential adjusted in order to represent the boundary conditions of the cell.

The electrostatics of this system are most readily analysed by converting it to the equivalent circuit of capacitors. This is shown in figure B.2. The dielectric slab has become C_1, with C_a and C_b representing the boundary conditions. The left-hand plate of C_a gives the boundary condition at the left-hand edge of the cell, whereas the right-hand plate is the left-hand surface of the metal plate on the dielectric's surface. Thus the charge q on the plate on the dielectric's surface on figure B.1 is clearly split between that on the inner surface producing the field in the dielectric, now found on C_1, and that on the outer surface producing the field in the vacuum, now found on C_a.

For the case of an isolated slab, the boundary conditions are those of zero field in the vacuum,

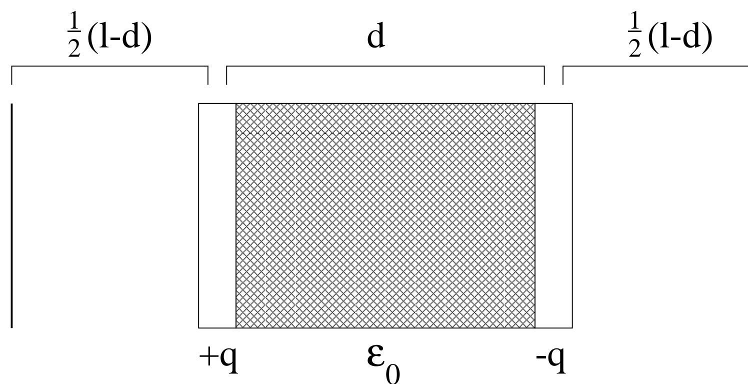

Figure B.1: Electrostatic model of a dipolar polarisable slab in a unit cell.

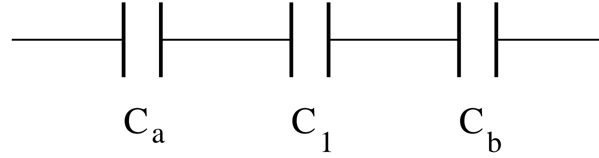

Figure B.2: Capacitor model of a dipolar polarisable slab in a unit cell. C_1 represents the slab, and C_a and C_b the vacuum regions on the left and right.

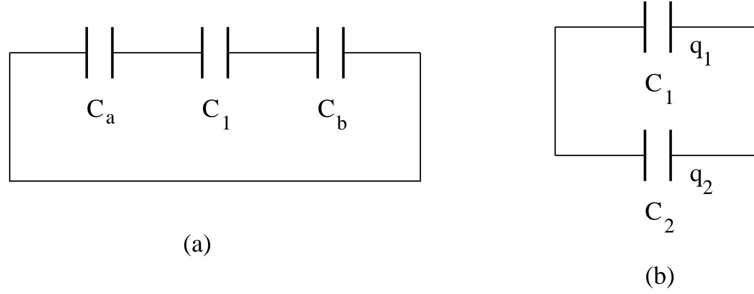

Figure B.3: Capacitor model of a dipolar polarisable slab in a unit cell with periodic boundary conditions. The circuits (a) and (b) are electrically equivalent.

that is no charge on C_a and C_b. The electrostatic energy is thus simply

$$E = \frac{1}{2}\frac{q^2}{C_1} \tag{B.1}$$

with

$$C_1 = \frac{A\epsilon_0\epsilon_r}{d}. \tag{B.2}$$

The dipole moment of this system, p_0, is not qd because of the additional polarisation charges produced by the dielectric. Rather

$$p_0 = \frac{qd}{\epsilon_r}. \tag{B.3}$$

When the periodic boundary conditions are imposed, this is equivalent to setting the potential at the edges of the cell to be the same. In terms of the capacitors, this is achieved by connecting the two ends of the circuit which were previously left floating. This is shown in figure B.3, where the separation of the charge q into two parts providing the field in the dielectric and vacuum is very clear. This assists in calculating the new total dipole moment of the system, which is now

$$p = \left(\frac{q_1}{\epsilon_r} + q_2\right) d. \tag{B.4}$$

The value of the second capacitor is given by

$$C_2 = \frac{A\epsilon_0}{l-d} \tag{B.5}$$

and the charges divide in proportion to the capacitances, with

$$\begin{aligned} q_1 &= \frac{qC_1}{C_1 + C_2} \\ q_2 &= \frac{qC_2}{C_1 + C_2}. \end{aligned} \tag{B.6}$$

This enables p to be rewritten as

$$p = \frac{qd}{C_1 + C_2}\left(\frac{C_1}{\epsilon_r} + C_2\right) \tag{B.7}$$

The new electrostatic energy is

$$E' = \frac{1}{2}\frac{q^2}{C_1 + C_2} \tag{B.8}$$

and by subtracting this from equation (B.2) an energy difference of

$$\begin{aligned} \Delta E &= \frac{1}{2}q^2\left(\frac{1}{C_1} - \frac{1}{C_1 + C_2}\right) \\ &= \frac{1}{2}\frac{q^2}{C_1 + C_2}\frac{C_2}{C_1} \end{aligned} \tag{B.9}$$

is obtained.

In order to obtain useful information from the above equations, a little more algebra is necessary. Two intermediate expressions are required:

$$\frac{C_2}{C_1} = \frac{d}{\epsilon_r(l - d)} \tag{B.10}$$

and

$$\begin{aligned} \frac{C_1}{\epsilon_r} + C_2 &= A\epsilon_0\left(\frac{1}{d} + \frac{l}{l - d}\right) \\ &= \frac{\epsilon_0 V}{d(l - d)}. \end{aligned} \tag{B.11}$$

Using these, the expression for the energy difference can be transformed as follows:

$$\begin{aligned} \Delta E &= \frac{1}{2}q\,\frac{q}{C_1 + C_2}\,\frac{C_2}{C_1} \\ &= \frac{1}{2}q\,\frac{q}{C_1 + C_2}\,\frac{d}{\epsilon_r(l - d)} \\ &= \frac{1}{2}\frac{qd}{\epsilon_r}\,\frac{qd}{C_1 + C_2}\frac{1}{d(l - d)} \\ &= \frac{p_0 p}{2\epsilon_0 V}. \end{aligned} \tag{B.12}$$

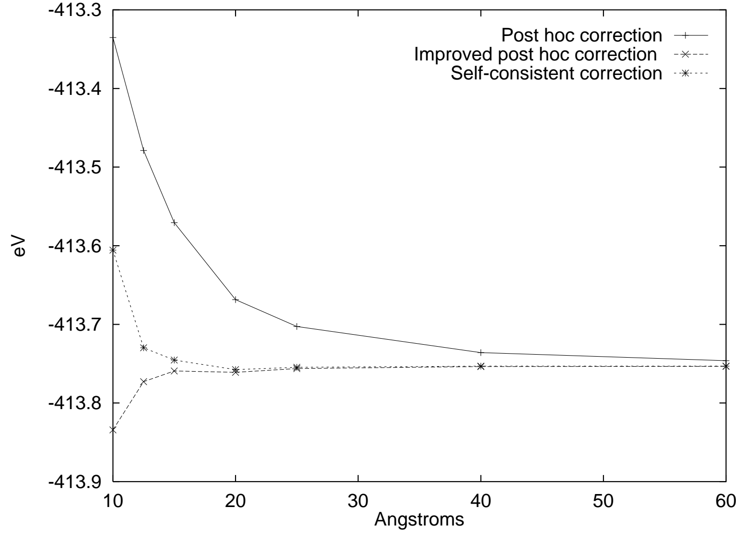

Figure B.4: The improved *post hoc* correction applied to the data of figure V.10.

This expression should be compared with the previous expression of section V.3.2 of $p^2/2\epsilon_0 V$ (page 84). The error in the original expression is simply given by the amount by which the measured dipole moment differs from its value in the infinite unit cell. This new correction can now be applied to the data of figure V.10 on page 88. The value of p_0 can be taken as 1.255 eÅ from table V.1 and then the resulting correction produces figure B.4.

Although the corrected data are now as good as the data from the self-consistent calculation, the comparison is unfair. The value of p_0 from the self-consistent calculation was needed before the improved *post hoc* correction could be applied. Unless p_0 can be estimated from p the new correction is useless.

It is possible to relate p and p_0 through l, d and ϵ_r. Doing so is only of use if these variables are known, but for a simple slab l and d can be estimated and ϵ_r taken from a data book.

Skipping a few steps in the algebra,

$$\begin{aligned} p &= \frac{\epsilon_r p_0}{C_1 + C_2}\left(\frac{C_1}{\epsilon_r} + C_2\right) \\ &= p_0\left(\frac{l}{(l-d) + d/\epsilon_r}\right) \\ p_0 &= p\left(\frac{l-d}{l} + \frac{d}{\epsilon_r l}\right) \\ &= p\,\langle\frac{1}{\epsilon_r}\rangle \end{aligned} \tag{B.13}$$

where the average is justified in this geometry, and is probably more generally correct. The

final energy correction is

$$\Delta E = \frac{p^2}{2} \langle \frac{1}{\epsilon} \rangle. \quad \text{(B.14)}$$

So for a system with a significant amount of dipolar material, the $1/\epsilon$ term of equation (V.7) should be replaced by its average value throughout the cell. This is possible for the SiC slab, but rather more difficult for the KCl slab. For an atom such as potassium, its polarisability varies as a function of its ionisation, and as the dipole moment is changing at constant bond length, the ionisation must also be changing. This variation in polarisability is dramatic, with K taking the value of 43.4 Å^3, and Ar, which is electronically equivalent to K^+, 1.6 Å^3 [104]. Determining the appropriate value to apply to the system would be rather difficult.

Appendix C

Thermal electronic effects

It has been mentioned that the large band-gap of SiC means that the change in electronic free energy at non-zero temperatures is very small. Considering how small the energy differences in general are, this is now quantified loosely.

The free energy of an electron can be obtained from its partition function, where the electron is here considered to be in a two level system with separation E_g and a very low probability p of being in the higher level. Then

$$\begin{aligned} Z_e &\approx 1 + p \\ F_e &= -kT \ln Z_e \\ &\approx -kTp \\ &= \frac{-kTn_c}{N} \end{aligned} \tag{C.1}$$

Where n_c is the density of carriers and N the total density of valence electrons. Ashcroft and Mermin give a simple formula for n_c [110] which assumes that the density of states near the band gap rises as $\sqrt{E}$ in the region of interest. Simplifying this further to assume that the effective mass of the electrons and holes is simply the electronic mass, and that the valance band maximum is four-fold degenerate, results in

$$n_c = 10^{-4} \times \left(\frac{T}{300}\right)^{\frac{3}{2}} \exp\left(\frac{E_g}{2kT}\right) \tag{C.2}$$

with n_c in units of Å^{-3}. From the lattice constant of 3C SiC, N may be calculated as 0.385 Å^{-3}.

The electronic free energy per SiC pair, F_{el} is required. This can be obtained by combining the above equations to give

$$F_{el} = -5.0 \times 10^{-8} kT^{\frac{5}{2}} \exp\left(\frac{E_g}{2kT}\right). \tag{C.3}$$

Evaluating this for an extreme case, 3C (E_g = 2.3 eV) at 2500K, results in an F_{el} of -6.5 μeV/pair, with the hexagonal polytypes around -1 μeV. Thus this effect is much smaller than the accuracy of the *ab initio* electronic calculations, and is much smaller than the contribution to the total free energy differences from the phonon spectra.

Appendix D

Polytype energies from J_n's

The energy of silicon carbide has been expressed in terms of a spin model based on layers in a manner such as

$$E = J_0 N - \sum_{i,n} J_n \sigma_i \sigma_{i+n} \tag{D.1}$$

(equation (II.3) on page 17). With the assumption that $J_n = 0$ for $n > 4$ this is now applied to simple bulk polytypes.

As each unit cell will contribute identically, the sum over i need only be done within a unit cell. The sum over n is truncated to $n \leq 4$. The polytype structures are shown in figure D.1, and the summations will be done considering the interactions on a layer from layers to its right only, in order to avoid overcounting.

The resultant expressions for the energies, quoted now per layer, are:

$$\begin{aligned}
E_{3C} &= J_0 \quad -J_1 - J_2 - J_3 - J_4 \\
E_{2H} &= J_0 \quad +J_1 - J_2 + J_3 - J_4 \\
E_{4H} &= J_0 \quad +\frac{1}{2}(-J_1 + J_2 + J_3 - J_4) \\
&\qquad\quad +\frac{1}{2}(J_1 + J_2 - J_3 - J_4) \\
&= J_0 \quad +J_2 + J_4 \\
E_{6H} &= J_0 \quad +\frac{1}{3}(-J_1 - J_2 + J_3 + J_4) \\
&\qquad\quad +\frac{1}{3}(-J_1 + J_2 + J_3 + J_4) \\
&\qquad\quad +\frac{1}{3}(J_1 + J_2 + J_3 - J_4)
\end{aligned}$$

3C:	$\ldots + \; + \; + \; + \; + \; + \; + \; + \ldots$
2H:	$\ldots + \; - \; + \; - \; + \; - \; + \; - \ldots$
4H:	$\ldots + \; + \; - \; - \; + \; + \; - \; - \ldots$
6H:	$\ldots + \; + \; + \; - \; - \; - \; + \; + \ldots$
15R:	$\ldots + \; + \; - \; - \; - \; + \; + \; - \ldots$
8H:	$\ldots + \; + \; + \; + \; - \; - \; - \; - \ldots$

Figure D.1: Polytype structures

$$\begin{aligned}
&= J_0 &+\frac{1}{3}(-J_1 + J_2 + J_4) + J_3 \\
E_{8H} &= J_0 &+\frac{1}{2}(-J_1 + J_3) + J_4 \\
E_{15R} &= J_0 &+\frac{1}{5}(-J_1 + 2J_2 + 3J_3 - J_4).
\end{aligned} \tag{D.2}$$

Assuming J_4 to be zero, these expressions can be inverted to find the J_n's in terms of the energies of the given polytypes, excluding 15R. This is done at the end of chapter IV.

Additionally, the above expressions show that

$$E_{15R} = \frac{2}{5}E_{4H} + \frac{3}{5}E_{6H} \tag{D.3}$$

even when J_4 is included. This result can be generalised by noting that if $J_n = 0$ for $n > 4$, then $I_n = 0$ for $n > 3$ (see section II.5.2). For a polytype made from <2> and <3> units, this means that only nearest neighbour boundary interactions are non-zero. Although both I_2 and I_3 will be present, corresponding to units of <2> and <3> respectively, their proportions are controlled by the total density of boundaries.

$$\rho = \frac{1}{2}\chi + \frac{1}{3}(1 - \chi) \tag{D.4}$$

where ρ is the density of boundaries and χ the proportion of <2> units in the polytype. This equation can be inverted to give

$$\chi = 6\rho - 2. \tag{D.5}$$

The total energy of a bulk polytype is simply

$$\begin{aligned}
E &= J_0 + \rho I_0 + \chi I_2 + (1-\chi) I_3 \\
&= (J_0 - 2I_2 + 3I_3) + \rho(I_0 + 6I_2 - 6I_3) \\
&= J_0' + \rho I_0'
\end{aligned} \tag{D.6}$$

so it can be modelled by a simple boundary energy term even though there are boundary-boundary interactions occurring. This is the approximation used for the electronic energy of the intermediate polytypes in chapter III.

Bibliography

[1] Berzelius, J. J. (1824) *Ann. Phys., Leipzig* **1** 169

[2] von Münch (1982) vol. 17a of *Landolt–Börnstein, New Series* (Berlin: Springer Verlag)

[3] Drowart, J., De Maria, G. and Inghram, M. G. (1958) *J. Chem. Phys.* **29** 1015

[4] Moissan, H. (1905) *Compt. Rend.* **140** 405

[5] Bobrievich, A. P., Kalyuzhnyi, V. A. and Smirnov, G. I. (1957) *Proc. Acad. Sci. USSR, Geol. Sci.* **115** 757

[6] Frazier, B. W. (October 1893) *J. Franklin Inst.* p. 287

[7] Verma, A. R. and Krishna, P. (1966) *Polymorphism and Polytypism in Crystals* chap. 5 (New York: J. Wiley)

[8] Trigunayat, G. C. and Chadha, G. K. (1971) *Phys. Stat. Sol. (a)* **4** 9

[9] Verma, A. R. and Krishna, P. (1966) *Polymorphism and Polytypism in Crystals* (New York: J. Wiley)

[10] Krishna, P., ed. (1983) *Crystal Growth and Characterization of Polytype Structures* vol. 7 of *Prog. Crystal Growth and Characterization* (Oxford: Pergamon Press)

[11] Ramsdell, L. S. (1947) *Am. Mineralogist* **32** 64

[12] Zhdanov, G. S. (1945) *C. R. Acad. Sci. URSS* **48** 43

[13] Neudeck, P. G. (1995) 'Recent progress in silicon carbide semiconductor electronics technology' http://www.lerc.nasa.gov/WWW/SiC/SiCReview.html

[14] Rupp, R., Dohnke, K., Völkl, J. and Stephani, D. (1993) *Inst. Phys. Conf. Ser.* **137** 503

[15] Burton, W. K., Cabrera, N. and Frank, F. C. (1949) *Nature* **163** 398

[16] Frank, F. (1951) *Phil. Mag.* **42** 1014

[17] Steinberger, I. T. (1983) *Prog. in Crystal Growth and Charact.* **7** 7

[18] Mardix, S., Brafman, O. and Steinberger, I. T. (1967) *Acta Cryst.* **22** 805

[19] Pandey, D. and Krishna, P. (1975) *J. Crystal Growth* **31** 66

[20] Jagodzinski, H. (1954) *Neues Jahrb. Mineral Monatsh* **3** 49

[21] Salje, E., Palosz, B. and Wruck, B. (1987) *J. Phys. C* **20** 4077

[22] Winkler, B., Dove, M. T., Salje, E. K. H., Leslie, M. and Palosz, B. (1991) *J. Phys.: Condens. Matt.* **3** 539

[23] Heine, V., Cheng, C. and Needs, R. J. (1991) *J. Am. Cer. Soc.* **74** 2630

[24] de Fontaine, D. and Kulik, J. (1985) *Acta Metall.* **33** 145

[25] Lely, J. A. (1955) *Ber. Deut. Keram. Ges.* **32** 229

[26] Kimoto, T. and Matsunami, H. (1994) *J. Appl. Phys.* **75** 850

[27] Knippenberg, W. F. (1963) *Philips Res. Rep.* **18** 161

[28] Itoh, A., Akita, H., Kimoto, T. and Matsunami, H. (1993) *Inst. Phys. Conf. Ser.* **137** 59

[29] Matsunami, H. (1993) *Inst. Phys. Conf. Ser.* **137** 45

[30] Kordina, O., Hallin, C., Glass, R. C., Henry, A. and Janzén, E. (1993) *Inst. Phys. Conf. Ser.* **137** 41

[31] Yang, J., Nishino, S., Powell, J. A. and Pirouz, P. (1993) *Inst. Phys. Conf. Ser.* **137** 25

[32] Nishino, K., Kimoto, T. and Matsunami, H. (1993) *Inst. Phys. Conf. Ser.* **137** 33

[33] Kanaya, M., Takahashi, J., Fujiwara, Y. and Moritani, A. (1991) *Appl. Phys. Lett.* **58** 56

[34] Buchan, N. I., Henshall, D. N., Yoo, W. S., Mailloux, P. A. and Tischler, M. A. (1993) *Inst. Phys. Conf. Ser.* **137** 113

[35] Stein, R. A. and Lanig, P. (1993) *J. Crystal Growth* **131** 71

[36] Yoo, W. S. (1994) private communication

[37] Lilov, S. K., Tairov, Y. M., Tsvetkov, V. F. and Chernov, M. A. (1976) *Phys. Stat. Sol.* **37** 143

[38] Jepps, N. W. and Page, T. F. (1983) *Crystal Growth and Characterization of Polytype Structures* vol. 7 of *Prog. Crystal Growth and Characterization* chap. 6 (Oxford: Pergamon Press)

[39] Krishna, P., Marshall, R. C. and Ryan, C. E. (1971) *J. Crystal Growth* **8** 129

[40] Tagai, T., Sueno, S. and Sadanaya, R. (1971) *Miner. J.* **6** 240

[41] Krishna, P. and Marshall, R. C. (1971) *J. Crystal Growth* **9** 319

[42] Pandet, D., Lele, S. and Krishna, P. (1980) *Proc. Royal Soc., London* **A369** 435

[43] Jepps, N. W. and Page, T. F. (1979) *J. Microsc.* **116** 159

[44] Inomata, Y., Inoue, Z. and Mitorno, M. (1969) *J. Crystal Growth* **5** 405

[45] Jepps, N. W. and Page, T. F. (1981) *J. Am. Cer. Soc.* **64** C177

[46] Cheng, C., Heine, V. and Needs, R. J. (1990) *J. Phys.: Condens. Matt.* **2** 5115

[47] Käckell, P., Wenzien, B. and Bechstedt, F. (1994) *Phys. Rev. B* **50** 17037

[48] Cheng, C., Heine, V. and Jones, I. L. (1990) *J. Phys.: Condens. Matt.* **2** 5097

[49] Cheng, C., Needs, R. J., Heine, V. and Churcher, N. (1987) *Europhys. Lett.* **3** 475

[50] Cheng, C., Needs, R. J. and Heine, V. (1988) *J. Phys. C* **21** 1049

[51] Shaw, J. J. A. and Heine, V. (1990) *J. Phys.: Condens. Matt.* **2** 4351

[52] Bak, P. and Bruinsma, R. (1982) *Phys. Rev. Lett.* **49** 249

[53] Aubry, S. (1983) *J. Phys. C* **16** 2497

[54] Zeppenfeld, P., Becher, U., Kern, K. and Comsa, G. (1992) *Phys. Rev. B: Cond. Matt.* **45** 5179

[55] de Fontaine, D. (1984) *J. Phys. A.* **17** L713

[56] Jepps, N. W. and Page, T. F. (1983) *Prog. in Crystal Growth and Charact.* **7** 259

[57] Chien, F., Nutt, S. R., Yoo, W. S., Kimoto, T. and Matsunami, H. (1994) *J. Mater. Res* **9** 940

[58] Cheng, C., Kunc, K. and Heine, V. (1989) *Phys. Rev. B* **39** 5892

[59] Cheng, C., Kunc, K. and Heine, V. (1989) *Journal de Chimie Physique* **86** 881

[60] Hofmann, M., Zywietz, A., Karch, K. and Bechstedt, F. (1994) *Phys. Rev. B* **50** 13401

[61] Jagodzinski, H. (1995) *Z. Kryst.* **210** 481

[62] Heine, V. (1980) *Solid State Physics* **35** 1

[63] Bruinsma, B. and Bak, P. (1983) *Phys. Rev. B* **27** 5824

[64] Kong, H. S., Edmond, J. A., Palmour, J. W., Glass, J. T. and Davis, R. F. (1989) *Amorphous and Crystalline Silicon Carbide* vol. 34 of *Springer Proc. in Phys.* p. 180 (Berlin: Springer Verlag)

[65] Short, H. E. (1994) 'Devil's staircase in SiC?' Part II Project, University of Cambridge (unpublished)

[66] Karch, K., Pavone, P., Windl, W., Schütt, O. and Strauch, D. (1994) *Phys. Rev. B* **50** 17054

[67] Windl, W., Karch, K., Pavone, P., Schütt, O., Strauch, D., Weber, W. H., Hass, K. C. and Rimai, L. (1994) *Phys. Rev. B* **49** 8764

[68] Churcher, N., Kunc, K. and Heine, V. (1986) *J. Phys. C* **19** 4413

[69] Born, M. and Oppenheimer, R. (1927) *Ann. Physik* **84** 457

[70] Hohenberg, P. and Kohn, W. (1964) *Phys. Rev.* **136** B 864

[71] Kohn, W. and Sham, L. J. (1965) *Phys. Rev.* **140** A 1133

[72] Ceperley, D. M. and Alder, B. J. (1980) *Phys. Rev. Lett.* **45** 566

[73] Perdew, J. P. and Zunger, A. (1981) *Phys. Rev. B* **23** 5048

[74] Perdew, J. P. (1991) in *Electronic Structure of Solids '91*, eds. P. Zeische and H. Eschrig (Berlin: Akademie Verlag)

[75] White, J. A. and Bird, D. A. (1994) *Phys. Rev. B* **50** 4954

[76] Ashcroft, N. W. and Mermin, N. D. (1976) *Solid State Physics* chap. 8, p. 131 (Philadelphia: Saunders College)

[77] Cunningham, S. L. (1974) *Phys. Rev. B* **10** 4988

[78] Chadi, D. J. and Cohen, M. L. (1973) *Phys. Rev. B* **8** 5747

[79] Monkhorst, H. J. and Pack, J. D. (1976) *Phys. Rev. B* **13** 5188

[80] Hamann, D. R., Schlüter, M. and Chiang, C. (1979) *Phys. Rev. Lett.* **43** 1494

[81] Kleinman, L. and Bylander, D. M. (1982) *Phys. Rev. Lett.* **48** 1425

[82] Heine, V. (1970) *Solid State Physics* **24** 1

[83] Denteneer, P. J. H. and van Haeringen, W. (1985) *J. Phys. C* **18** 4127

[84] Payne, M. C., Teter, M., Allan, D. C. and Joannopoulos, J. D. (1992) *Rev. Mod. Phys.* **64** 1045

[85] Car, R. and Parrinello, M. (1985) *Phys. Rev. Lett.* **55** 2471

[86] Teter, M. P., Payne, M. C. and Allan, D. C. (1989) *Phys. Rev. B* **40** 12255

[87] Lee, M.-H. (1995) *Improved optimised pseudopotentials and application to disorder in* γAl_2O_3 Ph.D. thesis University of Cambridge

[88] Lee, M.-H., Lin, J. S., Payne, M. C., Heine, V., Milman, V. and Crampin, S. (1995) *Phys. Rev. B* (submitted)

[89] Pack, J. D. and Monkhorst, H. J. (1977) *Phys. Rev. B* **16** 1748

[90] Kaye, G. W. C. and Laby, T. H., eds. (1986) *Tables of Physical and Chemical Constants* (London: Longman)

[91] Yean, D. H. and Riter, J. R. (1971) *J. Phys. Chem. Solids* **32** 653

[92] Schreiber, E. and Soga, N. (1966) *J. Am. Cer. Soc.* **49** 342

[93] Lambrecht, W. R. L., Segal, B., Methfessel, M. and van Schilfgaarde, M. (1991) *Phys. Rev. B* **44** 3685

[94] Francis, G. P. and Payne, M. C. (1990) *J. Phys.: Condens. Matt.* **2** 4395

[95] Pulay, P. (1969) *Mol. Phys.* **17** 197

[96] Takayanagi, K., Tanashiro, Y., Takahashi, S. and Takahashi, M. (1985) *Surf. Sci.* **164** 367

[97] Stich, I., Payne, M. C., King-Smith, R. D., Lin, J.-S. and Clarke, L. J. (1992) *Phys. Rev. Lett.* **68** 1351

[98] Kaplan, R. (1989) *Amorphous and Crystalline Silicon Carbide* vol. 34 of *Springer Proc. in Phys.* p. 100 (Berlin: Springer Verlag)

[99] Horn-von Hoegen, M. and Golla, A. (1996) *Phys. Rev. Lett.* **76** 2953

[100] Makov, G. and Payne, M. C. (1995) *Phys. Rev. B: Cond. Matt.* **51** 4014

[101] Neugebauer, J. and Scheffler, M. (1992) *Phys. Rev. B* **46** 16067

[102] Hellmann, H. (1937) *Einführung in die Quantenchemie* (Leipzig: Deuticke)

[103] Feynman, R. P. (1939) *Phys. Rev.* **56** 340

[104] Lide, D. R., ed. (1995) *Handbook of Chemistry and Physics* (Boca Raton, Florida: CRC Press) 76th edn.

[105] Tairov, Y. M. and Tsvetkov, V. F. (1983) *Prog. in Crystal Growth and Charact.* **7** 111

[106] Vanderbilt, D. (1990) *Phys. Rev. B* **41** 7892

[107] King-Smith, R. D., Payne, M. C. and Lin, J. S. (1991) *Phys. Rev. B* **44** 13063

[108] Käckel, P., Furthmüller, J. and Bechstedt, F. (1996) *Surface Science* **352** 55

[109] Headrick, R. L., Weir, B. E., Bevk, J., Freer, B. S., Eaglesham, D. J. and Feldman, L. C. (1990) *Phys. Rev. Lett.* **65** 1128

[110] Ashcroft, N. W. and Mermin, N. D. (1976) *Solid State Physics* chap. 28, p. 575 (Philadelphia: Saunders College)